NON-PERTURBATIVE QUANTUM GRAVITY:
A CONFORMAL PERSPECTIVE

NON-PERTURBATIVE QUANTUM GRAVITY:
A CONFORMAL PERSPECTIVE

Niet-perturbatieve kwantumzwaartekracht:
een hoekgetrouw perspectief

(met een samenvatting in het Nederlands)

Proefschrift

ter verkrijging van de graad van doctor aan de Universiteit Utrecht op gezag van de rector magnificus, prof. dr. G. J. van der Zwaan, ingevolge het besluit van het college voor promoties in het openbaar te verdedigen op dinsdag 20 maart 2012 des middags te 2.30 uur

door

TIMOTHY GEORGE BUDD

geboren op 8 juli 1984 te Watford, Verenigd Koninkrijk

Promotor: Prof.dr. R. Loll

Contents

Contents

CHAPTER 1

Introduction

The discovery of *general relativity* in the early twentieth century did not only provide an extension of Newton's theory of gravity to a wider range of masses and velocities, it completely changed our concept of space and time. Before, space and time were believed to merely provide a stage on which particles and forces, including gravity, perform their act. Einstein's theory of general relativity, however, has taught us that space and time have dynamics of their own. Space-time can curve and the effect of this curvature on particles is to be interpreted as the force of gravity. In other words, Newton's theory of gravity disappeared from stage and reappeared, in the form of general relativity, as a property of the stage itself. Ever since, the force of gravity has kept its special position among the known fundamental forces.

Another major revolution in physics, which came about around the same time, was the discovery of *quantum mechanics*. It forced us to reconsider the nature of particles and forces on microscopic scales, where gravity seemingly plays no role. Point particles were replaced by wave functions that describe the probabilities of outcomes of measurements. In its initial form a global time was necessary to describe the evolution of these wave functions. However, the application of quantum mechanics to fields rather than individual particles led to a probabilistic description compatible with Einstein's special theory of relativity. At present we have such *quantum field theories*, collectively known as the *standard model*, describing all known particles and three of the four fundamental forces.

Individually, general relativity and quantum mechanics have withstood every single experimental test to which they have been subjected since their discovery. On large scales we can treat gravitational sources completely classically and general relativity tells us precisely how space-time curves. On microscopic scales we are allowed in practice to completely ignore gravitational effects because of its weakness as compared to

the other forces. Therefore, quantum field theory is at present all we need, for instance, to understand the results of particle collisions at the LHC. The fact that presently no experiment requires a quantum description of general relativity for an explanation, does however not mean that such measurements are inconceivable in principle. General relativity and quantum field theory combined do not currently make any prediction about, for instance, the outcome of any experiment involving energies close to the *Planck scale*. To make any predictions at these energy scales we most likely require a quantum theory incorporating gravity.

Initial attempts to quantize general relativity along the same lines which were so successful in the case of the other fundamental forces have failed. In particular, a perturbative expansion around flat Minkowski space leads to a non-renormalizable quantum theory. This failure might have to do with the special position taken by gravity. Conventional quantum field theory relies on having a fixed background metric of space and time, and a well-defined notion of causality that comes along with it. When we introduce gravity into the framework, all these notions become dynamical themselves. It is far from clear how to incorporate a dynamical background in the principles of quantum field theory.

One can take several attitudes towards the problem of quantizing gravity. It could be that the degrees of freedom in general relativity are not fundamental, in the sense that they merely provide an effective description of more fundamental degrees of freedom at a microscopic scale. String theory is one of the most studied approaches following this idea. It relies on a radical departure from the conventional field theory of particles, by introducing extended objects as the fundamental constituents. Another more conservative attitude is to not disqualify the space-time geometry as a fundamental description of gravity, but question the perturbative methods used in the initial quantization attempts. In this thesis we will take the latter point of view.

Let us briefly summarize the origin and the consequences of perturbative non-renormalizability in the context of gravity. As one attempts to calculate quantum corrections to correlation functions in perturbative quantum field theory, often infinities are encountered which must be absorbed in the couplings of the theory. As can be deduced from the negative mass dimension of Newton's constant, at each order in the perturbative expansion of gravity the divergent terms contain increasingly higher powers of the curvature. Unless these divergent terms magically cancel, they must be added as counterterms to the action. Each new term comes with a new coupling constant, whose value must be determined experimentally. At an energy scale well below the Planck scale a finite number of such terms suffices to calculate observables to a desired accuracy, leading to non-trivial predictions. At the Planck scale, however, there is an infinite number of relevant terms, hence an infinite number of undetermined couplings.

A potential way out of this situation is the *asymptotic safety scenario* proposed already in 1976 by Weinberg [104]. Essentially the predictivity of the theory would be restored if the infinite number of couplings would satisfy an infinite number of relations. According to the asymptotic safety scenario this is achieved if the renormalization group flow on theory space, i.e. the infinite-dimensional space of actions parametrized by the values of all possible (dimensionless) couplings, has an ultra-violet (UV) fixed point with only a finite number of attractive directions. The critical surface in theory space, i.e. the subspace containing all actions that flow towards the UV fixed point under renormalization, is then finite-dimensional. The requirement that the gravitational action is contained in this critical surface provides a non-trivial prediction. Evaluating the flow on the infinite-dimensional theory space is a highly non-trivial task. However, using an approximation scheme, known as *truncation*, in which the flow is projected onto some finite-dimensional set of actions, evidence has been gathered that a UV fixed point might exist [80, 95]. This fixed point does not correspond to vanishing couplings and therefore its existence is a truly non-perturbative phenomenon.

Whether a suitable UV fixed point exists in the full theory space is unknown. Instead of "deriving" the UV theory of gravity by including higher and higher energy modes, an alternative route can be taken. As a result of some quantization method one may obtain a proposal for a UV theory of gravity. To check whether this theory reproduces general relativity in the appropriate regime, one should integrate out the high energy modes and thus flow down towards an infra-red effective action. This action can then be compared to the Einstein–Hilbert action of general relativity. Perhaps the best known proposal is loop quantum gravity [97, 101], which is the result of a canonical quantization of general relativity. Related, but employing a path integral quantization, are the spin foam models [52, 92] and the more general framework of group field theories [91].

In this thesis we will study path integral models of gravity sitting, in some sense, in between the asymptotic safety approach and these approaches. The models are collectively referred to as *dynamical triangulations* and have the interpretation of lattice regularizations of the gravitational path integral. They are partly inspired by the lattice treatments of strongly coupled non-gravitational field theories. A good example of a field theory that has significantly benefited from a lattice regularization is quantum chromodynamics (QCD) at low energies. After a Wick-rotation lattice QCD can be probed by computer simulations using Monte Carlo techniques [98]. Much has been learned about the confined phase of QCD in this way [87], including accurate calculations of the masses of light hadrons.

Roughly speaking we can view a lattice field theory action as an effective action at an energy scale determined by the lattice spacing. In this picture the renormalization group flow discussed above takes on a concrete interpretation, namely, it tells us how

we should change the action in order to compensate the effect of a change in the lattice spacing on physical observables. These observables can be taken to be correlation functions or Wilson loops depending on whether gauge symmetry is present. If we are interested in the UV behaviour of the field theory, we decrease the lattice spacing and adjust the couplings accordingly. This is what we are after in the context of gravity.

However, when we try to apply the same methods to general relativity, we run into a number of difficulties. First of all, the gravitational field describes the geometry of space-time, therefore a lattice version should describe the geometry of the lattice itself. In this case it makes no sense to fix a regular lattice with prescribed lattice spacing, as often used in lattice field theory. To maintain geometric degrees of freedom, either the lattice spacing must become dynamical, leading to Regge calculus [105, 106], or the connectivity of the lattice (see [82] for a summary of various approaches). Dynamical triangulations are based on the latter option, in which the fixed lattice spacing has the interpretation as a UV regulator.

Secondly, in the absence of a preferred time variable in general relativity it is far from clear how an explicit Wick rotation can be implemented even in principle. As we will see, attempts in this direction have inspired the introduction of a slightly adapted version of dynamical triangulations, known as causal dynamical triangulations (CDT).

Thirdly, after Wick-rotating the gravitational action presumably takes the form of the Euclidean Einstein–Hilbert action, which is known to be unbounded below in three and four dimensions [39, 84]. This so-called *conformal mode problem* implies that the classical solutions of the bare action do not correspond to the lowest-energy states of the system. The naive (semiclassical) path integral does not seem to exist, since the unboundedness leads to arbitrarily large integrands. Even if the unboundedness is "cured" by a UV cut-off on the degrees of freedom, the naive classical limit $\hbar \to 0$ will presumably have little to do with the classical solutions of the action.

The last difficulty we mention here holds for any approach to quantum gravity going beyond perturbations around a fixed background. Namely, it is much harder to define observables for a diffeomorphism-invariant system than it is for field theories in a fixed space-time. Since such observables should be independent of the chosen coordinates, we cannot simply take correlation functions of local scalars constructed from the metric. Diffeomorphism-invariant observables are necessarily non-local and will, in the absence of additional ingredients like clocks and rods, generically involve integrations over the full space-time manifold. In the canonical formulation of gravity, observables, or more precisely *Dirac observables*, have to commute with the constraints, and their identification involves partially solving the dynamics of general relativity [46].

Nonetheless, the identification of observables seems necessary for several reasons. Real experiments correspond to observables in the sense above, either directly or indi-

rectly. If we want to regard a model of gravity as a scientific theory, it should predict the outcome of real experiments, such that it can be falsified in principle. Two kinds of gravitational experiments are of importance, namely, experiments that have been performed and agree with general relativity and experiments we might perform in the future including ones that are sensitive to quantum effects. A viable model of quantum gravity should, in principle, address both kinds of experiments and agree with general relativity on the first kind.

On a more abstract level, observables allow us to physically distinguish different models of (quantum) gravity or find unexpected connections between them. An example of an observable in quantum gravity that has led to unexpected connections is the scale-dependent spectral dimension, first measured in CDT in 3+1 dimensions [15]. Similar scaling has later been observed in, among others, asymptotic safety [96], Hořava–Lifshitz gravity [68] and four-dimensional Euclidean dynamical triangulation [79] (see also [37]).

As we already hinted at before, having a toolbox of observables is useful, or perhaps even necessary, when searching for a continuum limit in the sense of lattice field theory. The requirement that the outcomes of measurements of physical observables, at least the dimensionless ones, do not change under a change in the lattice spacing leads to non-trivial relations between the couplings of the theory.

The final reason is purely pragmatic, namely, the only sensible way to get numbers out of a Monte Carlo simulations is through observables. This is quite clear in the case of dynamical triangulations, where the computer only keeps track of the connectivity of the lattice sites. The computer knows nothing about coordinates and therefore we simply cannot ask it coordinate-dependent questions. Although one can quite easily construct a complete set of "lattice observables", the challenge is to select observables from this huge set that have a good continuum interpretation.

These considerations lead us to the main research questions that we will attempt to address in this thesis. What interesting observables can we define in the setting of dynamical triangulations having an interpretation in terms of continuum geometry? Given such observables, how can we use them to study the physical properties of the model? In particular, in the case of CDT in 2+1 dimensions, can we deduce from measurements the existence and nature of a classical and/or continuum limit?

1.1   (Causal) Dynamical Triangulations

Most path integral approaches to quantum gravity in d dimensions have as starting point the purely formal path integral

$$Z = \int \frac{\mathcal{D}g}{\text{Diff}} e^{\frac{i}{\hbar} S_{\text{EH}}[g]} \tag{1.1}$$

over Lorentzian space-time metrics $g_{\mu\nu}(x)$ on a fixed d-dimensional manifold. The action appearing in the exponent is the Einstein–Hilbert action

$$S_{\text{EH}}[g] = \kappa \int \mathrm{d}^d x \sqrt{-g}(R - 2\Lambda) \tag{1.2}$$

of classical general relativity, where $\kappa = 1/(16\pi G)$ is related to the Newton's constant G and Λ is a cosmological constant.

   To turn this path integral into a less ill-defined quantity, we would like to invoke a Wick-rotation to imaginary time. We want to go beyond perturbation theory around Minkowski space and therefore cannot rely on a preferred time variable (up to Lorentz transformations). It is unclear how one could give, even in principle, a "unique" coordinate-invariant prescription for a Wick rotation from Lorentzian to Euclidean geometries. One may take the attitude that such a prescription is not strictly necessary, as long as physical predictions can be obtained from the theory and compared to nature. We follow the Euclidean quantum gravity approach introduced by Hawking [65] and simply take the Euclidean version of (1.1) as our starting point,[1]

$$Z = \int \frac{\mathcal{D}g}{\text{Diff}} e^{-\frac{1}{\hbar} S_{\text{EH}}[g]}, \tag{1.3}$$

where now the integral is over Riemannian metrics g_{ab} on a d-dimensional compact manifold M and the Euclidean Einstein–Hilbert action is given by

$$S_{\text{EH}}[g] = -\kappa \int \mathrm{d}^d x \sqrt{g}(R - 2\Lambda). \tag{1.4}$$

This formal path integral has the interpretation of a partition function of a thermal system, since each space-time metric occurs with a Boltzmann weight determined by the "energy" $S_{\text{EH}}[g]$.

   Most observables evaluated with respect to the partition function (1.3) will have no direct interpretation in terms of the original Lorentzian path integral. In conventional

---

[1] In the remainder of this thesis we set $\hbar = 1$, effectively absorbing it in κ.
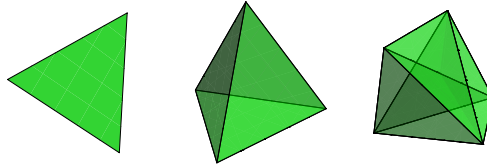
Figure 1.1: *Triangles, tetrahedra, and four-simplices with fixed edge length a form the elementary building blocks of dynamical triangulations in $d = 2, 3, 4$ dimensions, respectively.*

lattice field theory one has to perform an inverse Wick-rotation on the Euclidean correlation functions to obtain the physical correlation functions in Minkowski space. A similar procedure for the observables in some well-defined version of the gravitational path integral likely involves a choice of time. Whether and how this might be achieved, is a non-trivial question, which we will not touch upon in this thesis. Using observables we will try to understand the Euclidean path integral as a statistical theory of geometries, therefore not relying on any kind of Wick-rotation. For instance, in chapter 3 we will study the relation between a lattice regularization and a continuum treatment of the Euclidean path integral in two dimensions. In chapters 4, 5, and 6, we will try to understand the large-distance limit of a three-dimensional lattice regularization, again in a purely Euclidean setting but with a notion of time.

Dynamical triangulations (DT) in d dimensions is a particular regularization of the formal partition function (1.3). The integral over the space of all geometries, i.e. the space of metrics modulo diffeomorphisms, is replaced by a sum over a countable set $\mathcal{T}$. The ensemble $\mathcal{T}$ is formed by all piecewise flat manifolds with the topology of M that can be constructed from a finite number of flat equilateral d-simplices with fixed edge length a, as shown in figure 1.1 for $d = 2, 3, 4$. The fixed edge length a is the analogue of the lattice spacing in lattice field theory. The idea is that taking $a \to 0$ the ensemble $\mathcal{T}$ becomes more and more dense in the full space of geometries.

In general, the curvature of a piecewise flat manifold has support on the $(d - 2)$-dimensional simplices, i.e. on the vertices for $d = 2$, the edges for $d = 3$, and the triangles for $d = 4$. Despite the singular character of the curvature, the Euclidean Einstein–Hilbert action (1.4) can be generalized unambiguously[2] to these geometries, leading

---

[2]The Regge action is unambiguous in the sense that it can be derived from the Einstein–Hilbert action by considering a family of smooth metrics approximating a piecewise flat geometry [53]. If one is merely looking for discretizations of the Einstein–Hilbert action that become exact in the low curvature regime, the usual discretization ambiguities apply.

to the so-called (Euclidean) Regge action [93]. In the case of dynamical triangulations, where all edge lengths are fixed, the Regge action simplifies to a linear combination of the numbers of simplices of various dimensions.

Dynamical triangulations were first studied in $d = 2$ dimensions mainly in the context of non-critical string theory [6, 40, 77]. This model will be the subject of chapters 2 and 3. In the early nineties its generalizations to $d = 3$ [7, 19] and $d = 4$ [1] gained a lot of attention. As we will briefly discuss in the introduction to chapter 4, detailed simulations revealed that these higher-dimensional models in their current form seem to be lacking a good continuum limit.[3]

It the late nineties a new model of dynamical triangulation was introduced [5, 13, 16], referred to as *causal dynamical triangulation* (CDT). It was constructed in an attempt to resemble better the causal structure present in the Lorentzian path integral (1.1), by introducing a time foliation in the dynamical triangulations. The leaves of the foliation, i.e. the constant-time hypersurfaces, are required to have a fixed topology. We will see precisely what this means when we introduce CDT in 2+1 dimensions in chapter 4.

As a consequence of the causality condition on the triangulations, the CDT ensemble forms a proper subset of the DT ensemble described above. In terms of continuum geometry, the CDT ensemble seems to be best understood as an approximate sampling of the subset of Riemannian geometries that allow for a proper-time foliation. In support of this point of view, the continuum limit of CDT in 1+1 dimensions [16] has been shown to agree with continuum quantization of two-dimensional gravity in proper-time gauge [88].

The presence of a preferred time slicing in CDT has several consequences. First of all, with a preferred time variable there seems to be a closer connection, in the sense of Wick-rotations, to Lorentzian gravity. Secondly, the foliation provides more opportunities to define observables, since we can apply an observable for d-dimensional geometries to a certain constant-time surface in $(d + 1)$-dimensional CDT. We will make use of this property extensively in this thesis. Finally, it naturally opens up the possibility to compare CDT to other models of gravity with a preferred time slicing. These include the various formulations of Hořava–Lifshitz gravity [66, 67] and shape dynamics, which we will discuss in chapter 7.

1.2 Conformal perspective

Two-dimensional Riemannian geometry on compact surfaces is well-understood, especially compared to geometry in higher dimensions. This is likely due to the fact that

---

[3]However, see [79] for some renewed interest in a slightly adapted model of 4d dynamical triangulations.

the conformal equivalence classes of Riemannian geometries are directly related to Riemann surfaces, which are classified according to the well-known *uniformization theorem*. Any geometry on the two-sphere can be obtained by a conformal transformation of a single symmetric two-sphere. Geometries on the torus are obtained by conformal transformations of flat tori, of which there is a two-parameter family. To be precise, any metric g_{ab} on the torus can be decomposed in suitable coordinates as

$$g_{ab}(x) = e^{2\phi(x)}\hat{g}_{ab}(\tau), \tag{1.5}$$

where $\hat{g}_{ab}(\tau)$ is a family of unit-volume flat metrics parametrized by the moduli τ_1 and τ_2 and $\phi(x)$ is a position-dependent conformal factor. This conformal decomposition is unique up to translations in the coordinates and therefore gives rise to a complete set of diffeomorphism-invariant observables, namely, the moduli τ together with all translation-invariant functionals of the conformal factor.

This abundance of potential observables, especially the conformally invariant moduli, is the main reason why we chose to study two-dimensional DT on the torus and three-dimensional CDT with spatial topology of the torus. It is very valuable to have access to both conformally invariant, or *transverse traceless*, degrees of freedom and conformal factor, or *pure trace*, degrees of freedom in the spatial geometry, because of the distinct roles they play in general relativity.[4] As we will see they appear in the kinetic term of the Einstein–Hilbert action with opposite signs. Moreover, in the canonical formulation of gravity one can identify precisely the transverse traceless degrees of freedom as the physical degrees of freedom [109, 110].

1.3 Outline

In this thesis we discuss three different models of gravity: two-dimensional dynamical triangulation in chapters 2 and 3; causal dynamical triangulation in 2+1 dimensions in chapters 4, 5 and 6; canonical general relativity in 2+1 dimensions in the formulation of shape dynamics in chapter 7.

In chapter 2 we consider so-called *baby universes* in two-dimensional gravity. These baby universes can be interpreted as the result of local excitations in the conformal factor and characterize the fractal nature of random surfaces. To test an old conjecture concerning the distribution of baby universes as function of their neck size, we introduce an observable that measures the length of the shortest topologically non-trivial loop on a triangulation of the torus.

---

[4]To prevent confusion we will refrain from using the term "conformal degrees of freedom", since unfortunately it can be found in the literature to refer to either type.

In chapter 3 we introduce the conformally invariant *moduli* as observables for 2d gravity on the torus. Using Monte Carlo simulations we determine numerically the distribution of these moduli, which we compare to analytical results from Liouville theory.

In chapter 4 we perform an initial investigation of CDT with spatial topology of a torus. Using Monte Carlo simulations we measure expectation values and correlations of the spatial volumes, which can be interpreted as the global conformal mode, at different instances in time. We show how these measurements relate to classical solutions of three-dimensional general relativity.

In chapter 5 we apply the moduli observables to the spatial geometries in CDT. By combining the measurements of the moduli and the spatial volumes, we can establish the relative strength with which they appear in the kinetic term of the effective action. These results suggest a general kinetic term of the form given by a non-covariant Wheeler–DeWitt metric.

In chapter 6 we qualitatively confirm these results by measuring correlations in the extrinsic curvature of a fixed boundary in space-time.

Finally, in chapter 7 we discuss *shape dynamics* in 2+1 dimensions, which is a reformulation of general relativity, where the refoliation symmetry has been traded for spatial conformal symmetry. This shows that a preferred time slicing is not necessarily in contradiction with general relativity.

Baby universes in 2d gravity

This thesis is mainly concerned with lower-dimensional models of gravity, i.e. models with a number of dimensions lower than the four space-time dimensions we observe around us. In this and the next chapter we will focus on Euclidean gravity in two dimensions, which is one of such models that attracted a lot of attention in the 1980s and early 1990s. The main reason for this is its close connection to string theory. The central ingredients of string theory are strings that sweep out a two-dimensional world sheet embedded in some higher-dimensional space time manifold. The way one usually describes the dynamics of these strings is by assigning a geometry to the world-sheet and viewing the coordinates of the embedding as matter fields. In particular one can interpret a bosonic string living in a flat d-dimensional background as two-dimensional gravity on the world sheet coupled to d Gaussian matter fields. From this point of view pure 2d gravity is equivalent to bosonic string theory in a zero-dimensional background.

Although our reasons for studying two-dimensional gravity are not directly related to string theory, we can benefit from the set of tools that have come available to us through this connection. One of these tools that we will briefly discuss in the next chapter is Liouville theory, which allows us to perform analytic quantum gravity calculations in the continuum. In this chapter we will restrict ourselves to a discrete formulation of 2d gravity known as 2d dynamical triangulations (DT).

This purely combinatorial model, which we will introduce shortly, allows for numerical evaluation using Monte Carlo techniques, just like its higher-dimensional versions including the model of causal dynamical triangulations in 2+1 dimensions that we will

---

This chapter is largely based on [2] with some additions from [3].

discuss later. Contrary to its higher-dimensional cousins, DT in two dimensions also allows for some calculations to be done analytically. As such it provides an ideal testing ground for observables we have designed and intend to study in higher dimensions. This will be the subject of chapter 3 where we will investigate the modular parameter as an observable in 2d DT. Later, in chapter 5, we will actually make use of this observable in CDT in 2+1 dimensions.

In this chapter we will have a closer look at the two-dimensional geometries appearing in the DT model. These geometries turn out to be quite different from smooth Riemannian manifolds. A particular manifestation of their non-smooth structure is the appearance of baby universes, i.e. regions within the geometry that are connected to the rest of the universe through a neck of microscopic size. The distribution of such baby universes has been investigated by Jain and Mathur in [70] using simple scaling arguments. The main goal of this chapter is to show that their conjecture concerning the distribution of baby universes with non-minimal necks cannot be correct. Instead, we will put forward a modified conjecture. In section 2.4 we present a non-trivial numerical check of this conjecture by measuring non-contractible loops within DT on a torus. However, let us first introduce the set-up of dynamical triangulations in two dimensions.

2.1 Introduction to 2d dynamical triangulations

Our starting point is the Euclidean Einstein–Hilbert (1.4), given in $d = 2$ dimensions by

$$S[g] = -\kappa \int \mathrm{d}^2 x \sqrt{g}(R - 2\Lambda) \tag{2.1}$$

in terms of the two-dimensional Riemannian metric g_{ab} on a compact surface. Special to two dimensions is that the first term in this action is a topological invariant. According to the Gauss–Bonnet theorem it is determined by the genus g of the surface, i.e. the number g of handles one has to attach to a sphere to obtain the topology of the surface, namely,

$$\int \mathrm{d}^2 x \sqrt{g}\, R = 8\pi(1 - g). \tag{2.2}$$

This means that as long as we keep the topology constant the curvature term does not contribute to the dynamics. We can therefore drop it from the action and are left with only a cosmological term,

$$S[g] = \lambda V[g], \tag{2.3}$$

where $V[g]$ is the two-dimensional volume corresponding to the metric g_{ab} and $\lambda = 2\kappa\Lambda$.

Classically this action is of little interest, since for $\lambda = 0$ the equations of motion are automatically satisfied and for $\lambda \neq 0$ there is no solution. However, quantum-mechanically this action leads to quite an interesting theory. Formally we can write the path integral for two-dimensional Euclidean quantum gravity as

$$Z(\lambda) = \int \mathcal{D}g \, e^{-\lambda V[g]}, \tag{2.4}$$

where $\mathcal{D}g$ represents some measure on the space of metrics. This partition function can be expressed as the Laplace transform of the fixed-volume partition function $Z(V)$,

$$Z(\lambda) = \int_0^\infty \mathrm{d}V \, Z(V) e^{-\lambda V} \quad \text{and} \quad Z(V) = \int \mathcal{D}g \, \delta(V - V[g]). \tag{2.5}$$

We will not attempt to give a rigorous meaning to the measure in the integrals over metrics, but in keeping with the invariance of the theory it should involve an integration over diffeomorphism classes only, i.e. geometries instead of metrics.

Dynamical triangulations is a lattice regularization of the path integral over geometries in which the integral in (2.4) is replaced by a sum over triangulated geometries. Moreover we choose the triangles from which the geometries are assembled to be equilateral with edge length a. More precisely, we are led to the DT partition function

$$Z(\lambda) = \sum_{T \in \mathcal{T}} \frac{1}{C_T} e^{-\lambda V[T]}, \tag{2.6}$$

where $\mathcal{T}$ is a suitable ensemble of triangulations consisting of a finite number of equilateral triangles. The combinatorial factor C_T is equal to the order of the symmetry group of the triangulation T and is usually implicitly taken into account by working with labelled or marked triangulations. The volume $V[T]$ is simply proportional to the number $N[T]$ of triangles:

$$V[T] = \frac{\sqrt{3}}{4} a^2 N[T]. \tag{2.7}$$

Usually we work with the renormalized cosmological constant $\mu = \frac{\sqrt{3}}{4} a^2 \lambda$ in terms of which the partition function becomes

$$Z(\mu) = \sum_{T \in \mathcal{T}} \frac{1}{C_T} e^{-\mu N[T]}. \tag{2.8}$$

In practice we will usually not consider the *grand canonical partition function* (2.8), but rather the *canonical partition function* $Z(N)$ with fixed number N of triangles, i.e.

$$Z(N) = \sum_{T \in \mathcal{T}(N)} \frac{1}{C_T}, \tag{2.9}$$

which is the discrete counterpart of (2.5).

For the ensemble $\mathcal{T}$ several natural options are available, which have to do with the particular restrictions we impose on the way the triangles are to be glued. In general the differences between the various ensembles become unimportant in the large volume limit $N \to \infty$, but at finite N certain ensembles can be more convenient than others. The ensemble that we will use most often and denote by $\mathcal{T}_1$ is the ensemble in which we put no restrictions on the pair-wise gluing of edges, as long as the resulting piece-wise linear manifold has the topology of a surface with genus g. These triangulations can be described dually by a 3-valent graph embedded in a genus-g surface. In this representation $\mathcal{T}_1$ corresponds to the set of all inequivalent embedded 3-valent graphs. In the case of spherical topology these graphs correspond exactly to planar graphs.

A slightly smaller ensemble $\mathcal{T}_3 \subset \mathcal{T}_1$ that we will consider consists of all triangulations in $\mathcal{T}_1$ that have the structure of a simplicial complex. In a simplicial complex the simplices, in this case the triangles and the edges, have to be uniquely determined by the set of vertices they contain. This means that edges are not allowed to begin and end at the same vertex and any pair of vertices is allowed to be connected only by a single edge. In terms of the dual 3-valent graphs this implies that we do not allow for tadpoles and self-energy diagrams.[5]

Ignoring the symmetry factor C_T, which equals 1 for the vast majority of large triangulations, the partition function $Z(N)$ simply counts the number of inequivalent triangulations with N triangles. Explicit expressions can in principle be worked out for $Z(N)$. It can be shown that its leading behaviour as $N \to \infty$ is

$$Z^{(g)}(N) \propto N^{(5g-7)/2} e^{\mu_0 N}, \tag{2.10}$$

where μ_0 is independent of the genus but does depend on the chosen ensemble $\mathcal{T}$ (see e.g. [8]).

The partition functions described up to now are for pure two-dimensional gravity. In this case, as is apparent from (2.9), all geometries appear in the canonical partition function with the same weight. This changes when we couple matter to the gravitational field. In general the partition function for dynamical triangulations coupled to gravity will be of the form

$$Z(N) = \sum_{T \in \mathcal{T}} \frac{1}{C_T} Z_m(T), \tag{2.11}$$

where $Z_m(T)$ is the partition function of the matter fields on a fixed triangulation T.

In addition to the pure gravity case we will study in this thesis gravity coupled to Gaussian fields. As mentioned at the beginning of this chapter we can interpret 2d

---

[5]The notation $\mathcal{T}_l$ refers to the minimal loop length l we allow in the edge graph: in $\mathcal{T}_1$ we allow loops of a single edge, while in $\mathcal{T}_3$ a loop consists of at least three edges.

gravity coupled to d Gaussian fields as a model of non-critical bosonic strings moving in a d-dimensional flat background, as described by the Polyakov action. As a conformal field theory this model has a central charge c equal to the number of dimensions d (and therefore we will in the following refer to c instead of d). For Euclidean quantum gravity coupled to conformal matter with central charge c the partition function can be shown (see e.g. [45]) to scale with volume V as

$$Z^{(g)}(V) = V^{\gamma(g)-3}e^{\lambda V}. \tag{2.12}$$

Here λ is a bare cosmological constant, and $\gamma(g)$ is the *susceptibility exponent* given by

$$\gamma(g) = \gamma_0 + g(2 - \gamma_0), \quad \text{where} \quad \gamma_0 = \gamma(0) = \frac{c - 1 - \sqrt{(c-1)(c-25)}}{12}. \tag{2.13}$$

One can introduce a discretized version of this model by assigning to each triangle i a position X_i^a in $\mathbb{R}^d$. Then we can write the matter partition function as [77]

$$Z_m(T) = \int \prod_{i=1}^{N} \mathrm{d}^c X_i^a \exp\left(- \sum_{i,j=1}^{N} X_i^a \Delta_{ij} X_j^b \delta_{ab} \right), \tag{2.14}$$

where Δ_{ij} it the graph Laplacian on the 3-valent graph dual to T, i.e. its non-vanishing entries are $\Delta_{ii} = 3$ for $i = 1, \ldots, N$ and $\Delta_{ij} = -1$ if the triangles i and j are adjacent.

Since the action is quadratic in X_j^a the partition function evaluates (up to some irrelevant prefactors) to

$$Z_m(T) \propto (\det' \Delta)^{-c/2}, \tag{2.15}$$

where the prime means that we should first project out the constant mode from the Laplacian before evaluating the determinant.

Due to Kirchhoff's theorem the determinant $\det' \Delta$ is equal to the number $\mathcal{N}(T)$ of spanning trees on the 3-valent graph dual to T. A spanning tree of a graph is a connected subgraph which connects any two vertices but has no loops. The partition function (2.11) for dynamical triangulations coupled to c Gaussian fields becomes

$$Z_m(N) = \sum_{T \in \mathcal{T}(N)} \frac{1}{C_T} \mathcal{N}(T)^{-c/2}. \tag{2.16}$$

Considering the dimension d as a formal parameter we see that $c = -2$ is special because we get just the factor $\mathcal{N}(T)$ in the summand. Hence we can write for $c = -2$

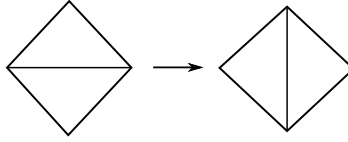$$Z_{c=-2}(N) = \sum_{T \in \mathcal{T}^*(N)} \frac{1}{C_T}, \tag{2.17}$$

Figure 2.1: *The local update move used in Monte Carlo simulations of dynamical triangulations of pure gravity.*

where $\mathcal{T}^*$ is the ensemble of triangulations in $\mathcal{T}$ *decorated with a spanning tree*. Thus we count two such triangulations as different even if they are identical as triangulations but are decorated with different spanning trees.

As we will see in the next section dynamical triangulations with $c = -2$ are especially simple to treat numerically. Therefore in this chapter and the next we choose to restrict our attention to the case of pure gravity $c = 0$ and the case $c = -2$.

2.2 Monte Carlo simulations of dynamical triangulations

Suppose we have an observable $\mathcal{O}$ which assigns a real number $\mathcal{O}(T)$ to a triangulation T. As usual we define its expectation value as

$$\langle \mathcal{O} \rangle_{\mathcal{T}(N)} = \frac{1}{Z(N)} \sum_{T \in \mathcal{T}(N)} \frac{1}{C_T} \mathcal{O}(T). \tag{2.18}$$

We can use Monte Carlo techniques to evaluate such expectation values numerically.

In the case of pure gravity this is easily accomplished by a Markov process in which we start with a triangulation with the desired number N of triangles and the desired topology. A sequence of triangulations $\{T_t\}_{t=1,2,\ldots}$, which constitutes a Markov chain, is then generated by iterating the procedure of selecting a random edge and performing a *flip move* on the two triangles sharing the edge (figure 2.1). These flip moves are ergodic in the sense that any triangulation can be obtained from any other by a finite number of such moves. The triangulation T_t we obtain after a large number t of moves will be independent of the starting configuration. We can view it as a random element in the ensemble $\mathcal{T}$ with uniform probability. In figure 2.4 we show a typical random triangulation for large N.

This procedure can be generalized to dynamical triangulations coupled to matter fields, e.g. Ising spins, by also performing update moves on the matter fields and ensuring that a detailed balance condition is fulfilled. However, we will not discuss this here.
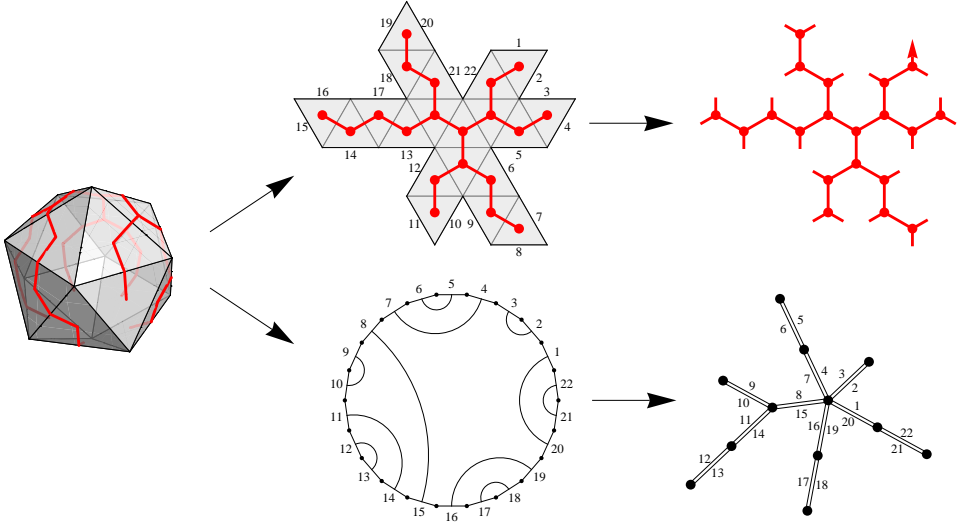
Figure 2.2: *A decorated triangulation can be represented by a binary tree and a unicellular map.*

Instead, let us consider the special case of $c = -2$ presented in the previous section. It was realized in [75] in the case of genus zero that random triangulations with the correct Boltzmann weight can be generated directly. This algorithm circumvents the problem of having to construct a sufficiently long Markov chain, which becomes increasingly time consuming when N is large. It therefore allows us to manage computationally larger system sizes than in the pure gravity case. We will present here a generalization of the method in [75] to arbitrary genus.

Suppose we are given a triangulation of genus g with N triangles together with a spanning tree on its dual graph (see figure 2.2 for an example in which we take the triangulation to be the icosahedron). Let us consider the set of edges of the triangulation which are not intersected by the spanning tree. This set of edges forms a graph consisting of $N/2 + 1$ links and containing $2g$ loops. If we cut open the triangulation along these links, we obtain a triangulation of the disc with a boundary consisting of $N + 2$ links. This triangulated disc in the plane is completely characterized by the 3-valent tree dual to it. This tree has N internal vertices and is obtained from the spanning tree by adding $N + 2$ external lines (see the top part of figure 2.2). To get back to the original triangulation, the boundary edges of the disc have to be glued pairwise. This construction suggests that any decorated triangulation can be obtained by combining a tree and a pairwise gluing.

To make this more precise, let us mark one of the external lines of the 3-valent tree such that we obtain a rooted tree (denoted by an arrow in figure 2.2). This way the tree becomes precisely of the form of a *binary tree*[6] with N nodes. The external links are by construction in 1-to-1 correspondence with the boundary links of the disc. The pairwise gluing of the edges of the disc to a genus-g surface corresponds to a pairwise identification of the external lines in the binary tree such that the resulting trivalent graph can be placed on a genus-g surface without any lines crossing (this is the meaning of the trivalent graph being of genus g). Such a pairwise gluing of a polygon is known as a *unicellular map* [38] (or *one-face map*) of genus g with $N + 2$ *half-edges*. Any combination of a binary tree and a genus-g unicellular map will lead to a triangulation of genus g together with a marked half-edge, i.e. a triangulation of which one side of an edge not intersected by the spanning tree is marked.

It follows that we can write (2.17) as

$$Z_{c=-2}(N) = \sum_{T \in \mathcal{T}^*} \frac{1}{C_T} = \frac{1}{N+2} \sum_{b \in \mathcal{B}(N)} \sum_{u \in \mathcal{U}_g(N+2)} 1, \tag{2.19}$$

where $\mathcal{B}(N)$ is the set of rooted binary trees with N nodes and $\mathcal{U}_g(N+2)$ is the set of genus-g unicellular maps with $N + 2$ half-edges. Therefore, we can generate a random decorated triangulation with the correct probability by separately generating a random binary tree and a random unicellular map. Efficient algorithms exist for generating binary trees, see e.g. [78], section 7.2.1.6.

The difficulty is the implementation of the random unicellular map. The case $g = 0$ was originally solved because it was understood that a genus-zero unicellular map with $N + 2$ half-edges is given simply by a planar tree with one half-edge marked [29, 77] (see figure 2.2 for an example). These planar trees can also be identified with rooted binary trees (see again [78]) and can therefore be easily generated.

To generate a torus we need a random genus-one unicellular map with $N + 2$ half-edges. Luckily in [38] an explicit connection was found between unicellular maps of genus g and genus $g + 1$. In particular, for a genus-0 unicellular map a procedure is given in which three distinct vertices are identified and the half-edges are relabelled in such a way that one obtains a genus-1 unicellular map. It is shown that any genus-1 unicellular map can be obtained through such a procedure in exactly two different ways (see [38], proposition 1 and corollary 1).

Let us briefly summarize the procedure. We label the half-edges of the $N + 2$-gon anti-clockwise by $1, 2, \ldots, N + 2$ and provide them with the corresponding orientation, such that they have a starting vertex and a final vertex. A unicellular map of genus

---

[6] A binary tree is a directed tree in which each node has at most two child nodes: a "left" child and a "right" child.
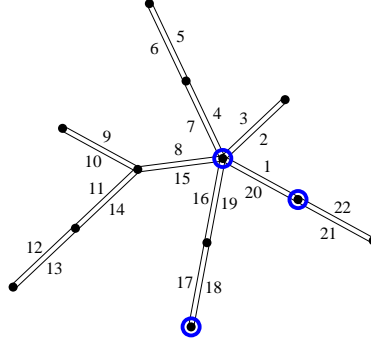
Figure 2.3: *A genus-0 unicellular map with three marked vertices.*

zero is fixed by giving a list α of $N/2 + 1$ pairs of integers which tell us which edges to glue. After the gluing we have a tree with $N/2 + 2$ vertices (see figure 2.2) of which we randomly select three distinct ones. For each of them we select from the set of half-edges having that vertex as its final vertex the smallest index. We denote these indices by a_1, a_2, and a_3 and reorder them such that $1 \leq a_1 < a_2 < a_3 \leq N + 2$. The resulting unicellular map of genus one is now given by gluing according to the list α but replacing $i \to f(i)$, where

$$f(i) = \begin{cases} i + a_3 - a_2 & \text{if } a_1 < i \leq a_2 \\ i - a_2 + a_1 & \text{if } a_2 < i \leq a_3 \\ i & \text{otherwise} \end{cases} . \tag{2.20}$$

We refer to [38] for the actual proof of this statement.

As an example consider the genus-0 unicellular map in figure 2.3 for which three vertices are selected (the encircled ones). The pair-wise gluing is given by

$$\alpha = \{\{1, 20\}, \{2, 3\}, \{4, 7\}, \{5, 6\}, \{8, 15\}, \{9, 10\}, \tag{2.21}$$
$$\{11, 14\}, \{12, 13\}, \{16, 19\}, \{17, 18\}, \{21, 22\}\}.$$

The distinguished half-edges are $a_1 = 1$, $a_2 = 17$ and $a_3 = 20$. Therefore the relabelling according to (2.20) reads

$$\{1, 2, 3, 4, 5, 6, 7, 8, 9, 10, 11, 12, 13, 14, 15, 16, 17, 18, 19, 20, 21, 22\} \tag{2.22}$$
$$\to \{1, 5, 6, 7, 8, 9, 10, 11, 12, 13, 14, 15, 16, 17, 18, 19, 20, 2, 3, 4, 21, 22\}.$$
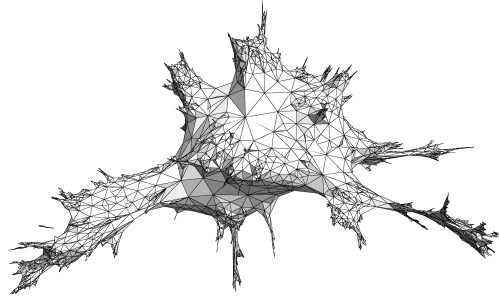
19

Figure 2.4: *An illustration of a typical geometry appearing in the partition function of DT.*

The corresponding genus-1 unicellular map is given by the gluing obtained by applying this relabelling to α, i.e

$$\alpha' = \{\{1,4\},\{5,6\},\{7,10\},\{8,9\},\{11,18\},\{12,13\}, \tag{2.23}$$
$$\{14,17\},\{15,16\},\{19,3\},\{20,2\},\{21,22\}\}.$$

2.3 Distribution of baby universes

Having established algorithms to produce random configurations in the DT partition functions for pure gravity and gravity coupled to $c = -2$ conformal matter, we might ask what a typical geometry looks like. In figure 2.4 an embedding in three dimensions is shown of a random triangulation taken from one of the DT partition functions to illustrate the non-smooth structure. One aspect of the non-classical behaviour of 2d gravity is discussed by Jain and Mathur in [70]. They relate the susceptibility exponent γ_0 defined in (2.13) to the creation of so-called *baby universes*.

First of all they define a *minbu*, or *minimal neck baby universe*, to be a region in a triangulated surface with topology of a disc whose boundary consists of a minimal number of edges. What this minimal number is depends on the precise ensemble considered. In the ensembles $\mathcal{T}_1$ and $\mathcal{T}_3$ we introduced in section 2.1 the minimal neck sizes are 1 and 3 respectively. Jain and Mathur show that the average number of minbus of volume B is given by

$$n_N(B) = k(g)N(1 - B/N)^{\gamma(g)-2}B^{\gamma_0-2}, \tag{2.24}$$

where N is the total volume of the surface, $k(g)$ is a constant depending on the genus g, and we have assumed $B < N/2$.

The leading power-law behaviour of B in (2.24) provides a convenient way to determine γ_0 in numerical simulations and has been extensively used to check the relation (2.13) for dynamical triangulations (see e.g. [18]).

Jain and Mathur also put forward generalized relations based on a conjectured formula involving non-minimal necks (equation (9) in [70]). These necks also divide the surface into two pieces with volumes $N-B$ and B but have an arbitrary length $L < \sqrt{N}$. We show that the conjectured formula cannot be correct and discuss how to modify it appropriately while maintaining many of the results derived there. Our key observation is that the necks of baby universes are by construction special curves on the surface whose scaling as function of the volume N is different from generic curves. In the next section we will perform a non-trivial numerical check of our improved conjecture.

For the moment we will restrict ourselves to the case of pure gravity, i.e. $c = 0$. We will discuss the general situation with $c \leq 1$, and $c = -2$ in particular, in section 2.5.

Consider a (triangulated) surface of area N and spherical topology with n boundary loops of length L_i, $i = 1, \ldots, n$, counting the number of edges in the boundaries. Assume also that none of the boundary loops can be deformed into a loop of shorter length in the same homotopy class, unless the deformation sweeps an area which is a sizeable fraction of N. Jain and Mathur conjectured that the number of such surfaces behaves like

$$\tilde{Z}_n(N, L_i) \sim N^n Z^{(g=0)}(N) \prod_{i=1}^n L_i^{-(1+\gamma_0)}, \quad L_i \lesssim \sqrt{N}. \tag{2.25}$$

The factor N^n corresponds simply to the number of ways n boundary loops can be located on a genus-0 surface. The power for the lengths L_i was determined by making a general ansatz $L_i^{-(1+\alpha)}$. To determine α they calculated the genus-1 partition function from $\tilde{Z}_2(N, L, L)$ by gluing together both boundaries to form a torus and integrating over L up to $\sqrt{N}$,

$$Z^{(g=1)}(N) \sim \int^{\sqrt{N}} \mathrm{d}L \, L \, \tilde{Z}_2(N, L, L), \tag{2.26}$$

where the factor L in the integrand takes into account the freedom in gluing the boundaries. Now $\alpha = \gamma_0$ follows from evaluating this integral and comparing to (2.12).

A number of interesting results were derived in [70] using the ansatz (2.25). In particular the relation $\gamma(g) = \gamma_0 + g(2 - \gamma_0)$ in (2.13) can be directly derived from the ansatz in a way similar to (2.26). Indeed one can construct a genus-g surface from a genus-0 surface with g pairs of boundaries, for which the two boundaries in each pair have the same length L_i, $i = 1, \ldots, g$. It is not hard to see that integration over each L_i as in (2.26) leads to an additional factor of $N^{2-\gamma_0}$.

As Jain and Mathur point out, the number of surfaces of area N with n boundaries of prescribed length which cannot be deformed without increasing their length is strictly

smaller than the number of surfaces with n boundaries without such restrictions, for which explicit formulas are known. The reason for this is that curves that serve as baby universe necks are special curves. However, the consequences of this are even more drastic than envisaged in [70] and are directly related to why ansatz (2.25) cannot be correct. By definition the boundary loop in (2.25) is a geodesic curve and it is well-known that the lengths of such curves scale anomalously in dynamical triangulations [17, 22, 62, 72]. In fact, the dimension of geodesic curves is volume$^{1/4}$ and not volume$^{1/2}$, as one might have expected naïvely, implying that the Hausdorff dimension d_h of surfaces in the DT ensemble is 4. This is reflected in the scaling behaviour of the expectation values

$$\langle R \rangle_N \sim N^{1/d_h}, \quad \langle N(r) \rangle_N \sim r^{d_h}, \text{ for } r \ll A^{1/d_h}, \tag{2.27}$$

where R is the linear extension of a surface of area N, and $N(r)$ the area contained within a geodesic distance r from a given point.

The necks of length L along which Jain and Mathur cut surfaces into disconnected pieces are geodesic curves, which means that their ensemble average is much shorter than the generic $\sqrt{N}$ used as upper limit in integrations like (2.26). (Note that the main contribution to this integral comes precisely from the upper limit.) Instead, according to (2.27), $N^{1/4}$ should be used as upper limit, and, more generally, N^{1/d_h} if the Hausdorff dimension is d_h. An alternative ansatz, which will reproduce most of the results of Jain and Mathur, is to replace (2.25) by

$$\tilde{Z}'_n(N, L_i) \sim N^n Z^{(g=0)}(N) \prod_{i=1}^n L_i^{-(1+\gamma_0 d_h/2)} \quad (c = 0). \tag{2.28}$$

This formula is supposed to be valid for $L_i < N^{1/d_h}$, with the understanding that any integration over N_i is to be performed from the minimal neck length up to N^{1/d_h}. For $L_i > N^{1/d_h}$ the function $\tilde{Z}'_n(N, L_i)$ is assumed to vanish fast.

2.4 Shortest non-contractible loops

As an application of our modified conjecture (2.28), let us consider the case of torus topology, i.e. $g = 1$. The expression (2.26) relating the torus partition function $Z^{(g=1)}(N)$ to the partition function $\tilde{Z}_2(N, L, L)$ of genus-0 surfaces with two geodesic boundaries of length L is modified to

$$Z^{(g=1)}(N) \sim \int^{N^{1/4}} \mathrm{d}L \, L \, \tilde{Z}'_2(N, L, L). \tag{2.29}$$
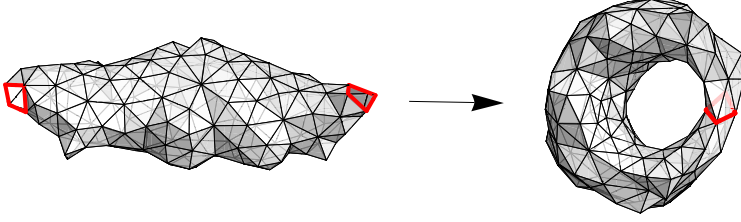
Figure 2.5: *An example of a shortest non-contractible loop of length 4.*

From the point of view of the torus the curve corresponding to the glued boundaries is a non-contractible loop of minimal length (see figure 2.5 for an example). The integrand in (2.29) gives us a prediction for how the length L of the shortest non-contractible loop is distributed in the ensemble of genus-1 dynamical triangulations. We expect the fraction $P_N(L)$ of triangulations with N triangles that have a shortest non-contractible loop of length L to be given by

$$P_N(L) = \frac{L\,\tilde{Z}'_2(N, L, L)}{Z^{(g=1)}(N)} = \frac{L}{N^{1/2}} F\left(\frac{L}{N^{1/4}}\right),\tag{2.30}$$

for some function $F(x)$ that is approximately constant for small x and goes to zero rapidly when $x \gtrsim 1$.

To test this we generate triangulations in the $c = 0$ ensemble with various volumes N using the Monte Carlo technique outlined in section 2.2. Then we determine the length L of the shortest non-contractible loop using the following algorithm.

First we need a method of constructing curves in the triangulation that generate the fundamental group. Inspired by the methods for producing random $c = -2$ triangulations described in section 2.2 we generate an arbitrary spanning tree on the 3-valent graph dual to the triangulation. Then we consider the set of edges of the triangulation that are not intersected by this spanning tree (see figure 2.6). As mentioned in section 2.2 the graph G formed by these edges contains $2g$ cycles, where g is the genus of the triangulation. To extract these cycles we choose an arbitrary vertex v in G and generate a spanning tree for G based at v. This tree will contain all but $2g$ of the edges of G. Adding any of the remaining $2g$ edges to the tree will lead to a cycle and therefore to a unique closed path based at v. The set of $2g$ paths $\{\gamma_i\}_{i=1,\ldots,2h}$ thus constructed generates the fundamental group of the triangulation. Once we have such a set of generators we can establish for any closed curve whether it is contractible or not by computing its oriented intersection number with the generators γ_i. The curve is contractible if and only if all these intersection numbers vanish.
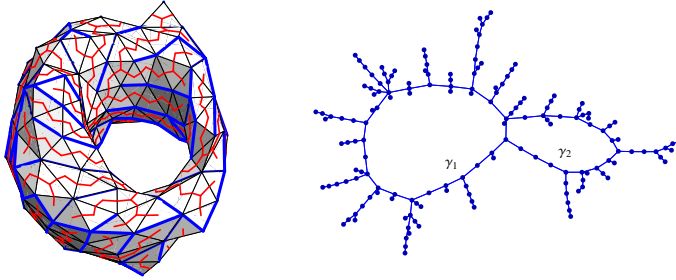
Figure 2.6: *A triangulated torus decorated with a spanning tree (in red). The edges (in blue) not intersected by the spanning tree form a graph with two cycles.*

Given a vertex v we can find a shortest non-contractible loop based at v by performing a so-called breadth-first search in the edge-graph of the triangulation starting at v. Once we encounter a vertex that we have already visited before, we have implicitly established a loop in the edge-graph. The first such loop we meet that is non-contractible will automatically have minimal length.

In principle we can repeat this procedure for each vertex v in the triangulation to find the overall shortest non-contractible loop (or rather a non-contractible loop of minimal length as there is usually more than one). However, in general the set V of vertices for which we have to perform this procedure can be greatly reduced. We know that any non-contractible loop will intersect at least one of the generators γ_i, so it suffices to take V to consist of all vertices contained in the γ_i. In order to obtain such a set V with as few vertices as possible it is worthwhile to first spend some time to shorten the γ_i. This will result in a set V with a number of vertices of the order N^{1/d_h}, with N the number of triangles. Since a single breadth-first search involves a number of steps of the order N, the full algorithm will have an expected run-time of the order N^{1+1/d_h}, which amounts to $N^{1.25}$ for $c = 0$.

In figure 2.7 the measured distributions $P_N(L)$ for random $c = 0$ triangulations from the ensemble $\mathcal{T}_1$ are shown for volumes N ranging from 125 up to $64\,000$ triangles. We rescaled the distribution according to our ansatz (2.30) and observe that the data satisfies the finite-size scaling with good accuracy. Moreover, we see that the universal function $F(x)$ has the form of a smooth cut-off function, which equals a constant for small x and goes to zero rapidly for $x \gtrsim 1$.

These simulations are in clear disagreement with the ansatz of [70] which predicts a
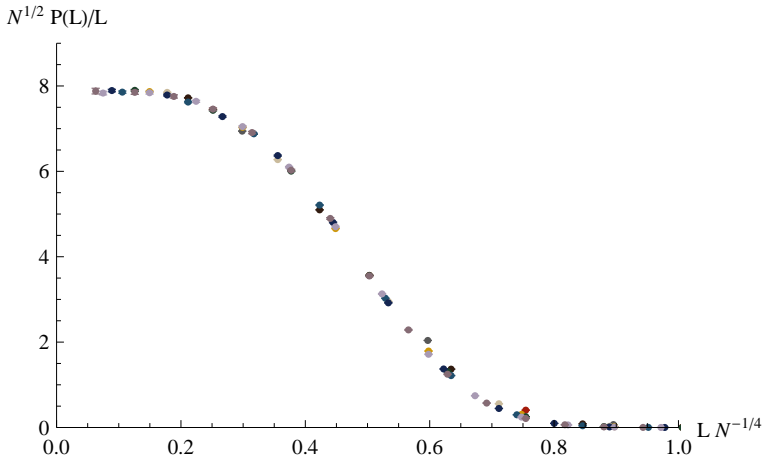
Figure 2.7: *The rescaled distribution of the shortest non-contractible loop length L for volumes $N = 125, 250, 500, \ldots, 64\,000$ and $L = 1, 2, \ldots, 15$ for $c = 0$.*

probability distribution

$$P_N^{\mathrm{(JM)}}(L) \sim \begin{cases} \frac{1}{\sqrt{N}} & \text{for } L \lesssim \sqrt{N} \\ 0 & \text{for } L \gtrsim \sqrt{N} \end{cases}, \tag{2.31}$$

as noted in [71]. Our improved ansatz also resolves a discrepancy found in [71], namely, that (2.31) leads to an average shortest loop length $\langle L \rangle \sim N^{1/2}$ while one would expect

$$\langle L \rangle \sim N^{1/d_h} = N^{1/4} \tag{2.32}$$

because of the anomalous scaling of geodesic distances. It is exactly the latter that follows from our ansatz (2.30), based on (2.28). We have also verified (2.32) numerically as is shown in figure 2.8.

2.5   Baby universes in the presence of conformal matter

The arguments presented above for $c = 0$ need to be refined for the general case of 2d gravity coupled to conformal matter with central charge $c \leq 1$. Integrating out the matter fields we end up with a partition function in which every triangulation appears with a certain weight $Z_m(T)$ as in (2.11). In general this weight depends on the connectivity of the triangulation and is therefore not invariant under cutting and gluing.
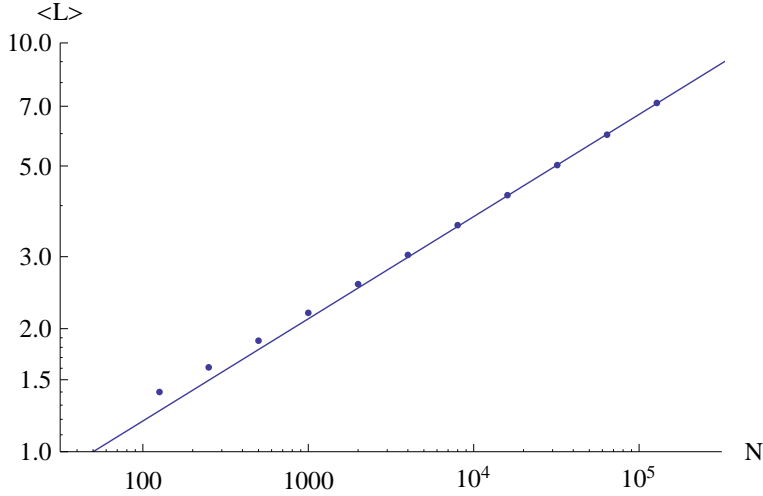
Figure 2.8: *A log-log plot of the expectation value $\langle L \rangle$ for volumes $N = 125, 250, 500, \ldots, 128\,000$ for $c = 0$. The fitted curve corresponds to $\langle L \rangle = 0.376\, N^{1/4}$ (error bars are too small to display).*

We can illustrate this for the case of Ising spins coupled to DT, with spins located at the centres of the triangles and nearest-neighbour interactions. This model has a critical point describing a $c = 1/2$ conformal field theory coupled to 2d gravity [76]. If we consider a triangulated surface with a neck associated to a baby universe, there is clearly an energy associated with the interactions between spins on either side of the neck. There seems to be no non-trivial way of recovering the weight associated with this energy when considering the separate partition functions of the two surfaces we obtain after cutting along the neck. A proper treatment would be to consider partition functions with fixed boundary conditions on the matter fields and to sum over inequivalent boundary conditions with the appropriate weight when gluing.

The error we are making by neglecting the matter boundary conditions will depend on the length of the neck. In the case of minimal-neck baby universes the energy contribution associated with them will become negligible in the continuum limit. This explains why the result (2.24) derived by Jain and Mathur has turned out to be robust also when $c \neq 0$.

The derivations in [70] building on (2.25) for non-minimal necks are much harder to justify. The contributions from the boundary energies might become significant when the boundary lengths become of the order of the linear system size. Notice that it is precisely those long boundary lengths that give important contributions to integrals

like (2.26). Nevertheless, let us for the sake of simplicity assume that we can ignore such boundary energies. In that case we can simply repeat our derivation from the previous section taking into account that the string susceptibility γ and the Hausdorff dimension d_h depend on the central charge c of the matter. It was shown in [103] that the Hausdorff dimension d_h governing the linear extent of random triangulations coupled to conformal matter of central charge c is given by the general formula

$$d_h(c) = 2\frac{\sqrt{25-c}+\sqrt{49-c}}{\sqrt{25-c}+\sqrt{1-c}}. \tag{2.33}$$

The straightforward generalization of (2.28) is

$$\tilde{Z}_n'(N, L_i) \sim N^n Z^{(g=0)}(N) \prod_{i=1}^{n} L_i^{-(1+\gamma_0(c)d_h(c)/2)} \quad \text{(any } c \leq 1\text{)}, \tag{2.34}$$

where $\gamma_0(c)$ is given by (2.13).

The distribution of the length of the shortest non-contractible loop on the torus is altered accordingly. The fraction $P_N(L)$ of triangulations with N triangles that have a shortest non-contractible loop of length L is now expected to be given by

$$P_N(L) = N^{-1/d_h(c)} \left(\frac{L}{N^{1/d_h(c)}}\right)^{|\gamma_0(c)|d_h(c)-1} F\left(\frac{L}{N^{1/d_h(c)}}\right), \tag{2.35}$$

for some function $F(x)$ that is approximately constant for small x and goes to zero rapidly when $x \gtrsim 1$. We conclude that $N^{1/d_h(c)}P_N(L)$ should be a universal function $x^\alpha F(x)$ of the rescaled length $x = N^{-1/d_h(c)}L$ with

$$\alpha = |\gamma_0(c)|d_h(c) - 1. \tag{2.36}$$

Let us test this hypothesis for the case of DT coupled to matter with central charge $c = -2$, for which we developed a numerical method in section 2.2. According to (2.33) the Hausdorff dimension for $c = -2$ is given by $d_h = (3 + \sqrt{17})/2 \approx 3.56$. We can verify this value by measuring the expectation value $\langle L \rangle_N$ of the shortest non-contractible loop length, which should satisfy $\langle L \rangle_N \propto N^{1/d_h(c)}$. The measurements, which are plotted in figure 2.9, show that the theoretical scaling already sets in for quite small triangulations.

As in the case $c = 0$ the distribution $P_N(L)$ satisfies a beautiful finite-size scaling as is shown in figure 2.10. To determine the behaviour of $P_N(L)$ at small L we have plotted the same data on a logarithmic scale in figure 2.11. We observe that the data does not agree well with the expected scaling $P_N(L) \propto L^\alpha$ with $\alpha = (1 + \sqrt{17})/2 \approx 2.56$. A naive power-law fit to the data yields a value of α around 2.2. This means either that the
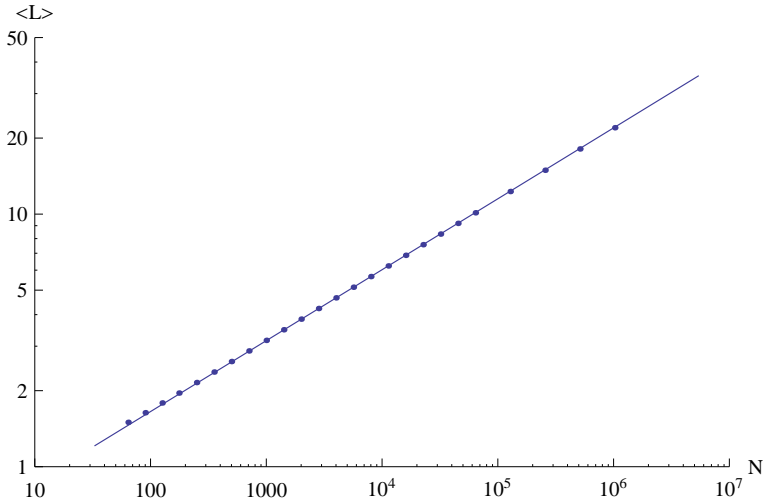
Figure 2.9: *A log-log plot of the expectation value $\langle L \rangle$ for volumes $N = 64, \ldots, 1\,024\,000$ for $c = -2$. The fitted curve corresponds to $\langle L \rangle = 0.454\,N^{1/3.56}$ (error bars are too small to display).*

convergence towards the continuum power-law scaling is very slow or that our ansatz (2.35) is incorrect for $c = -2$.

As in the case of DT coupled to Ising spins we can understand qualitatively where the error might come from. Notice that when we cut open a decorated torus along a neck to get a sphere with two boundaries, we generally cut the spanning tree into several pieces as well. This means that for the cut-open surfaces we should consider the partition function of surfaces with boundaries decorated with multiple trees which together form a *spanning forest*, instead of a single spanning tree. The boundary conditions should then specify for every pair of boundary edges whether they are connected through the spanning forest or not. Needless to say those partition functions are hard to construct in general.

Figure 2.10: *The distribution of the shortest non-contractible loop length L for volumes* $N = 64, \dots, 1\,024\,000$ *and* $L = 1, 2, \dots, 32$ *for* $c = -2$.

Figure 2.11: *Same plot as in figure 2.10 but now on a logarithmic scale.*

Moduli in 2d gravity

In the previous chapter we considered the appearance of baby universes in 2d gravity, which can be viewed as local outgrowths of the geometry. I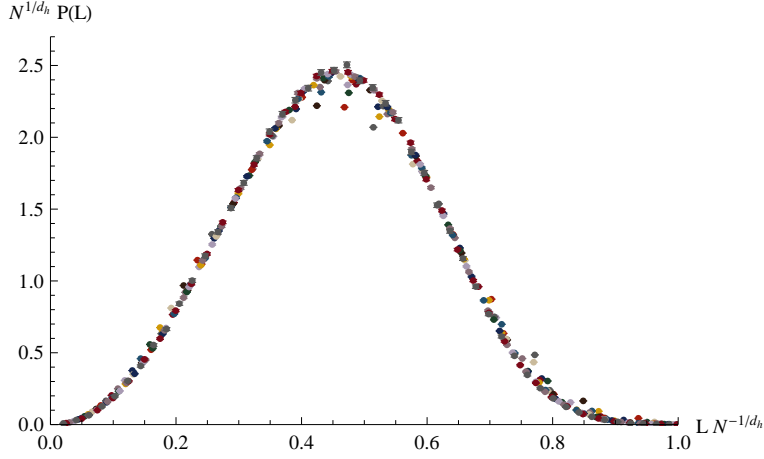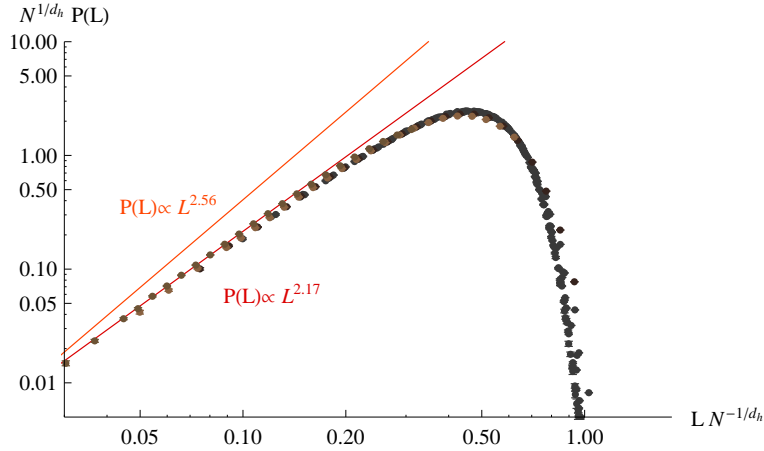n the continuum we can represent any metric on a 2d surface as a conformal transformation of one of a small set of background geometries. We will make this statement more precise when we introduce Liouville field theory in section 3.1, where the Liouville field plays the role of conformal factor. In such a representation baby universes correspond roughly to local excitations in the conformal factor and they therefore reveal the quantum nature of the Liouville field.

In this chapter, however, we will be primarily concerned with degrees of freedom that are invariant under conformal transformations, i.e. the degrees of freedom that remain after integrating out the Liouville field. These degrees of freedom are referred to as the moduli and parametrize the set of background geometries. In non-critical string theory using Liouville theory one can evaluate the integral over the Liouville field and the matter fields in the partition function explicitly in the special case of the torus. What remains is an integral over the two moduli parameters of the torus. The corresponding integrand gives a density in moduli space, which is a measure of how often certain torus shapes occur.

The model of dynamical triangulations (DT) is regarded as a lattice formulation of non-critical string theory. This point of view is backed up by an extensive list of observables that can be calculated analytically in both approaches and for which agreement is found. The moduli parameters as observables, however, are not (yet) on this list. Although some analytical connections have been found between dynamical triangulations

---

This chapter is largely based on [3].

and moduli spaces using matrix model techniques [4], at present we do not know how to derive densities in moduli space explicitly. Instead in this chapter we will resort to numerical methods to find evidence for agreement with the moduli density from non-critical string theory.

To do this we will present in section 3.2 a robust method of assigning moduli parameters to triangulations of the torus. The ensemble of dynamical triangulations with a fixed number N of triangles will lead to a (large but finite) number of points in moduli space. When N goes to infinity we expect this set of points to converge to a smooth density distribution. It is this distribution that we want to compare to the continuum result presented in section 3.1.

The possibility of performing such a comparison was pioneered by Kawai and collaborators in [73, 74] for $c = 0$, $c = 1$ and $c = 2$. They found good qualitative agreement with the results from non-critical string theory. We will improve these results by making them more quantitative in the case $c = 0$ and we will also investigate the case $c = -2$. Finally, in appendix B we will show how one can generalize these techniques to higher genus. Unfortunately at present a theoretical calculation of the moduli density in non-critical string theory for genus larger than one is lacking, so at this stage no comparison is possible.

3.1 Introduction to Liouville gravity

The standard method of evaluating the non-critical string partition function is by gauge fixing the two-dimensional world sheet metric to the so-called *conformal gauge*. In particular, for a surface of genus g one can choose coordinates such that the metric takes the form[7]

$$g_{ab}(x) = e^{2\beta\phi(x)}\hat{g}_{ab}(\tau^i), \tag{3.1}$$

where $\hat{g}_{ab}(\tau^i)$ is taken from a $(2g-2)$-dimensional space of background metrics parametrized by the moduli τ^i, $i = 1, \ldots, 2g-2$. Special to two dimensions is not only that the moduli space $\mathcal{M}$ is finite-dimensional, but also that due to the uniformization theorem we can choose simple representatives for these background geometries, namely, constant-curvature metrics of unit volume. In particular, in the case of the torus we will take the background geometries to be flat.

Formally, the fixed-genus partition function for conformally invariant matter cou-

---

[7] For convenience we have added a normalization constant β in the exponent, which will later be fixed to bring the action for the Liouville field ϕ to canonical form.

pled to 2d gravity reads

$$Z(\lambda) = \int \mathcal{D}g\, \mathcal{D}X \exp\left(-\lambda V[g] - S_m[X, g]\right), \tag{3.2}$$

where $S_m[X, g]$ is some conformally invariant action for the matter fields X. For this partition function to make sense the diffeomorphism symmetry has to be gauge-fixed. In the conformal gauge (3.1) the partition function reduces to an integral over the moduli τ and the Liouville field ϕ,

$$Z(\lambda) = \int \mathrm{d}\tau\, \mathcal{D}_g\phi\, \mathcal{D}_g X\, J_g \exp\left(-\lambda V[e^{2\phi}\hat{g}] - S_m[X, \hat{g}]\right). \tag{3.3}$$

Here J_g is the Faddeev–Popov determinant associated with the conformal gauge fixing.

Even though the matter action is conformally invariant, the matter part of the partition function does depend on ϕ through the measure $\mathcal{D}_g X$ and the Faddeev-Popov determinant J_g. It turns out that one can rewrite them in terms of the background metric $\hat{g}$ as

$$\mathcal{D}_g X\, J_g = \mathcal{D}_{\hat{g}} X\, J_{\hat{g}} \exp\left(\frac{c - 26}{12} S_L[\phi, \hat{g}]\right), \tag{3.4}$$

where $S_L[\phi, \hat{g}]$ is the Liouville action

$$S_L[\phi, \hat{g}] = \frac{1}{4\pi} \int \mathrm{d}^2 x \sqrt{\hat{g}} \left(\hat{g}^{ab}\partial_a\phi\partial_b\phi + \hat{R}\phi + \bar{\mu}e^{2\beta\phi}\right). \tag{3.5}$$

In *critical string theory* we would then require $c = 26$, leading to the usual critical dimension 26, in which the Liouville field completely decouples from the dynamics of the matter fields X. In the case of *non-critical string theory* the central charge is not restricted to $c = 26$ and a non-trivial integration over the Liouville field is required. The idea is that the integration over ϕ should restore the conformal invariance. Remember that the background geometries $\hat{g}(\tau)$ are merely representatives of the conformal equivalence classes of metrics and the partition function is supposed not to depend on the choice of these representatives. In particular, this means that the partition function for the Liouville field and matter fields combined should be invariant under conformal transformations of the background $\hat{g}$.

The measure $\mathcal{D}_g\phi$ cannot be straightforwardly rewritten in terms of the ϕ-independent measure $\mathcal{D}_{\hat{g}}\phi$. However, if one assumes that its contribution is again of the form of the Liouville action (3.5) then the requirement of conformal invariance completely determines the values of the couplings. This way one ends up with a partition function

$$Z = \int \mathrm{d}\tau\, \mathcal{D}_{\hat{g}}\phi\, \mathcal{D}_{\hat{g}} X\, J_{\hat{g}} \exp(-S_L[\phi, \hat{g}] - S_m[X, \hat{g}]), \tag{3.6}$$
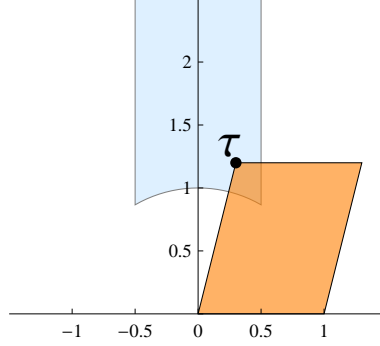
Figure 3.1: *Any flat torus can be obtained by identifying opposite sides of a suitable parallelogram. This identification is unique if we restrict τ to the fundamental domain $\mathcal{M}$ (the shaded region).*

where the full Liouville action is now given by

$$S_L[\phi, \hat{g}] = \frac{1}{4\pi} \int \mathrm{d}^2 x \sqrt{\hat{g}} \left(\hat{g}^{ab} \partial_a \phi \partial_b \phi + Q\hat{R}\phi + \mu e^{2\beta\phi} \right) \tag{3.7}$$

and Q and β are fixed in terms of central charge c,

$$Q = \sqrt{\frac{25 - c}{6}} = \frac{1}{\beta} + \beta, \quad \beta = \frac{\sqrt{25 - c} - \sqrt{1 - c}}{\sqrt{24}}. \tag{3.8}$$

In general, the partition function (3.6) is hard to evaluate, but it simplifies considerably for genus-1 topology [27, 63]. In that case we can choose the background metrics $\hat{g}(\tau)$ to be flat, i.e. $\hat{R} = 0$. Starting from the Euclidean plane we can obtain any flat torus by identifying the opposite sides of a parallelogram. The moduli τ_1 and τ_2 are associated with the position $\tau = \tau_1 + i\tau_2$ of the upper-left corner of the parallelogram when we position it in the upper-half complex plane as shown in figure 3.1. This representation of a flat torus is not unique since there are diffeomorphisms of the torus that do not leave τ invariant. These so-called *large diffeomorphisms* form the *modular group* of the torus and act on τ according to

$$\tau \to \frac{a\tau + b}{c\tau + d}, \quad \begin{pmatrix} a & b \\ c & d \end{pmatrix} \in SL(2, \mathbb{Z})/\mathbb{Z}_2. \tag{3.9}$$

To remove this redundancy we have to restrict τ to a fundamental domain $\mathcal{M}$ of the modular group in (3.9). The standard choice for $\mathcal{M}$ is the "key-hole" region in the upper-half plane,

$$\mathcal{M} = \{-\frac{1}{2} \leq \tau_1 \leq 0 \text{ and } |\tau| \geq 1\} \cup \{0 < \tau_1 < \frac{1}{2} \text{ and } |\tau| > 1\}, \tag{3.10}$$

as illustrated in figure 3.1. If we choose (periodic) coordinates $0 \leq x^1, x^2 < 1$ on the torus, we can write down explicitly a position-independent metric $\hat{g}_{ab}(\tau)$ of unit volume,

$$\hat{g}_{ab}(\tau) = \frac{1}{\tau_2} \begin{pmatrix} 1 & \tau_1 \\ \tau_2 & \tau_1^2 + \tau_2^2 \end{pmatrix}. \tag{3.11}$$

Using this background metric and restricting to fixed volume, as we did in section 2.1, the partition function (3.6) simplifies to [63]

$$Z(V) = \int_{\mathcal{M}} \mathrm{d}\tau \int \mathcal{D}_{\hat{g}} \phi \, \mathcal{D}_{\hat{g}} X \, J_{\hat{g}} \exp\left(-\frac{1}{4\pi} \int \mathrm{d}^2 x \sqrt{\hat{g}} \hat{g}^{ab} \partial_a \phi \partial_b \phi - S_m[X, \hat{g}]\right) \tag{3.12}$$

$$\times \delta\left(V - \int \mathrm{d}^2 x \sqrt{\hat{g}} e^{2\beta\phi}\right). \tag{3.13}$$

The delta function is taken care of by integrating over the constant mode of ϕ. If we take the matter action to be the Polyakov action in c dimensions,

$$S_m[X, \hat{g}] \propto \int \mathrm{d}^2 x \sqrt{\hat{g}} \hat{g}^{ab} \partial_a X^i \partial_b X^j \delta_{ij} \quad \text{with } 1 \leq i, j \leq c, \tag{3.14}$$

we see that ϕ appears in the partition function exactly as an extra dimension. The integrals over the matter fields X and ϕ lead to a functional determinant of the Laplacian for the metric $\hat{g}$ on the torus (see e.g. [51], section 10.2, for an explicit calculation). It turns out that the full partition can be written as

$$Z(V) \propto \int_{\mathcal{M}} \mathrm{d}^2 \tau \left(\frac{1}{\tau_2} |\eta(\tau)|^4\right) \left(\tau_2^{1/2} |\eta(\tau)|^2\right)^{-(c+1)}, \tag{3.15}$$

where the first factor comes from $J_{\hat{g}}$ and the second from the integral over ϕ and X. Here $\eta(\tau)$ is the Dedekind function

$$\eta(\tau) = e^{\pi i \tau/12} \prod_{n=1}^{\infty} (1 - e^{2\pi i n \tau}). \tag{3.16}$$

We conclude that

$$Z(V) \propto \int_{\mathcal{M}} \frac{\mathrm{d}^2 \tau}{\tau_2^2} F(\tau)^{c-1}, \tag{3.17}$$

where $F(\tau)$ is a function of the moduli τ that is invariant under the action of the modular group (3.9),

$$F(\tau) = \tau_2^{-1/2} e^{\pi \tau_2/6} \prod_{n=1}^{\infty} |1 - e^{2\pi i n \tau}|^{-2}. \tag{3.18}$$

Notice that, since $F(\tau)$ grows exponentially with τ_2, the partition function (3.17) converges only for $c \leq 1$.

It is precisely this density $F(\tau)^{c-1}$ in moduli space that we want to verify using dynamical triangulations. We will do this both for $c = 0$ and $c = -2$ in section 3.3.

3.2 Assigning moduli to triangulations

Our strategy for assigning moduli to a triangulation of the torus is to first determine such an algorithm for Riemannian manifolds using only differential forms. Then we will mimic the procedure for triangulations using the notion of discrete differential forms.

Suppose we are given a Riemannian metric g_{ab} on the torus. In the previous section we observed that periodic coordinates $0 \leq x^1, x^2 < 1$ exist in which the metric g_{ab} takes the form

$$ds^2 = e^{2\beta\phi}\hat{g}_{ab}(\tau)dx^a dx^b. \tag{3.19}$$

This means that once we have these coordinates we can extract τ_1 and τ_2 simply from the form of the metric. How do we construct the coordinates x^a if we are just given the metric g_{ab}? First of all notice that these coordinates are not unique since the modular group (3.9) acts non-trivially on them. To fix this non-uniqueness, suppose that we are given or that we can construct a pair of simple closed curves γ_1 and γ_2 that generate the fundamental group of the torus. Given such a pair of curves we impose that the coordinate x^1 increases by 1 when running around γ_1 and does not change when running around γ_2, and likewise for x^2. More precisely, in terms of the 1-forms $\alpha^1 = dx^1$ and $\alpha^2 = dx^2$ we demand that

$$\int_{\gamma_i} \alpha^j = \delta_i^j. \tag{3.20}$$

Now, up to constant shifts, the coordinates x^1, x^2 are uniquely determined by (3.19) and (3.20).

To see in what sense the coordinates x^a are special we need to introduce some differential geometry. Let d denote the *exterior derivative* and δ the *divergence* or *co-differential*, which is the adjoint of d with respect to the standard inner product on p-forms,

$$\langle \phi, \psi \rangle = \int \phi \wedge *\psi. \tag{3.21}$$

Here $*$ is the Hodge dual on differential forms[8]. The Hodge Laplacian Δ mapping p-forms to p-forms is defined as

$$\Delta = d\delta + \delta d. \tag{3.22}$$

---

[8]In components, the Hodge dual of a p-form ψ on a n-dimensional Riemannian manifold is defined as:

$$\psi = \frac{1}{p!}\psi_{a_1...a_p} \, dx^{a_1} \wedge \cdots \wedge dx^{a_p},$$

$$*\psi = \frac{\sqrt{g}}{p!(n-p)!} \, \epsilon_{a_1...a_p, b_1...b_{n-p}} \psi^{a_1...a_p} \, dx^{b_1} \wedge \cdots \wedge dx^{b_{n-p}}.$$

The p-forms in its kernel are called *harmonic forms* and according to the Hodge theorem form a linear space with dimension equal to the pth Betti number. In particular, for 1-forms on the torus the space of harmonic forms is two-dimensional and is spanned precisely by the 1-forms $\alpha^i = dx^i$. This follows from the fact that the harmonicity of 1-forms is preserved under conformal transformations and clearly the dx^a are harmonic with respect to the flat, position-independent metric $\hat{g}_{ab}$ in (3.19).

Hence, to construct the coordinates x^a we should solve $\Delta\alpha = 0$, which is equivalent to α having a vanishing curl and divergence,

$$d\alpha = 0 \quad \text{and} \quad \delta\alpha = 0. \tag{3.23}$$

For the two-dimensional space of solutions we choose a basis α^i dual to the γ_j according to (3.20). The coordinates can now be reconstructed from the α^i by integration (the α^i are closed and therefore their integrals do not depend on the chosen path).

We claim that the moduli τ can be directly expressed in terms of the inner products $\langle \alpha^i, \alpha^j \rangle$ through[9]

$$\tau = -\frac{\langle \alpha^1, \alpha^2 \rangle}{\langle \alpha^2, \alpha^2 \rangle} + i \sqrt{\frac{\langle \alpha^1, \alpha^1 \rangle}{\langle \alpha^2, \alpha^2 \rangle} - \left(\frac{\langle \alpha^1, \alpha^2 \rangle}{\langle \alpha^2, \alpha^2 \rangle}\right)^2}. \tag{3.24}$$

To see this notice that it follows from (3.21) and (3.11) that

$$\langle \alpha^i, \alpha^j \rangle = \hat{g}^{ij} \quad \text{and} \quad \langle \alpha^1, \alpha^1 \rangle \langle \alpha^2, \alpha^2 \rangle - \langle \alpha^1, \alpha^2 \rangle^2 = \det \hat{g}^{ab} = 1. \tag{3.25}$$

With the formula (3.24) we have succeeded in expressing the moduli τ completely in terms of the linear spaces of differential forms together with the associated exterior derivatives and inner products. This is a good starting point because these notions can be extended naturally to the piecewise linear geometries encountered in the DT formalism. Let us for the moment assume that we are working in the DT ensemble $\mathcal{T}_3$ (see section 2.1) in which all the triangulations have the structure of a simplicial complex. The construction we are about to discuss can be straightforwardly generalized to the larger ensemble $\mathcal{T}_1$, but various definitions look more natural in the simplicial set-up.

For precise definitions of discrete differential forms on triangulations, for which the geometry is specified by the lengths of the edges, we refer to [42, 43, 69]. In the case of DT the definitions become simpler because all simplices are identical. As a consequence we are closer to the more abstract notion of discrete differential forms on simplicial complexes used in the study of simplicial cohomology (see e.g. [86]).

---

[9]The square root term is just equal to $1/\langle \alpha_2, \alpha_2 \rangle$, but we write it this way to make sure that the expression is independent of the normalization of the inner product $\langle \cdot, \cdot \rangle$.

A discrete p-form ϕ is defined to be a function that associates to each oriented p-simplex σ a real number $\phi(\sigma)$. By definition, if we evaluate ϕ on a simplex σ with reversed orientation we get $-\phi(\sigma)$. In this way the linear space Ω_p of discrete p-forms has a dimension equal to the number of p-simplices in the triangulation. For our purposes we choose the inner product, which is the discrete counterpart of (3.21), to be simply

$$\langle \phi, \psi \rangle = \sum_\sigma \phi(\sigma)\psi(\sigma), \tag{3.26}$$

where the sum is over all oriented p-simplices σ in the triangulation. The exterior derivative $d : \Omega_p \to \Omega_{p+1}$ is defined as

$$(d\phi)(\sigma_{p+1}) = \sum_{\sigma_p \in \sigma_{p+1}} \phi(\sigma_p), \tag{3.27}$$

where the sum is over all p-subsimplices σ_p of σ_{p+1} with the appropriate orientation. As in the continuum we define the divergence $\delta : \Omega_p \to \Omega_{p-1}$ to be the adjoint of d with respect to the inner product (3.26).

Let us make this more explicit for 1-forms on a two-dimensional simplicial complex. We denote simplices by tuples of vertex labels, i.e. we write $\langle ij \rangle$ for a directed edge from vertex i to vertex j and similarly $\langle ijk \rangle$ for a triangle. Then $\phi(\langle ji \rangle) = -\phi(\langle ij \rangle)$ and

$$(d\phi)(\langle ijk \rangle) = \phi(\langle ij \rangle) + \phi(\langle jk \rangle) + \phi(\langle ki \rangle), \quad (\delta\phi)(i) = \sum_{\text{edges}\langle ji \rangle} \phi(\langle ji \rangle). \tag{3.28}$$

The discrete Hodge Laplacian $\Delta = d\delta + \delta d$ can now be represented simply by a square matrix of dimension equal to the number of edges in the triangulation. It can be shown [69] that on a torus triangulation it has a kernel of dimension two, just like in the continuum. In principle we could now use standard numerical linear algebra techniques to compute this kernel for any given triangulation. However, below we will describe a more practical method which directly yields the preferred basis for this kernel.

Before doing this, we need to add one more ingredient to this discrete geometry framework, the discrete counterparts of the curves γ_j in (3.20). In the previous chapter, in section 2.4, we already described an algorithm to construct for a torus triangulation a pair of closed paths γ_j, consisting of a sequence of edges, that generate the fundamental group. Using the natural pairing between discrete paths and discrete 1-forms, we obtain the discrete version of (3.20),

$$\int_{\gamma_j} \alpha^i = \sum_{\langle ij \rangle \in \gamma_j} \alpha^i(\langle ij \rangle) = \delta^i_j. \tag{3.29}$$

A convenient way to find the discrete 1-forms α^i satisfying both $d\alpha^i = \delta\alpha^i = 0$ and (3.29) is to first construct two closed, but not necessarily co-closed, 1-forms β^i dual to
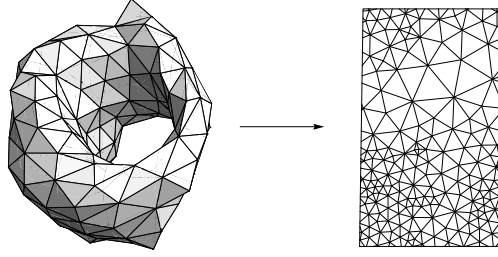
Figure 3.2: *A harmonic embedding of a torus triangulation into a parallelogram in the Euclidean plane.*

the γ_j in the sense of (3.29). This can be done, say, for β^1, by slightly displacing the path γ_2 into a path $\tilde{\gamma}_2$ on the dual 3-valent graph. Then we set $\beta^1(\langle ij \rangle) = 1$ for all the edges $\langle ij \rangle$ that intersect $\tilde{\gamma}_2$ (with the proper orientation) and demand that β^1 vanishes on all other edges. We do the same for β^2, but now we set $\beta^2(\langle ij \rangle) = -1$ for the edges intersecting $\tilde{\gamma}_1$. It follows from the theory of cohomology that $\alpha^i - \beta^i = dx^i$ for a pair of 0-forms x^i, which are of course the discrete counterparts of the coordinates in (3.19). The values x^i on the vertices of the triangulation are then found by solving the matrix equation

$$\Delta x^i = -\delta \beta^i, \tag{3.30}$$

where $\Delta = \delta d$ is now the standard graph Laplacian on the edge graph of the triangulation, i.e.

$$(\Delta f)(i) = \sum_{\text{edges} \langle ij \rangle} (f(i) - f(j)). \tag{3.31}$$

Once we have the 0-forms x^i, we easily obtain the desired harmonic forms $\alpha^i = \beta^i + dx^i$. Finally, we determine the inner products $\langle \alpha^1, \alpha^1 \rangle$, $\langle \alpha^1, \alpha^2 \rangle$, and $\langle \alpha^2, \alpha^2 \rangle$ from (3.26), and plug them into the expression (3.24) to obtain the moduli τ. This value for τ might be outside of the fundamental domain $\mathcal{M}$ that we specified in (3.10). In that case we use the modular transformations (3.9) to map it to $\mathcal{M}$.[10]

A nice by-product of this construction is that we obtain an explicit embedding of the triangulated torus into a parallelogram in the Euclidean plane, determined by the coordinates x^i modulo 1, see figure 3.2. This embedding is harmonic in the sense that every vertex is located at the centre of mass of its neighbours, which is a property that is invariant under linear transformations. The value for τ that we get using the algorithm

---

[10]It turns out that the following algorithm will map any value of τ to $\mathcal{M}$ in a few steps: first move τ to the strip $-1/2 \leq \tau_1 < 1/2$ by shifting τ_1 by some integer; stop if $\tau \in \mathcal{M}$, otherwise map $\tau \to -1/\tau$ and repeat these steps.
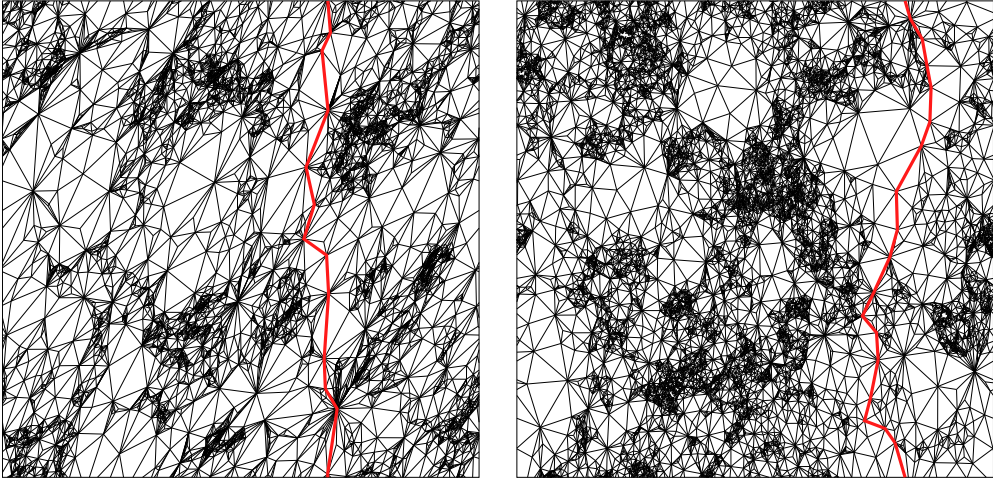
Figure 3.3: *The harmonic embeddings of triangulations with* 150 000 *triangles into the unit square taken from the ensemble for $c = 0$ (left) and $c = -2$ (right). The thick red curve corresponds to the shortest non-contractible loop.*

described above corresponds exactly to the shape of the unit-volume parallelogram that minimizes the total of all squared edge lengths.

The fairly regular torus appearing in figure 3.2 is not a typical triangulation appearing in the DT ensemble. Typical random triangulations tend to be quite wild and have fractal properties, of which one aspect is the presence of baby universes discussed in chapter 2. To illustrate this fractal nature we have plotted in figure 3.3 embeddings into the unit square of two large triangulations, one taken from the DT ensemble of pure gravity $c = 0$ and the other from the ensemble of DT coupled to matter with central charge $c = -2$.

Apart from the overall shape of the parallelogram, which is the main subject of this chapter, these embeddings contain quite a lot of interesting information. For instance, the embedding assigns to each triangle an area with respect to the flat background metric. Since all triangles are identical in the actual geometry we can interpret this area as being proportional to the inverse conformal factor $e^{-2\beta\phi}$. It can be seen that all triangles will have a non-zero area, meaning that they will eventually become visible when zooming in, except those that are contained in a baby universe with neck size $L = 2$ (or $L = 1$). The triangulations in figure 3.3 are from the ensemble $\mathcal{T}_1$ which contains such baby universes, whose general scaling we have discussed in section 2.3. This means that a fraction of the 150 000 triangles is actually invisible in figure 3.3. Measurements show that this fraction is approximately 0.73 for $c = 0$ and 0.46 for $c = -2$. In appendix
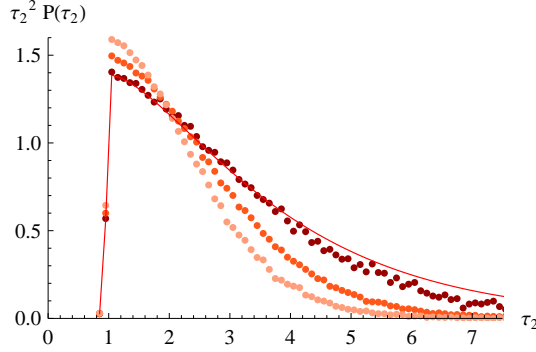
Figure 3.4: *The measured moduli density $P(\tau_2)$ with $N = 8\,000$ for the ensembles $\mathcal{T}_3$ (lightest), $\mathcal{T}_2$ and $\mathcal{T}_1$ (darkest). The theoretical curve for $c = 0$ is shown as a solid line.*

A we show, by renormalizing the propagator for the dual ϕ^3-graph, that this fraction for $c = -2$ as $N \to \infty$ is given analytically by

$$3\frac{2^{12} - 375\pi^2}{675\pi^2 - 2^{12}} \approx 0.46169. \tag{3.32}$$

3.3 Measurement of the moduli distribution

Using the Monte Carlo methods described in section 2.2 we generated a large number of random triangulations in the DT ensemble of pure gravity. Initially we used the ensemble $\mathcal{T}_3$ (see section 2.1), in which different corners of the same triangle are not allowed to be glued and at most one edge is allowed to connect any pair of vertices. For each triangulation we measured the moduli τ in the fundamental domain $\mathcal{M}$ and used these to produce a histogram of the imaginary part τ_2 of τ. The result for $N = 8\,000$ triangles is shown in figure 3.4 (the lightest data points), together with the theoretical values derived from (3.17) by integrating over τ_1. We see a clear deviation from theory which is mainly due to a lack of triangulations with a large value of τ_2.

As is clear from figure 3.1, τ_2 corresponds roughly to the ratio of lengths of the sides of the parallelogram. This means that as far as the flat background geometry is concerned a large value for τ_2 corresponds to a torus that is very elongated in one direction as compared to the other. Of course this does not necessarily reflect a property of the triangulations since we have a (discrete) conformal map in between the triangulation and the flat background. However, on average one would expect a large τ_2 to reflect a torus triangulation with short non-contractible loops in one direction as compared to the

41

loops in other directions. For triangulations appearing in the DT ensemble there are two restrictions entering. By definition, there is a shortest allowed loop length since a loop consists of a number of edges of fixed length. Also for a fixed number of triangles N there is a limit on how long one can make geodesic loops. These restrictions suggest two ways of improving the distribution for large τ_2, either by increasing N or by decreasing the allowed shortest loop length.

The minimal loop length for the ensemble $\mathcal{T}_3$ is three edges. In order to decrease the shortest loop length we have to switch to a different ensemble. In section 2.1 we already introduced the ensemble $\mathcal{T}_1$ in which all 3-valent graphs are allowed as the dual description of the triangulation. This means that loops of length one can occur, i.e. two corners of the same triangle are allowed to be glued. Likewise we can introduce $\mathcal{T}_2$ in which multiple edges are allowed between pairs of vertices but edges may not start and end at the same vertex. The results for the moduli density $P(\tau_2)$ for $\mathcal{T}_2$ and $\mathcal{T}_1$ are shown in figure 3.4 (the middle and darkest data points respectively). Clearly, replacing the ensemble $\mathcal{T}_3$ by the more general ensemble $\mathcal{T}_1$ greatly improves the data quality for fixed number of triangles.

To get even closer to the theoretical curve we have to increase the system size determined by the number of triangles N. Increasing N also increases the simulation run-time significantly, since the number of Monte Carlo moves needed to produce independent configurations grows with N as well as the dimension of the matrix equation (3.30), which we need to solve numerically to determine τ. However, we managed to collect high-precision data for volumes up to $N = 64\,000$. In figure 3.5 the deviation of the data from the theoretical distribution is plotted for volumes $N = 1\,000$ up to $N = 64\,000$, showing a good convergence.

For DT coupled to matter with central charge $c = -2$ the comparison with theory is slightly easier. For $c = -2$ the theoretical distribution falls off like $e^{-\pi\tau_2/2}$ for large τ_2 as compared to the slower fall-off $e^{-\pi\tau_2/6}$ for $c = 0$. Therefore the problematic large-τ_2 configurations contribute less to the partition function. Moreover, we developed a fast numerical method for dynamical triangulations coupled to $c = -2$, which naturally produces random triangulations in the desired ensemble $\mathcal{T}_1$. Already at a volume $N = 8\,000$ the measured distribution $P(\tau_2)$ becomes practically indistinguishable from the theoretical curves, as is shown in figure 3.6. To illustrate how good the agreement is for $N = 8\,000$, we measured the fraction of triangulations having $\tau_2 < 1.5$,

$$P(\tau_2 < 1.5) = 0.64067 \pm 0.00014. \tag{3.33}$$

This is to be compared to the result from Liouville theory

$$P(\tau_2 < 1.5) = \frac{\int_{\mathcal{M}, \tau_2 < 1.5} \frac{\mathrm{d}^2\tau}{\tau_2^2} F(\tau)^{-3}}{\int_{\mathcal{M}} \frac{\mathrm{d}^2\tau}{\tau_2^2} F(\tau)^{-3}} = 0.640648\ldots \tag{3.34}$$
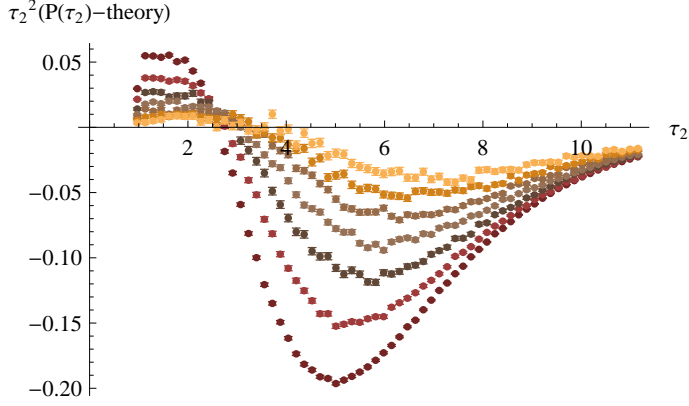
Figure 3.5: *The deviation of $P(\tau_2)$ from the theoretical curve for $c = 0$, ensemble $\mathcal{T}_1$, and volumes N ranging from $1\,000$ (darkest points) up to $64\,000$ (lightest points).*

Let us now have a closer look at the relation between the geometry of the triangulations and the moduli τ. Due to the conformal invariance this relation cannot be very direct. We observed above that short non-contractible loops are important for the large-τ_2 part of the moduli distribution. To quantify this relation we have measured for all generated triangulations the length L of the shortest non-contractible loop in addition to the moduli τ. In section 2.4 we already observed that the distribution of this length L scales with the area as N^{1/d_h} where $d_h = 4$ for $c = 0$ and $d_h \approx 3.56$ for $c = -2$ (see (2.33)). In figure 3.7 we again show the distribution $P(\tau_2)$, this time plotted as a ratio of the theoretical values, for $c = 0$ and $N = 64\,000$, and $c = -2$ and $N = 8\,000$. In addition we have colour-coded the triangulations according to the length L of their shortest loop. Clearly the distribution for large τ_2 is dominated by triangulations that have small loop lengths L.

Presently we do not have a good ansatz for what the combined distribution for τ_2 and L should look like in the continuum $N \to \infty$. One aspect that we can measure is the exponential fall-off with τ_2 if we split the DT-ensemble into subsets according to L. To be precise, let us denote by $P_N(L, \tau_2)$ the fraction of all triangulations with N triangles that have a shortest loop length L and imaginary part of the moduli parameter between $\tau_2 \pm \Delta\tau_2$. Then we fit this distribution to an exponential for large τ_2,

$$P_N(L, \tau_2) \propto e^{-\frac{\pi}{6}\tau_2\beta}. \tag{3.35}$$

The measured values of β are shown in figure 3.8 for $c = 0$ and $c = -2$. The results indicate a universal dependence in terms of the "dimensionless" variable $L/N^{1/d_h}$. What this also shows is that only the sub-ensembles with small L attain the slow fall-off of the
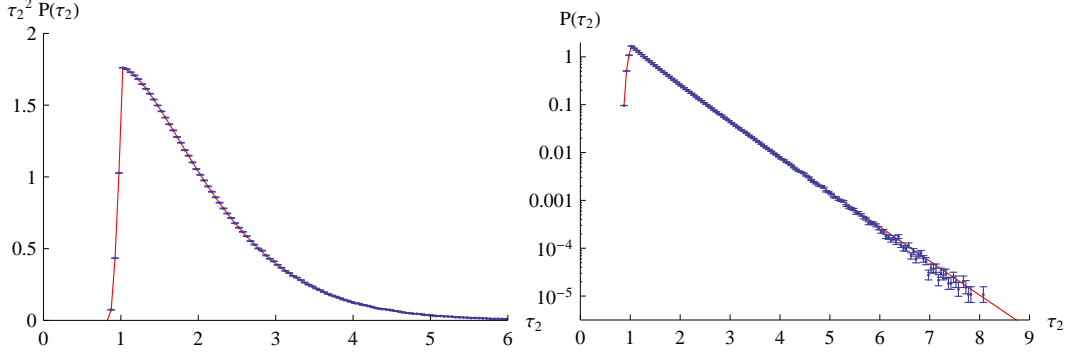
Figure 3.6: *The distribution $P(\tau_2)$ for $c = -2$ with $N = 8\,000$ triangles. The theoretical curves are shown in red.*
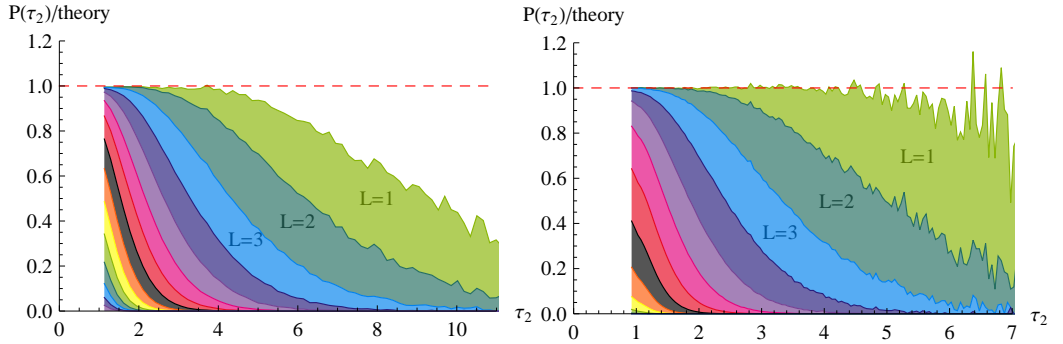

Figure 3.7: *The distribution $P(\tau_2)$ plotted as ratio of the theoretical value. The triangulations appearing in the ensemble are colour-coded according to the length L of their shortest non-contractible loop. The left figure is for $c = 0$ and $N = 64\,000$, the right figure for $c = -2$ and $N = 8\,000$.*
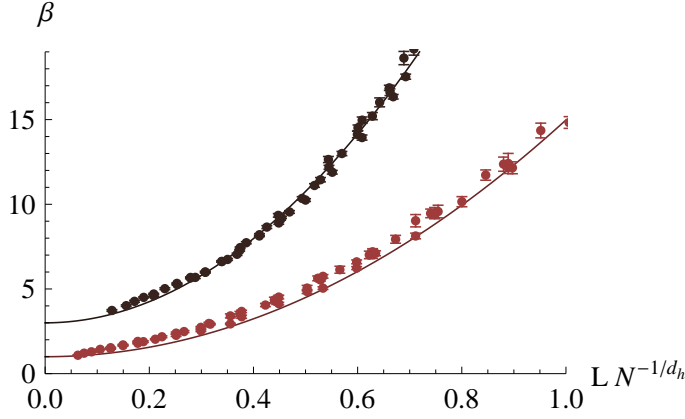
Figure 3.8: *The exponential fall-off $P_N(L, \tau_2) \propto \exp(-\frac{\pi}{6}\tau_2\beta)$ for $c = 0$ (bottom curve) and $c = -2$ (top curve). The fitted curves correspond to $\beta = 1 + 14(LN^{-1/4})^{1.8}$ and $\beta = 3 + 31(LN^{-1/3.56})^{2.0}$. To attain the clean collapse for $c = -2$ we had to perform a small shift $L \rightarrow L - 0.4$ in the length L, which becomes irrelevant in the continuum.*

full distribution, i.e. $e^{-\frac{\pi}{6}(1-c)\tau_2}$ for central charge c.

Thus statistically there is a clear relation between small L in the triangulation and large τ_2 of the conformal embedding in the Euclidean plane. "Small" can be quantified: the typical linear extension of the triangulation will be of the order N^{1/d_h} and "small" means small compared to this linear extension. Finally, let us emphasize that the measurement of a small L in a triangulation does not imply that τ_2 is large. For instance, it can happen that there are two short non-contractible loops that together generate the fundamental group, however, for large N such configurations seem to be rare.

3.4 Discussion and outlook

We have found good agreement between the numerically determined density in moduli space from dynamical triangulations and the analytic results from Liouville theory in the case of pure gravity $c = 0$ and gravity coupled to matter with central charge $c = -2$. A priori it was unclear whether these methods were going to work since the differential geometry techniques we use have only been tested for well-behaved triangulations approximating smooth geometries. The results confirm our intuition that the spaces of differential forms and the linear structures on them are objects that are well-suited for studying the large-scale geometry of triangulations.

Indeed, the moduli may be viewed as describing the degrees of freedom in the geometry of the torus associated with the largest scale, in the sense that they are the only degrees of freedom that remain when inhomogeneities are ironed out. This fact is reflected in the actual construction we discussed in section 3.2: we expressed the moduli solely in terms of harmonic forms, which are extracted from the kernel of the Hodge Laplacian. Usually one interprets the eigenvalues of the Laplacian as representing the length scale (to the power minus two) at which one is probing the geometry, and therefore one can interpret the kernel as corresponding to the largest possible length scale.

The topological nature of the moduli probably explains the small ambiguity in its construction on the triangulation. For instance, in general the precise spectra and eigenspaces of the (Hodge) Laplacians depend on the choice of discrete inner product (3.26). However, it is not easy to write down a combinatorially defined inner product that changes the kernel of the Laplacian on 1-forms and thereby changes the values for the moduli. Alternatively, we could try and deduce the moduli from the dual 1-forms, i.e. the discrete 1-forms that take values on the edges of the dual 3-valent graph (see e.g. [42, 43]). Again, there is no precise relation between discrete forms and the dual discrete forms except in the case of harmonic forms and one can show that the dual analogue of our formula (3.24) leads to exactly the same values for the moduli.

Not only are these results interesting in their own right, but they also give us confidence that similar measurements make sense when we will apply them in chapter 5 to spatial geometries in CDT in 2+1 dimensions. There we do not have a theoretical ansatz for the distribution of moduli, and the continuum limit is not as easily approached as it is here. However, generic geometries appearing in 2d gravity are expected to be wilder than the spatial geometries in CDT. Therefore, if a continuum limit exists in CDT which can be described by a metric, we are confident that these moduli measurements will relate to the moduli of the continuum metric.

Torus universes in CDT

In section 1.1 we have discussed some of the issues of the models of *Euclidean dynamical triangulations* (DT) in three and four dimensions. These are direct generalizations of the two-dimensional model that we investigated in chapters 2 and 3. Contrary to the two-dimensional case few analytic techniques are available to investigate its continuum limit. However, Monte Carlo simulations have revealed a number of properties that already seem to disqualify them in their current form as viable quantum descriptions of gravity. In particular, in three dimensions two phases of the model are identified, a branched polymer phase and a crumpled phase [19, 30, 94]. Typical 3-geometries appearing in either phase have little to do with continuum geometry on any scale. Moreover, the phase transition separating both phases is first order and therefore cannot give rise to a scaling limit.

Several ways of adapting Euclidean dynamical triangulations have been investigated in order to solve these issues. One such attempt that has turned out to be quite successful is the model of *causal dynamical triangulation* (CDT), which will be the subject of this and the next two chapters. The way in which CDT differs from the Euclidean version is in the choice of the ensemble of geometries appearing in the partition function. Instead of summing over all possible triangulations with the desired three-dimensional topology, we restrict to those triangulations that have a foliated structure. What this precisely means will be discussed in section 4.1. Roughly speaking the foliation requirement introduces a notion of time into the system which allows us to view the full 3-geometry as a time evolution of a 2-geometry. By requiring the topology of the 2-geometries not to change in time we are effectively suppressing the appearance of three-dimensional baby universes, i.e. the higher-dimensional analogues of the baby universes discussed in chapter 2. In two dimensions it has been shown explicitly that CDT can be obtained from DT (and vice versa) by surgery of baby universes [5, 16].

The hope is that the foliation will tame the degeneracies in the typical geometries to such a degree that at a large-distance scale a continuum geometry will emerge. Several pieces of evidence in this direction have been gathered in the last decade. In particular, it has been observed that CDT possesses a phase in which the space-time dimension, as measured by the *spectral dimension* both in three [26] and four dimensions [10, 15], approaches the correct continuum value at large distances. This is to be contrasted with DT in three and four dimensions where the Hausdorff dimension diverges in the crumpled phase and is equal to two in the branched-polymer phase.

Another piece of evidence that has boosted the interest in CDT comes from the measurements of spatial volumes in configurations with spherical spatial topology. The expectation values of these observables correspond very closely to the spatial volume profile of Euclidean de Sitter space, i.e. the constant-curvature 3-sphere. These results might lead one to conjecture that in the large-distance limit CDT describes quantum fluctuations around some emergent classical background. If this turns out to be the case, the obvious question to ask is what the equations are that govern the geometry of the classical background. Do they have anything to do with the Einstein equations of general relativity? This brings us to the main question that we will attempt to address in this chapter and the next two: *can we construct an effective action depending on a continuum metric that agrees on the outcome of measurements of large-scale observables in CDT*?

Unfortunately our toolbox of observables in CDT that have an interpretation in terms of large-scale geometry is quite small. At present, it only contains the spatial volumes at different times and their correlations.[11] Still the measurements of these observables provide clues concerning the effective action. In [13] it was shown that the outcome of the measurements are well-described by an effective action for the spatial volumes alone, which can be obtained by evaluating the Euclidean Einstein–Hilbert on a spherical homogeneous cosmology. The main goal of this chapter will be to extend these results to the case of non-trivial spatial topology, namely, that of the torus.

Having an additional non-trivial test of the dynamics of the spatial volume is not our main reason for studying non-trivial spatial topology. In chapter 3 we introduced the moduli as observables in the partition function of two-dimensional triangulations of the torus. These observables can be easily extended to observables in CDT with spatial topology of the torus, by applying them to the two-dimensional triangulations at a fixed time. Having these observables and studying their dynamics is of great importance if we wish to understand better the nature of the large-distance limit in CDT. We know that in general relativity the physical degrees of freedom of the gravitational field reside in the (transverse) traceless components of the metric, i.e. those that capture the local

---

[11]This situation is already much better than it is in DT, where one cannot take advantage of the foliation to define observables at different times and therefore has to resort to full space-time observables.

shape of space rather than the local scale factor.[12] As we will see later, the traceless degrees of freedom enter the Einstein–Hilbert action with the opposite sign in the kinetic term, compared to the pure trace degrees of freedom. This minus sign is at the heart of the *conformal mode problem* of Euclidean gravity: the classical solutions to the Euclidean Einstein equations are not (local) minima of the Euclidean Einstein–Hilbert action. To see if and how CDT deals with this unboundedness it is necessary to probe both pure trace and traceless degrees of freedom of the geometry. This is achieved by the spatial volume and the moduli as observables. They are distinguished examples of observables measuring respectively trace and traceless degrees of freedom in that they probe the geometry at the largest possible scale. They are also the only degrees of freedom remaining in the presence of homogeneity. This opens up the possibility of comparing the measurements of these observables to minisuperspace actions of homogeneous torus universes.

This chapter may be viewed as a preparation for the program outlined above. First we will introduce the set-up of CDT in 2+1 dimensions and discuss suitable boundary conditions. Then we will attempt to compare the measured expectation values of the spatial volume to classical solutions that we derive from the Euclidean Einstein–Hilbert action. Finally, we consider the correlations in the quantum fluctuations of the spatial volume, which will give us some non-trivial information about kinetic term in the effective action.

4.1 Causal dynamical triangulation in 2+1 dimensions

Given a pair of metrics g_{ab} and g'_{ab} on a two-dimensional manifold Σ, we can write the formal statistical path integral

$$Z[g_{ab}, g'_{ab}] = \int \frac{\mathcal{D}g}{\text{Diff}} \exp(-S[g]). \tag{4.1}$$

The integral is over three-dimensional geometries on the space-time manifold $[0, 1] \times \Sigma$, which are redundantly parametrized by metrics $g_{\mu\nu}$ that reduce to g_{ab} and g'_{ab} when restricted to the initial and final boundary respectively. The redundancy, determined by the action of the diffeomorphism group, is to be factored out in order not to overcount the physical configurations.

Causal dynamical triangulations (CDT) is a particular regularization of this path integral which turns the infinite-dimensional integral into a discrete sum. This is achieved

---

[12]This point has been much emphasized by York in the context of the initial value problem of GR [109, 110] and was the inspiration for the development of Shape Dynamics, which we will discuss in chapter 7.
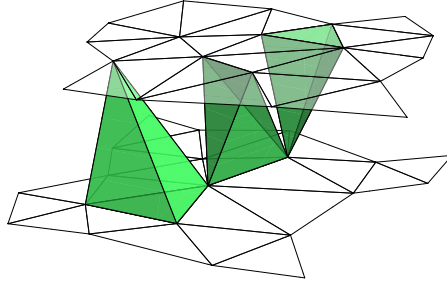
Figure 4.1: *Different types of simplices: a 31-simplex, a 22-simplex and a 13-simplex.*

by restricting the ensemble of geometries to piecewise linear geometries of a specific form. Roughly speaking, we restrict the geometries to consist of a fixed number T of slices consisting of three-dimensional simplices. For this to make sense, we must first assume that the boundary geometries g_{ab} and g'_{ab} correspond to two-dimensional triangulations $\mathbf{T}_0$ and $\mathbf{T}_T$ that are built from equilateral triangles, just like the ones we discussed in chapters 2 and 3. We choose a time coordinate t on our three-dimensional geometry that is equal to 0 on the initial boundary and equal to T on the final boundary. The *spatial geometries* at each intermediate time step $t = 1, 2, \ldots, T - 1$ are required to be of the form of a two-dimensional equilateral triangulation $\mathbf{T}_t$. The space-time in between two spatial triangulations $\mathbf{T}_t$ and $\mathbf{T}_{t+1}$ is filled with tetrahedra making the three-dimensional geometry into a simplicial manifold. To be more precise, we allow tetrahedra of three types, 31-simplices, 22-simplices and 13-simplices, according to the distribution of their vertices into consecutive spatial slices (figure 4.1). Finally, we restrict all tetrahedra of a particular type to be geometrically identical. In particular, this implies that all the edges connecting consecutive slices, which we will refer to as *timelike edges*, are assumed to have equal length. The same holds for all *spacelike edges*, i.e. the edges that are contained in the spatial triangulations.

The main advantage of taking identical building blocks is that we can now describe the geometry purely combinatorially. To specify a triangulation we only need to keep track of a finite list of numbers describing the adjacency of the simplices, e.g. in the form of an adjacency matrix. This way the ensemble of geometries in the path integral (4.1) becomes a discrete set $\mathcal{T}$ of three-dimensional triangulations $\mathbf{T}$. The partition function for CDT becomes

$$Z_{\text{CDT}}[\mathbf{T}_0, \mathbf{T}_T, T] = \sum_{\mathbf{T} \in \mathcal{T}} \frac{1}{C_{\mathbf{T}}} e^{-S_{\text{CDT}}[\mathbf{T}]}, \tag{4.2}$$

where $C_{\mathbf{T}}$ is the order of the automorphism group of the triangulation $\mathbf{T}$ and the action
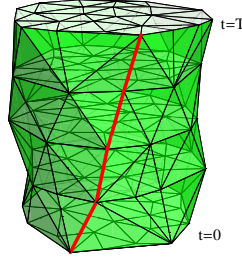
Figure 4.2: *Any vertex in the final boundary of a CDT geometry has a fixed edge-distance T to the initial boundary.*

$S_{\mathrm{CDT}}[\mathbf{T}]$ can only depend on the combinatorics of $\mathbf{T}$. We take this action to be the Euclidean Einstein–Hilbert action evaluated on the piecewise linear manifold corresponding to the triangulation $\mathbf{T}$, which (according to [13]) leads to

$$S_{\mathrm{CDT}}[\mathbf{T}] = k_3 N_3 - k_0 N_0, \tag{4.3}$$

in terms of the number N_0 of vertices and the number N_3 of tetrahedra. The couplings k_0 and k_3 can be expressed in terms of Newton's constant, the cosmological constant, and the spacelike and timelike edge lengths, but the precise expressions are of little interest here. The important point is that the Einstein–Hilbert action yields a function which is linear in the number of simplices of various dimensions. It is also the most general such expression, since the number of triangles and the number of edges can be expressed in terms of N_0 and N_3, and the same holds for the number of 31-simplices, 22-simplices and 13-simplices. It also means that the choice of spacelike and timelike edge lengths does not affect the CDT partition function other than renormalizing the bare Newton's constant and cosmological constant.

We can view the foliation in CDT as a discrete analogue of the proper-time (or rather proper-distance) foliation of a Riemannian manifold. If we define the *edge distance* between two vertices as the minimal number of edges connecting them, any vertex in the spatial triangulation $\mathbf{T}_t$ has a fixed edge distance t to the initial boundary. In particular, both boundaries are separated by a fixed distance T in lattice units, see figure 4.2. We will see later that this feature has important consequences for the classical limit of the theory.

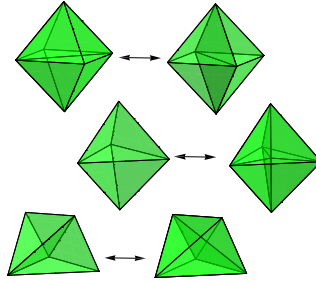The partition function Z_{CDT} can be used to define the expectation value of an ob-

Figure 4.3: *A set of local update moves on the CDT configurations.*

servable $\mathcal{O} : \mathcal{T} \to \mathbb{R}$ according to

$$\langle \mathcal{O} \rangle = \frac{1}{Z_{\text{CDT}}} \sum_{\mathbf{T}} \frac{\mathcal{O}(\mathbf{T})}{C_{\mathbf{T}}} e^{-k_3 N_3 + k_0 N_0}. \tag{4.4}$$

In Monte Carlo simulations of CDT we can measure these expectation values for certain observables, but we do not have direct access to the transition amplitude $Z[\mathbf{T}_0, \mathbf{T}_T]$ as function of the boundary geometries. In practice we therefore try to avoid putting in artificial boundary geometries $\mathbf{T}_0$ and $\mathbf{T}_T$. One reason is that we do not know what generic spatial geometries look like in CDT; an ad hoc boundary geometry constructed by hand might well affect the simulation in a way that we have no control over. The standard approach is to avoid boundaries altogether by making time periodic, such that the topology of the triangulation becomes $S^1 \times \Sigma$. Another option is to take $\mathbf{T}_0$ and $\mathbf{T}_T$ to be singular such that the spatial volume shrinks to zero when approaching the boundary.

To approximate expectation values of observables using Monte Carlo simulations we need to generate a large set of random CDT configurations according to the Boltzmann distribution in (4.2). As in the case of the 2d dynamical triangulations described in section 2.2, this can be accomplished by a Markov process. We start by constructing by hand a triangulation $\mathbf{T}$ with the desired topology and satisfying the desired boundary conditions. We then apply a large number of random update moves on $\mathbf{T}$, where each move occurs with a probability carefully chosen to satisfy a detailed balance condition. In the case of CDT in 2+1 dimensions a suitable set of local update moves is shown in figure 4.3, see [12, 13] for more details.

4.2 Torus universes

Let us now restrict the spatial topology Σ to that of the torus. The goal of this section is to present an initial investigation of the spatial volume profiles in the CDT simulations and to determine which boundary conditions yield the most interesting dynamics. We first consider periodic boundary conditions, which have been extensively used in CDT with spherical spatial topology in both three and four dimensions.

It is important to note that periodic boundary conditions imply that there is a time translation symmetry present in the system. This means that shifting the time $t \to t+1$ (modulo T) maps the ensemble $\mathcal{T}$ of CDT configurations to itself and leaves the action S_{CDT} invariant. A consequence of the time translation symmetry is that strictly speaking the spatial volume profile $\langle V(t) \rangle$ is time-independent and therefore contains little information. However in the spherical case it has been observed, both in three [13] and four dimensions [14], that the time translation symmetry is spontaneously broken for sufficiently large time extent T. The simplices do not distribute homogeneously in time, but condense into a subinterval in time with macroscopic spatial volumes, while the remaining time slices acquire a minimal spatial volume. To obtain a non-trivial profile the spatial volumes are not averaged at fixed time t but at a fixed time t' with respect to the centre of the extended region. The resulting volume profile is illustrated in figure 4.4, which shows a typical volume distribution $V(t')$ together with its expectation value $\langle V(t') \rangle$. To high accuracy the expectation value $\langle V(t') \rangle$ coincides with the spatial volume of a proper-time foliation of the 3-sphere, leading to the conjecture that Euclidean de Sitter space emerges from CDT on the sphere in 2+1 dimensions.

A similar behaviour might be expected for CDT on the torus, however we have not observed any such breaking of the time translation symmetry in our simulations. In none of the simulations we performed, with a wide range of three-volumes, time extents T, and couplings k_0, did we observe any tendency of spatial slices to degenerate to minimal-volume configurations. This is illustrated on the right-hand side of figure 4.4, which shows a typical volume profile from a CDT simulation with $T = 70$ time slices. Of course, the absence of degenerate spatial geometries does not prove that the classical limit has time translation symmetry. A more detailed analysis, for instance involving the distribution of Fourier modes of $V(t)$, would be necessary to make more definite statements.

One might wonder which feature of the torus topology in CDT is responsible for the quite different behaviour when compared to spherical topology. One way in which the CDT configurations are different is in the number of triangles in a minimal triangulation of Σ. In the case of the sphere the minimal configuration is given by the boundary of a tetrahedron, which consists of four triangles. A triangulation of the torus, however,
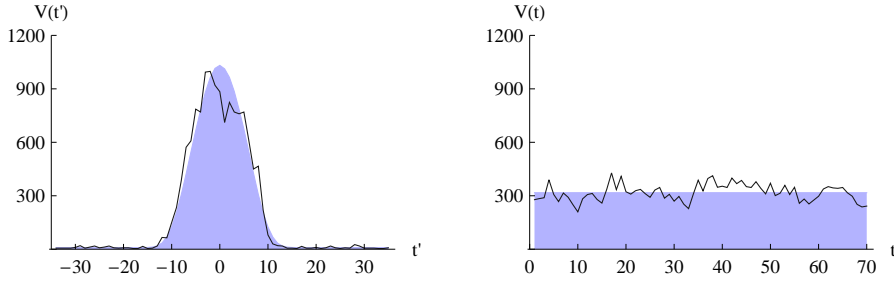
Figure 4.4: *Volume profiles of CDT with topology $S^1 \times S^2$ (left) and $S^1 \times T^2$ (right). The solid curves represent typical configurations, while the shaded areas correspond to the expectation values $\langle V(t') \rangle$ and $\langle V(t) \rangle$ respectively.*

requires a minimum of 14 triangles and therefore we need substantially more tetrahedra to produce a "stalk" of minimal spatial volume. It could be that the extra cost of the stalk (as measured by the N_3-term in the CDT action) is no longer outweighed by the entropic gain of the tetrahedra clumping together. Perhaps this is not the full story, since it seems to imply that the macroscopic ground state of the system depends sensitively on the microscopic details. Hopefully we will be able to give a more satisfactory explanation once we understand better the effective dynamics of CDT.

Without symmetry breaking there is little we can learn from measurements of the spatial volume. One way to produce a non-trivial time dependence of the spatial volume is by explicitly breaking the time translation symmetry of the action. For instance, we could insert a time-dependent coupling $k_2(t)$ for the number $N_2(t)$ of spatial triangles at time t:

$$S_{\text{CDT}}[\mathbf{T}] = k_3 N_3 - k_0 N_0 + \sum_{t=1}^{T} k_2(t) N_2(t). \tag{4.5}$$

Such a coupling has an interpretation in the continuum as a time-dependent cosmological constant, which acts as a source for the spatial volume.

In this chapter we will take another approach which involves trading the periodic boundary conditions for fixed boundaries. In the case of spherical spatial topology it is hard to imagine that fixing the boundaries at $t = 0$ and $t = T$ to minimal triangulations (or zero volume if allowed by the simulation code) will affect the overall volume profile other than introducing some minor boundary artefacts. By contrast, similar boundaries for CDT on the torus will presumably have a major impact on the dynamics of the spatial volume, since minimal spatial volumes do not occur with periodic boundary
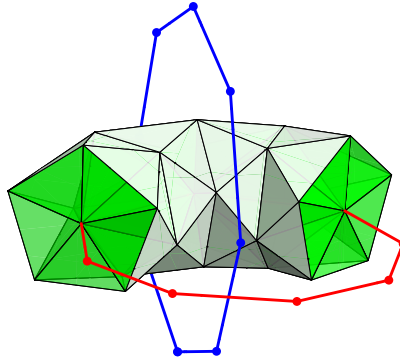
Figure 4.5: *A degenerate initial boundary at $t = 0$ consisting of $l_0 = 8$ edges (solid red curve). The light triangles belong to the triangulation at $t = 1$. If we choose the final singularity according to the blue curve, we end up with the Hopf foliation of S^3.*

conditions. In addition to a non-trivial volume profile we would also like the shape of the tori to evolve in time. This can be achieved by taking an initial torus elongated in one direction and a final torus elongated in the other direction. If we try to produce boundary triangulations with such geometries, we need a lot of boundary triangles and there is quite some ambiguity in the way we put them together. Luckily, we have an easier option, namely, to take the boundary to be completely degenerate in one of the two directions, resulting in a one-dimensional circle consisting of a number l_0 of edges instead of a two-torus. As an example we have depicted in figure 4.5 a portion of a CDT configuration with an initial boundary consisting of $l_0 = 8$ edges.

With this choice, the topology of the space-time region $0 \leq t \leq t'$ for some $0 < t' < T$ becomes that of a solid torus. If we impose similar boundary conditions on the final boundary, the same will hold for the region $t' \leq t \leq T$. Therefore the most general space-time topology is that of a pair of solid tori glued along their boundaries (in this case corresponding to the torus at time t'). This can be done in several ways, giving rise to $S^2 \times S^1$, S^3, or more generally a *lens space $L(p,q)$* (see e.g. [64]). For our purposes the second option is the most interesting, because it is the simplest topology that allows for a non-trivial shape evolution. It is achieved by taking the initial and final singularity such that together they form the so-called *Hopf link* in S^3. This is illustrated in figure 4.5, in which the final singularity is shown in blue and the embedding space $\mathbb{R}^3$ represents S^3 with one point removed (e.g. after stereographic projection). The foliation of the 3-sphere by tori that we obtain in this way is known as the *Hopf foliation*, see also figure 4.7.
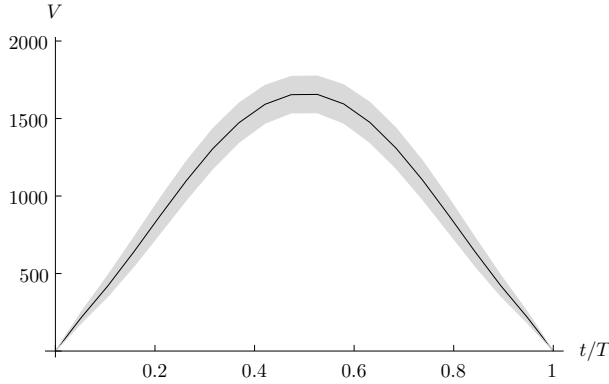
Figure 4.6: *Volume profile for $N_3 = 60\,000$ with boundaries consisting of $l_0 = 60$ edges and $k_0 = 2.5$. The shaded area corresponds to the standard deviation in $V(t)$ and gives an idea of the size of the quantum fluctuations. Error bars are not shown but they are of the order of 0.1%.*

The results that we will present in this chapter are based on CDT simulations with a time extent $T = 19$ and, unless indicated otherwise, we take the length l_1 of the final singularity at $t = T$ to be identical to the length l_0 of the initial singularity at $t = 0$ in order to maintain time-reversal symmetry. In figure 4.6 the expectation value $\langle V(t) \rangle$ of the spatial volume is shown for a simulation with fixed number $N_3 = 60\,000$ of tetrahedra, boundary length $l_0 = 60$, and coupling $k_0 = 2.5$. We observe a clear expansion of the volume at early times and a contraction at late times, indicating non-trivial dynamics of the spatial volume. Moreover, the expansion close to the singularity is roughly linear, which is in accordance with the initial geometry being one-dimensional. Before we start exploring various other values of N_3, l_0, and k_0, let us see what classical solutions we might expect from general relativity.

4.3 Classical solutions

Classical solutions of general relativity with Euclidean signature are given by the stationary points of the Euclidean Einstein–Hilbert action

$$S_{EH}[g_{\mu\nu}] = -\kappa \int \mathrm{d}^3x \sqrt{g}(R - 2\Lambda). \tag{4.6}$$

Its Euler–Lagrange equations are known as the Einstein equations

$$R_{\mu\nu} - \frac{1}{2}R\,g_{\mu\nu} + \Lambda\,g_{\mu\nu} = 0, \tag{4.7}$$

which in three dimensions are equivalent to (see e.g. [35])

$$R_{\mu\nu\rho\sigma} = \Lambda(g_{\mu\rho}g_{\nu\sigma} - g_{\mu\sigma}g_{\nu\rho}). \tag{4.8}$$

Hence, solutions have constant Riemann curvature and are therefore locally isometric to the 3-sphere ($\Lambda > 0$), flat Euclidean space ($\Lambda = 0$) or hyperbolic space ($\Lambda < 0$), depending on the sign of the cosmological constant. As a consequence, classical general relativity in three dimensions has no local degrees of freedom.

To find the solutions explicitly we switch to the ADM formalism, i.e. we rewrite the metric $g_{\mu\nu}$ in terms of a spatial metric g_{ab}, a shift vector N^a and lapse N,

$$ds^2 = N^2 dt^2 + g_{ab}(dx^a + N^a dt)(dx^b + N^b dt). \tag{4.9}$$

In terms of these the Einstein–Hilbert action becomes

$$S_{ADM}[g_{ab}, N^a, N] = -\kappa \int \mathrm{d}t \int \mathrm{d}^2 x \sqrt{g} N \left(K^2 - K_{ab}K^{ab} + R - 2\Lambda \right), \tag{4.10}$$

where R now refers to the two-dimensional curvature and K_{ab} is the extrinsic curvature tensor

$$K_{ab} = \frac{1}{2N} \left(\dot{g}_{ab} - \nabla_a N_b - \nabla_b N_a \right). \tag{4.11}$$

The only difference with the (usual) Lorentzian case is the minus sign in front of the kinetic term $K_{ab}K^{ab} - K^2$. If one puts the lapse N to 1, the set of constant-t surfaces defines a proper-time foliation for the space-time manifold. Hence, the gauge $N = 1$ is particularly useful when comparing to CDT.

We can find the classical solutions by putting (4.10) into canonical form (see [85] or [35]) and imposing the constant mean curvature (CMC) gauge condition in which one can solve the dynamics completely.[13] In this gauge the classical solutions for the torus can be shown to be spatially flat. The lapse only depends on time while we can choose the shift to vanish, which means that on shell the foliation fixed by the CMC gauge is a proper-time foliation (up to a reparametrization of the time variable).

It follows that in general all solutions can be obtained from a minisuperspace model where we impose spatial homogeneity from the outset. To achieve this, let us put

---

[13]Of course, the situation is slightly different than usual, since we are considering Euclidean gravity instead of Lorentzian gravity. Hence, we cannot be sure that we capture all possible solutions. This is not really a problem, since we are interested in a limited class of solutions matching our boundary conditions.

$N = N(t)$, $N^a = 0$ and $g_{ab}(t) = V(t)\hat{g}_{ab}(\tau_i(t))$, where $\hat{g}_{ab}(\tau_i)$ is the flat unit-volume metric on the torus parametrized by the moduli τ_1 and τ_2 (see (3.11) from chapter 3),

$$\hat{g}_{ab}(\tau) = \frac{1}{\tau_2} \begin{pmatrix} 1 & \tau_1 \\ \tau_2 & \tau_1^2 + \tau_2^2 \end{pmatrix}. \tag{4.12}$$

Plugging this ansatz into (4.10) we obtain the minisuperspace action

$$S[V, \tau_i, N] = \kappa \int \mathrm{d}t \left(\frac{1}{2N} \left(-\frac{\dot{V}^2}{V} + V\frac{\dot{\tau}_1^2 + \dot{\tau}_2^2}{\tau_2^2} \right) + 2N\Lambda V \right). \tag{4.13}$$

To find the classical solutions, we identify two conserved quantities, E and p, given by

$$E = -\frac{1}{2N} \left(-\frac{\dot{V}^2}{V} + V\frac{\dot{\tau}_1^2 + \dot{\tau}_2^2}{\tau_2^2} \right) + 2N\Lambda V, \tag{4.14}$$

$$p = \frac{V}{N} \frac{\sqrt{\dot{\tau}_1^2 + \dot{\tau}_2^2}}{\tau_2}. \tag{4.15}$$

Moreover, variation with respect to the lapse $N(t)$ yields the initial value condition $E = 0$. Imposing the proper-time gauge $N = 1$, we easily find the most general solution for the spatial volume $V(t)$ up to time translation and time reversal,

$$V(t) = \begin{cases} \frac{p}{2\sqrt{\Lambda}} \sin(2\sqrt{\Lambda}\,t) & \text{if } \Lambda > 0 \\ p\,t & \text{if } \Lambda = 0 \\ \frac{p}{2\sqrt{-\Lambda}} \sinh\left(2\sqrt{-\Lambda}\,t\right) & \text{if } \Lambda < 0. \end{cases} \tag{4.16}$$

In addition, we have the static solution $\dot{V} = p = 0$ for $\Lambda = 0$[14] and an exponentially expanding solution $V(t) = \exp\left(2\sqrt{-\Lambda}t\right)$ and $p = 0$ for $\Lambda < 0$.

Only for $\Lambda > 0$ we get a solution with both an initial and a final singularity, at $t = 0$ and $t = T = \pi/(2\sqrt{\Lambda})$ respectively. In general the modular parameter $\tau = \tau_1 + i\tau_2$ will traverse a geodesic in the Poincaré upper half-plane, which is the genus-1 Teichmüller space, with speed determined by p in (4.15). When approaching either of the singularities, τ will hit the boundary of Teichmüller space and therefore lead to degenerate tori at the boundaries. In particular, the boundary conditions $\tau(0) = 0$ and $\tau(T) = i\infty$ give precisely the Hopf foliation of the 3-sphere, which we described in the last section. The

---

[14]Notice that general relativity with spherical spatial topology does not have such a static solution due to presence of a spatial curvature term. We could view this as an explanation for the breaking of time translation symmetry in the spherical case. However, this fact relies crucially on the initial value condition $E = 0$, which we will revisit below.
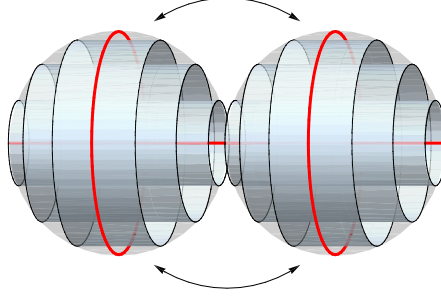
Figure 4.7: *The Hopf foliation of the 3-sphere, which is depicted by two 3-balls with their spherical boundaries identified. The red curves denote the initial and final singularity.*

general solution with these boundary conditions is parametrized by the lengths l_0 and l_1 of the singularities and is given by the space-time metric

$$ds^2 = dt^2 + l_0^2 \cos^2(\sqrt{\Lambda}\, t)dx^2 + l_1^2 \sin^2(\sqrt{\Lambda}\, t)dy^2. \tag{4.17}$$

The three-volume V_3 of this geometry is $V_3 = l_0 l_1/(2\sqrt{\Lambda})$, which directly relates the cosmological constant Λ and the volume V_3.

When we try to compare the corresponding volume profile

$$V(t) = \frac{l_0 l_1}{2} \sin(2\sqrt{\Lambda}\, t) \tag{4.18}$$

to measurements in CDT simulations, we immediately run into a difficulty. The time extent $T = \pi/(2\sqrt{\Lambda})$ of the classical solution (4.18) is fixed in terms of Λ or, equivalently, in terms of the three-volume and the boundary conditions. However, in our CDT simulations the time extent T appears as an additional free parameter set by hand.

This is a specific case of the more general issue of comparing CDT to general relativity. As we mentioned in section 4.1 the configurations appearing in the CDT ensemble all have roughly constant distance T between their boundaries. This means that any "average" continuum geometry emerging from such an ensemble in a classical limit will have the same property. Assuming that an effective action in terms of a continuum metric exists that describes the classical limit, the classical solution should arise at its stationary point when restricted to the ensemble of geometries having fixed distance T between the boundaries. Such an ensemble of geometries is most easily characterized in proper-time gauge. It contains the geometries that allow a metric with lapse $N = 1$ and boundaries occurring at $t = 0$ and $t = T$.

If we take the Einstein–Hilbert action as ansatz for the effective action, we should, according to the previous discussion, not take into account the equation of motion obtained by varying the lapse N. This means that

$$\frac{\delta S}{\delta N}\bigg|_{N=1} = \sqrt{g}(K_{ab}K^{ab} - K^2 + R - 2\Lambda) \tag{4.19}$$

should no longer be required to vanish, although its constancy in time is guaranteed by the other equations of motion. To summarize, in order to take into account the fixed time extent T, we should consider the equations of motion of the ADM action in which we put $N = 1$,

$$S[g_{ab}, N^a] = -\kappa \int_0^T \mathrm{d}t \int \mathrm{d}x \sqrt{g}\left(K^2 - K_{ab}K^{ab} + R - 2\Lambda\right). \tag{4.20}$$

Effectively we lose one of the Einstein equations and therefore the number of local physical degrees of freedom increases from zero to one. From the canonical point of view we lose the Hamiltonian constraint, which normally allows us to solve for the trace part of the spatial metric in terms of the traceless degrees of freedom.

Let us now see what effect this has on the family of homogeneous solutions for the torus universe.[15] We still have the conserved quantities E and p from (4.14) and (4.15) with N set to one. However, now E is not required to vanish and therefore it serves as an additional parameter in the family of solutions, which we can tune to arrive at the desired time extent T. Restricting to the solutions with two singularities and non-vanishing p, we find a family of volume profiles,

$$V(t) = \begin{cases} l_0 l_1 \frac{\sinh\left(\sqrt{-\Lambda}(T-t)\right)\sinh\left(\sqrt{-\Lambda}\,t\right)}{\sinh^2\left(\sqrt{-\Lambda}\,T\right)} & \text{if } \Lambda < 0 \\ l_0 l_1 (T-t)t/T^2 & \text{if } \Lambda = 0 \\ l_0 l_1 \frac{\sin\left(\sqrt{\Lambda}(T-t)\right)\sin\left(\sqrt{\Lambda}\,t\right)}{\sin^2\left(\sqrt{\Lambda}\,T\right)} & \text{if } 0 < \Lambda < \left(\frac{\pi}{T}\right)^2. \end{cases} \tag{4.21}$$

For fixed l_0, l_1, and T, the three-volume increases monotonically as a function of Λ from $V_3 = 0$ at $\Lambda = -\infty$ to $V_3 = \infty$ at $\Lambda = (\pi/T)^2$. In figure 4.8 we have plotted the volume profiles normalized by their time average $V_{\mathrm{av}} = V_3/T$ for various values of Λ. The shape of the profile only depends on the dimensionless quantity $v = V_3/(l_0 l_1 T)$. For $v \to 0$ we find a flat profile, for $v = 1/6$ a parabola, for $v = 1/\pi$ a sine, and for $v \to \infty$ a sine-squared profile.

---

[15]Contrary to the general relativistic case, homogeneity here is a non-trivial restriction of the full set of solutions to (4.20). There is an infinite-dimensional family of classical solutions due to the presence of a local degree of freedom. Only when the boundary conditions are homogeneous, which is the case we are interested in, can we safely assume homogeneity of the solutions.
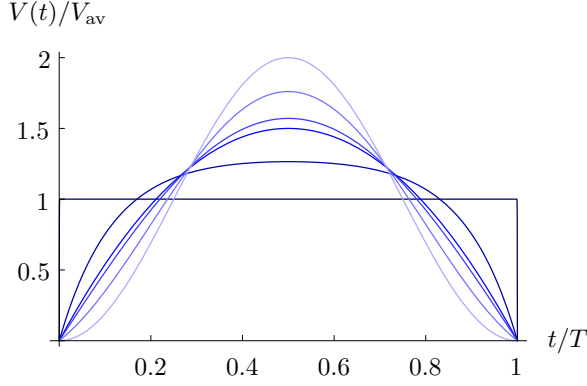
Figure 4.8: *The spatial volume $V(t)$ from (4.21) normalized by its time average $V_{\mathrm{av}} = V_3/T$ for different values of $v = V_3/(l_0 l_1 T)$. The curves, from dark to light, correspond to $v = 0$ (flat), $v = 0.01$, $v = 1/6$ (parabola), $v = 1/\pi$ (sine), $v = 2$, and $v = \infty$ (sine squared).*

4.4 Measurement of volume profiles

Now that we have a proper ansatz for the classical trajectories let us return to the data from our Monte Carlo simulations. Since we have a wide range of shapes available as classical volume profiles, it is perhaps no surprise that we can find relatively good fits to most of the experimental data. The expectation values $\langle V(t) \rangle$ shown in figure 4.6 are well described by the volume profile corresponding to a value $v = 0.98$ (see figure 4.8).

To see whether our simulations can reproduce volume profiles in our simulations with a wider range of shapes, we should vary some of the free parameters in our partition function. In the current set-up there are four such parameters (five if we count the boundary lengths l_0 and l_1 separately): the time extent T, the discrete three-volume N_3, the coupling k_0, and the boundary length l_0. Probing the full parameter space would have been too time-consuming, therefore we decided to fix the three-volume to $N_3 = 60\,000$ and the time to $T = 19$ and perform simulations for a wide range of values of the coupling k_0 and the boundary length l_0.

To determine the relevant range of couplings k_0 we should first briefly discuss the phase diagram of CDT in 2+1 dimensions. Remember that our original CDT action (4.3) contained two couplings, k_0 and k_3. To approach a continuum limit the coupling k_3 is decreased towards a critical line, at which the expectation value of the three-volume N_3 diverges. However, in practice we work with an ensemble in which the system size N_3 is fixed and the continuum limit is approached by increasing N_3. In any case,
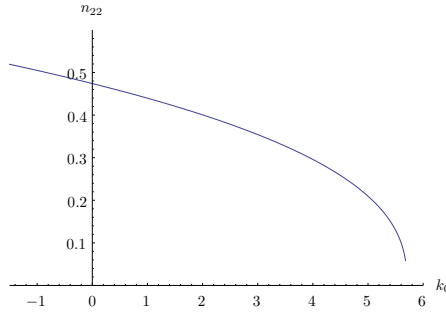
61

Figure 4.9: *The fraction n_{22} of simplices of type 22 as function of the coupling k_0.*

what remains is a one-dimensional phase space parametrized by k_0. It is not hard to see that the effect of increasing k_0 is to reduce the number of 22-simplices in favour of 31-simplices and 13-simplices. As k_0 approaches the critical value $k_0^* \approx 5.6$ the fraction n_{22} of simplices of type 22 collapses to (nearly) zero, see figure 4.9. Since the 22-simplices provide the coupling between consecutive spatial triangulations, we find that the spatial geometries in the phase $k_0 > k_0^*$ are uncoupled and therefore the space-time geometry loses its physical interpretation. We are interested in a classical limit and therefore restrict our attention to the "physical" phase $k_0 < k_0^*$. We also make sure not to come too close to the phase transition where the fluctuations in the spatial volume are large.

In figure 4.10a we show the results for fixed $l_0 = 60$ and k_0 varying from 1.0 to 5.0 in steps of 0.5. Clearly, as we increase k_0 towards the phase transition, the shape of the volume profile becomes flatter, which corresponds to the parameter v approaching zero. This is in accordance with the discussion above, since a complete decoupling of the spatial triangulations would lead to a flat volume profile with $v = 0$.

In figure 4.10b we fixed $k_0 = 2.5$ but took for the boundary length l_0 the values 5, 20, 40, 60, 80, 120, and 180. As we decrease l_0 we observe an approach towards the sine-squared shape, i.e. $v \to \infty$. If we had been confident about the system being well approximated by the classical minisuperspace description, we would quantitatively test the classical relation $v = V_3/(Tl_0^2)$.[16] However, as we will argue in a moment we should probably not put too much trust in this classical description.

---

[16]Even if the minisuperspace formulation is a good approximation, we would probably find deviations from the power-law dependence $v \propto l^{-2}$, which we would interpret as a renormalization of the boundary length. It might well be that the path determined by the singularity shows some random walk behaviour in the three-dimensional triangulation, leading to an anomalous scaling of the continuum singularity length with the discrete l_0.
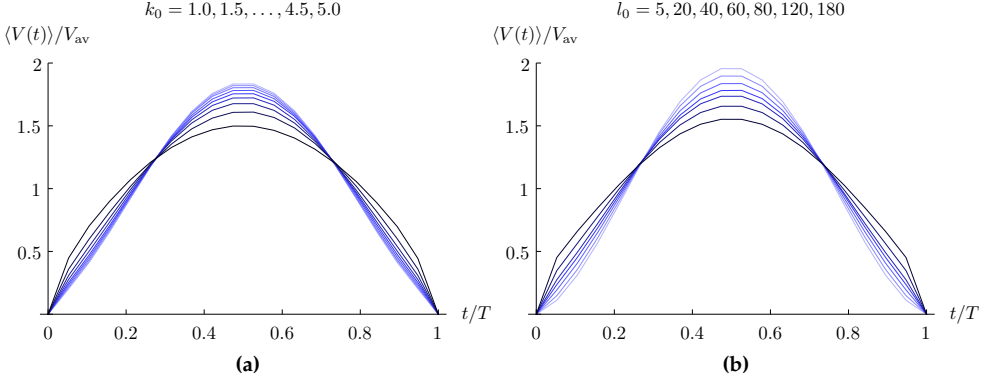
Figure 4.10: *The normalized volume profiles for several simulations with $N_3 = 60\,000$: (a) $l_0 = 60$ and different values of k_0 and (b) $k_0 = 2.5$ and different boundary lengths. The lightest curves correspond to $k_0 = 1.0$ and $l_0 = 5$ respectively.*

The qualitative similarity between the measurements and the classical solutions may be due to the rather generic nature of the classical volume profiles, which represent roughly the smoothest profiles with a given slope and time-reversal symmetry. More significant tests of the hypothesized classical limit would involve studying higher-order corrections to the volume profile. The situation is different when we drop the time reversal symmetry in CDT, by using unequal boundary lengths l_0 and l_1. The classical solutions (4.21) yield a non-trivial prediction in this case, namely, that the volume profile remain symmetric. To test this prediction we performed simulations with fixed initial singularity length $l_0 = 60$ and varying final singularity length $l_1 = 5, 20, 40, 60, 80, 120$. The results are shown in figure 4.11, from which it is clear that the symmetry is not present in our system when $l_0 \neq l_1$. Instead of identical slopes at the two boundaries, we see that the slope at the initial boundary hardly changes when changing l_1. This probably means that the information about the geometry at $t = T$ is not propagated all the way to small t, in the sense that spatial geometries at small time t are oblivious to the final boundary conditions. In classical gravity, however, the geometry is sensitive to the boundary conditions no matter how far one is from the boundary.

The discrepancy between the data and the classical solutions (4.21) can mean several things: either the classical limit of CDT, at least for certain boundary conditions, is genuinely different from the minisuperspace ansatz following from general relativity, or our systems are too far from classicality or too small to make a sensible comparison. At system sizes that are currently available we will probably not learn much from more detailed measurements of volume profiles, since it is hard to distinguish alternatives for

$l_1 = 5, 20, 40, 60, 80, 120$

$\langle V(t) \rangle / V_{\mathrm{av}}$
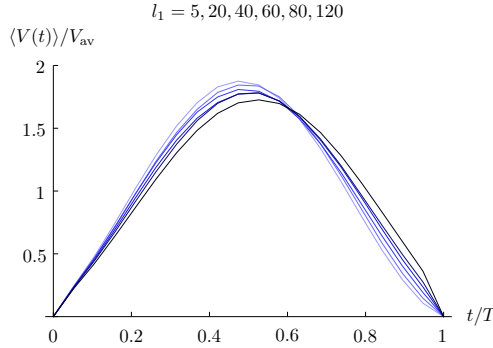
Figure 4.11: *The normalized volume profiles for $k_0 = 2.5$, $N_3 = 60\,000$, and $T = 19$. The initial singularity has fixed length $l_0 = 60$, while we varied the final singularity length $l_1 = 5, 20, 40, 60, 80, 120$ ($l_1 = 120$ corresponding to the darkest curve).*

the classical dynamics from quantum corrections. Therefore we will slightly change our strategy by assuming that effective actions exist that describe the CDT systems *at their current system sizes*. We will then attempt to deduce some of their properties directly from the data. Once we manage to significantly narrow down the relevant terms in the effective action, we will in principle be able to study the scaling properties of these terms when approaching a classical limit.

4.5   Volume correlations

Suppose that the effective action $S[V]$ for the spatial volume in CDT is local in time and can be written in terms of a Lagrangian $\mathcal{L}(V, \dot{V})$ as

$$S[V] = \int_0^T \mathrm{d}t\, \mathcal{L}(V, \dot{V}). \tag{4.22}$$

Assuming time reversal symmetry we have the condition $\mathcal{L}(V, -\dot{V}) = \mathcal{L}(V, \dot{V})$, which implies that only even powers of $\dot{V}$ can appear in the Lagrangian.

Given a proper set of boundary conditions, the action $S[V]$ will have a unique classical solution $V_0(t)$, satisfying $\delta S[V_0] = 0$, supposed to describe the expectation values $\langle V(t) \rangle$ measured in the simulations. Since in general $V_0(t)$ depends on all terms in the Lagrangian $\mathcal{L}$, it is hard to deduce specific information about the form of $\mathcal{L}$ from measurements of $\langle V(t) \rangle$ alone.
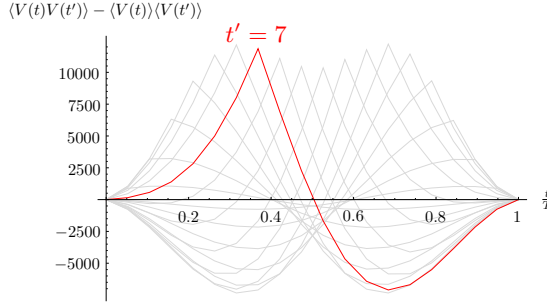
Figure 4.12: *The volume correlation function for a simulation with $T = 19$, $N_3 = 70\,000$, $l_0 = 75$, and $k_0 = 1.2$. The curves are for various fixed values of t'; the red curve corresponds to $\langle V(t)V(7)\rangle - \langle V(t)\rangle\langle V(7)\rangle$.*

It turns out that more specific information is contained in the quantum fluctuations around the classical solution. To see this, let us assume that the fluctuations are small enough for a semiclassical treatment to make sense. In that case the fluctuations $\delta V(t) = V(t) - \langle V(t)\rangle$ are correlated according to

$$\langle \delta V(t)\,\delta V(t')\rangle = \langle V(t)\,V(t')\rangle - \langle V(t)\rangle\langle V(t')\rangle \propto \left(\frac{\delta^2 S}{\delta V^2}[V_0]\right)^{-1}(t,t'). \qquad (4.23)$$

This means that we can deduce numerically the operator $P(t,t') = \frac{\delta^2 S}{\delta V^2}[V_0]$ from the spatial volume by inverting the matrix of spatial volume correlations.

In figure 4.12 the measured volume correlations are shown for a CDT simulation with $N_3 = 70\,000$, $l_0 = 75$, and $k_0 = 1.2$. Restricted to $1 \leq t, t' \leq T - 1$ the correlation matrix $\langle \delta V(t)\,\delta V(t')\rangle$ is invertible. In figure 4.13a we have plotted the diagonal and subdiagonals of its inverse $P(t,t')$. We observe that the matrix elements away from the diagonal and the first subdiagonal have all approximately the same value, which we will denote by P_0. This constant non-local contribution to the inverse correlation is due to the global constraint on the three-volume N_3 and can therefore be regarded as an artefact of the simulation set-up. If we wish to take this effect into account in the effective action (4.22), we should add a term of the form $f(\int_0^T \mathrm{d}t\, V(t))$. However, for convenience we will simply subtract this constant term from $P(t,t')$ and work with the normalized inverse correlation matrix

$$P'(t,t') = P(t,t') - P_0. \qquad (4.24)$$

65

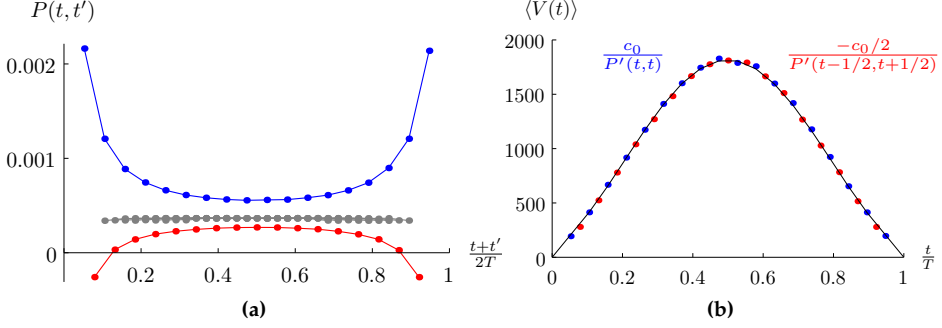**Figure 4.13:** *(a) The diagonal of $P(t,t')$ (top/blue curve), its first subdiagonal (bottom/red curve), and the remaining off-diagonal elements (grey). (b) The volume expectation value $\langle V(t) \rangle$ (solid curve) compared to the diagonals of the normalized inverse correlation function $P'(t,t') = P(t,t') - P_0$. The fitted proportionality constant is given by $c_0 \approx 0.35$.*

According to our ansatz (4.22) the operator P' is given by

$$P'(t,t') = \left[\frac{\partial^2 \mathcal{L}}{\partial V^2} - \frac{\mathrm{d}}{\mathrm{d}t} \left(\frac{\partial^2 \mathcal{L}}{\partial V \partial \dot{V}} \right) - \frac{\mathrm{d}}{\mathrm{d}t} \left(\frac{\partial^2 \mathcal{L}}{\partial \dot{V}^2} \left(\frac{\mathrm{d}}{\mathrm{d}t} \cdot \right) \right) \right] \delta(t - t'), \qquad (4.25)$$

where the partial derivatives of the Lagrangian are evaluated at $V = V_0(t)$. We see that P' consists of a purely diagonal part and a second-order time derivative. Moreover, the time-dependent coefficient of the second part only depends on the kinetic term in the Lagrangian.

In figure 4.13a, the values on the first subdiagonal of $P'(t,t')$ equal $-1/2$ times the values on the diagonal to high accuracy. We conclude that the matrix $P(t,t')$ represents a discretization of a second-order time derivative operator like the last term in (4.25). The pure diagonal component is absent or small compared to the second-order time derivative part. We can now extract the prefactor $\partial^2 \mathcal{L}/\partial \dot{V}^2[V_0]$ of the kinetic term $\dot{V}^2$ in the effective action from the data. It turns out that this prefactor is very close to $1/V_0(t) = 1/\langle V(t) \rangle$, as shown in figure 4.13b, where we have plotted the measured volume profile (solid curve) together with rescalings of the inverses of the diagonals from figure 4.13a (red and blue dots). The proportionality constant $c_0 \approx 0.35$ has been obtained by a best fit.

We conclude that the correlations are accurately described by a kinetic term in the effective action of the form

$$S[V(t)] = \int_0^T \mathrm{d}t \left(\frac{c_0}{2} \frac{\dot{V}^2}{V} + \cdots \right). \qquad (4.26)$$

This kinetic term is almost of the same form as the one appearing in the minisuperspace action (4.13) (with $N = 1$). The only difference is that there is no minus sign in front of the kinetic term in (4.26). The positive sign should come as no surprise, since the semiclassical treatment relies on the fact that the classical solution $V_0(t)$ appears at a (local) minimum of the action. The minisuperspace action, however, has its classical solution at a maximum of the action as far as the spatial volume is concerned. Of course, a maximum is easily changed into a minimum by changing the overall sign in front of the Einstein–Hilbert action.

As we will see in the next chapter, the Einstein–Hilbert and the CDT effective action can no longer be related by a simple overall sign flip when we take into account degrees of freedom beyond the spatial volume. Traceless degrees of freedom in the metric, like the moduli τ_i, appear in the Einstein–Hilbert action with a kinetic term that - unlike the spatial volume - already has the "correct", positive sign. In this case, the prescription of switching the overall sign clearly does not render the Einstein–Hilbert action positive around the classical solutions.

4.6 Conclusions

We have presented an initial investigation of the behaviour of three-dimensional CDT universes with spatial topology of a torus. Novel boundary conditions had to be introduced to obtain an interesting dynamics for the spatial volume. Our attempts to understand the spatial volume profiles by comparing them to classical general relativity have not proved very successful. However, we have uncovered a number of interesting issues along the way. These are believed to be central to CDT, but not all have surfaced explicitly in previous studies of CDT with spherical spatial topology.

First of all, the introduction of fixed boundary conditions forces us to take into account the effect of a fixed time extent in the classical theory we are comparing to. This issue did not occur explicitly in the case of spherical spatial topology with periodic boundary conditions, due to the presence of a "stalk" of minimal spatial volume (see figure 4.4). The fixed time extent T there holds for the extended universe and the stalk together, but for sufficiently large T the system can choose how much time it spends in each one of them dynamically. If one disregards the stalk, it seems as though the time extent of the extended universe is no longer fixed. To be more precise, let us consider the ensemble $\mathcal{T}_{T'}$ for $T' \leq T$ containing all CDT configurations with time extent T', initial and final boundary fixed to the minimal triangulation, and all intermediate spatial volumes non-minimal. To each configuration in $\mathcal{T}_{T'}$ we can associate a configuration in the original ensemble $\mathcal{T}$, unique up to time translation, by gluing a stalk of length $T - T'$ to it. We know that the full ensemble $\mathcal{T}$ is dominated by configurations that contain a

single extended universe. Therefore, if we neglect the microscopic contribution of the stalk to the action we can approximate the full partition by a sum over $T' \leq T$ of the partition functions corresponding to $\mathcal{T}_{T'}$. In this way the effective time extent T' has become a free parameter in the system. Still, the geometries of the extended universe, appearing in all ensembles $\mathcal{T}_{T'}$ together, form only a slightly larger subclass than in the fixed boundary case: the time extent T' is allowed to vary, but it is still required to be position-independent. As a consequence, one additional equation of motion can be satisfied in the classical limit: the homogeneous part of, say, the time-time component of the Einstein equations. This means that in the case of spherical spatial topology one does not have to worry about fixed time extents when comparing CDT to homogeneous cosmologies.

Secondly, the measurements presented in section 4.4 show beyond doubt that the boundary conditions have an effect on the spatial volume profile. This means that the spatial volume is not completely decoupled from the other degrees of freedom in the spatial geometry. Although this is what we expect from a potential theory of gravity, this coupling makes it harder to assess the size of quantum contributions to the volume profiles. As we know from previous research and have confirmed in section 4.5, quantum fluctuations of the spatial volume itself are fairly well understood. On the other hand, we do not know how big the quantum fluctuations in the moduli trajectories are, although we will gather some clues in chapter 5. Any major deviation from the classical trajectories will have an effect on the volume profile. This might explain the observations we made in section 4.4 concerning systems with asymmetric boundary conditions.

Finally, a semiclassical comparison of the correlations in the quantum fluctuations to an effective action requires a (local) minimum around the classical solution. The Euclidean Einstein–Hilbert action, however, does not have this property, a fact which is known as the *conformal mode problem* [39, 84] and which we discuss in more detail in the next chapter. In the case of CDT in 3+1 dimensions with spherical topology (see [10]) it was already observed that the minisuperspace action, derived from the Einstein–Hilbert action, for the spatial volume alone can be rendered positive by flipping its overall sign. In our case it becomes immediately clear that such a procedure on the minisuperspace action, including the moduli, does not render it positive.

This last issue leads us directly to the main question of the next chapter: how does CDT render the kinetic term in the effective action positive definite? In view of the results we will present there we have added a discussion in appendix C showing that any classical solution to the original unbounded minisuperspace action (4.13) can also be obtained from a bounded action with a suitable potential.

Moduli measurements in CDT

The model of Causal Dynamical Triangulations (CDT) on the torus provides an explicit example of a space-time path integral with a non-trivial time evolution of the two-dimensional conformal geometry, i.e. of the shape[17] of the spatial tori. In chapter 4 we attempted to understand this shape evolution by considering its effect on the dynamics of the spatial volume. Although we found qualitative similarities between measured spatial volume profiles and solutions of a classical minisuperspace action, a quantitative description is still lacking. By examining the volume correlations we did manage to establish the effective kinetic term for the spatial volume. We will take this result as a firm starting point and try to fill in some of the dots in the full effective action governing CDT on the torus,

$$S_{\text{eff}}[g_{ab}(t)] = \int_0^T dt \left(\frac{c_0}{2} \frac{\dot{V}^2}{V} + \cdots \right).\tag{5.1}$$

To do this we introduce a new observable into our simulations, the moduli $\tau_i(t)$ governing the conformal shape of the spatial geometries. We have already seen the moduli in action in the model of dynamical triangulations in two dimensions in chapter 3. There we found good agreement of the measured moduli distributions in an ensemble of random triangulations and predictions from a continuum description in terms of Liouville theory. This result was non-trivial in that the discrete moduli were defined in terms of discrete differential geometry, whose applicability in random geometries is not obvious. The relation between continuum and discrete differential geometry is

---

A brief summary of the results in this chapter has appeared in [32].

[17]To prevent confusion, in this chapter and the rest of this thesis we will *not* use the word "shape" in the sense of "shape of the volume profile" used in chapter 4. Unless explicitly indicated otherwise, by "shape" we mean the conformal shape of the torus parametrized by the moduli.

rather well understood in low-curvature regimes, while dynamical triangulations display large curvatures on short scales.

There is some evidence that the spatial triangulations in CDT are slightly better behaved than the geometries of the same dimension appearing in the DT, at least not worse.[18] Therefore, if the spatial geometry in CDT has an effective description in some large-distance limit in terms of a continuum metric on the torus, we are confident that our discrete moduli measurements will be related to the moduli of that metric. This means that we can add the moduli to the list of observables that we can use as probes for the effective dynamics of CDT. As far as we know, this chapter contains the first non-trivial results in CDT concerning the dynamics of the traceless degrees of freedom of the spatial geometry.[19]

We will extend the method from section 4.5 to study the effective kinetic term of the spatial volume and the moduli combined. In order to do this we first construct a continuum ansatz for the effective kinetic term of the full spatial metric. As mentioned before, we cannot simply take the Euclidean Einstein–Hilbert action in ADM form, because it suffers from the conformal mode problem and does not have a minimum at its classical solution. There are not that many alternatives when we insist on full diffeomorphism invariance. However, if we merely insist on actions that are invariant under foliation-preserving diffeomorphisms, there are natural candidates for effective actions. We will argue that the preferred time-foliation in CDT actually points in the direction of this reduced diffeomorphism symmetry.

This chapter will be structured as follows. In section 5.1 we will show how to generalize the procedure of assigning moduli to a two-dimensional triangulation to CDT configurations, in order to obtain a well-defined trajectory in moduli space. After that we will have a brief look at the average trajectories and compare these to the classical solutions we found in chapter 4. In section 5.3 we will consider the moduli correlations and describe what they mean in terms of the effective action.

5.1 Moduli as observables in CDT

Let us summarize the algorithm described in 3.2 of assigning a point in moduli space to a two-dimensional triangulation $\mathbf{T}_0$ of the torus. The construction relies on the notion of discrete differential forms in a simplicial manifold. Recall that a discrete p-form is defined as a function that assigns a real number to each oriented p-simplex. In particular,

---

[18]See [13] for some partial results on spatial Hausdorff dimension in 2+1 dimensions and [11] for more detailed results in 3+1 dimensions.

[19]See [47] for an analytic investigation of similar degrees of freedom in CDT in a reduced setting.

a discrete 1-form α assigns a number to a directed edge e and this number should be interpreted as the integral along that edge. As a consequence, we have a natural notion of discrete integration of a 1-form α along a discrete curve γ given by a sequence of directed edges,

$$\int_\gamma \alpha = \sum_{e \in \gamma} \alpha(e). \tag{5.2}$$

To find the moduli we first need a pair of closed discrete curves γ_i that generates the fundamental group of the topological manifold defined by the triangulation $\mathbf{T}_0$. Such a pair can be constructed using the algorithm described in section 2.4. Next we determine a basis α^i of the two-dimensional space of harmonic 1-forms, i.e. discrete 1-forms that satisfy $d\alpha^i = 0$ and $\delta\alpha^i = 0$ in terms of the discrete exterior derivative d and its adjoint δ in (3.28). This basis is uniquely determined if we require it to be dual to the generators γ_i in the sense that

$$\int_{\gamma_j} \alpha^i = \sum_{e \in \gamma_j} \alpha^i(e) = \delta^i_j. \tag{5.3}$$

In terms of these harmonic forms the modular parameter τ can be defined as

$$\tau = -\frac{\langle \alpha^1, \alpha^2 \rangle}{\langle \alpha^2, \alpha^2 \rangle} + i \sqrt{\frac{\langle \alpha^1, \alpha^1 \rangle}{\langle \alpha^2, \alpha^2 \rangle} - \left(\frac{\langle \alpha^1, \alpha^2 \rangle}{\langle \alpha^2, \alpha^2 \rangle} \right)^2}, \tag{5.4}$$

where the inner product $\langle \alpha^i, \alpha^j \rangle$ is defined simply as

$$\langle \alpha^i, \alpha^j \rangle = \sum_e \alpha^i(e) \alpha^j(e). \tag{5.5}$$

The value we obtain for τ depends on the choice of the curves γ_i. This has to do with the fact that τ parametrizes the Teichmüller space of the torus, i.e. the space of conformal structures on a torus with a marked pair of curves. A different choice of curves will lead to a value of τ related to the original by the action of the modular group (3.9),

$$\tau \to \frac{a\tau + b}{c\tau + d}, \quad \begin{pmatrix} a & b \\ c & d \end{pmatrix} \in SL(2, \mathbb{Z})/\mathbb{Z}_2. \tag{5.6}$$

Therefore the moduli space of metrics modulo conformal transformations and diffeomorphisms corresponds to the space of orbits of the modular group in the Teichmüller space. This ambiguity was resolved in chapter 3 by restricting τ to a fundamental domain $\mathcal{M}$ of the modular group in the complex upper half-plane.

The method outlined above can be applied directly to the spatial triangulation $\mathbf{T}_t$ appearing in a CDT configuration at time t. However, in general there is no need to
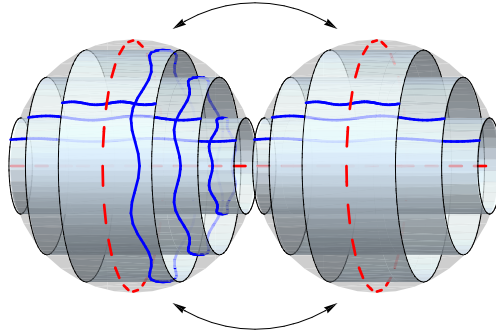
Figure 5.1: *Projection of the upper and lower hemisphere of the 3-sphere onto two 3-balls whose boundary 2-spheres are identified. The dashed red curves correspond to the initial and final singularity while the blue curves denote sets of canonical generators of the fundamental group of the Hopf tori.*

map the moduli to the fundamental domain $\mathcal{M}$ since there might be a canonical set of generating curves arising from the boundary conditions at $t = 0$ and $t = T$. This happens for the system with degenerate boundary conditions described in section 4.2. In such a case a CDT configuration defines an unambiguous sequence in Teichmüller space given by the values $\tau(t)$ for $t = 0, \ldots, T$.

Let us see how we can determine this canonical pair of generating curves. Recall that the foliated geometries appearing in the CDT ensemble are topologically of the form of a Hopf foliation of the 3-sphere as in figure 5.1. The initial and final singularity together describe a Hopf link, i.e. two circles linked together exactly once, embedded in the 3-sphere. To any closed curve γ in the complement of the Hopf link in the 3-sphere one can assign a pair of linking numbers L_0 and L_1 describing how often γ links the initial and final singularity respectively. It is not hard to see that on each spatial torus a pair (L_0, L_1) of integers determines a homotopy class of closed curves. Therefore we find a canonical pair of generators on a spatial torus by selecting a closed curve γ_1 with linking numbers $(0, 1)$ and γ_2 with linking numbers $(1, 0)$. Examples of these curves are shown in figure 5.1. The curve γ_2 can be chosen to contract to zero length when approaching the initial singularity, and the same holds for γ_1 when approaching the final singularity. We can therefore naturally assign to the singularities the values $\tau(0) = 0$ and $\tau(T) = i\infty$ lying on the boundary of Teichmüller space.

In practice, we do not determine first all canonical pairs of curves on the spatial triangulations, since a direct calculation of the linking numbers in the three-dimensional geometry is non-trivial. Instead, for each spatial triangulation $\mathbf{T}_t$ we generate an arbitrary
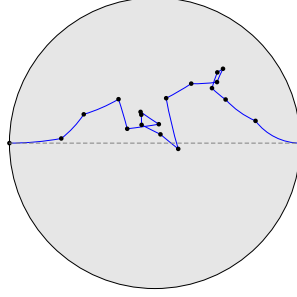
Figure 5.2: *Sequence of moduli in the Poincaré disk. The points at $\tilde{\tau} = -1$ and $\tilde{\tau} = 1$ correspond to the degenerate geometries at the initial and final singularity respectively.*

pair of generating curves $\gamma_1'(t)$ and $\gamma_2'(t)$ using the same methods as in chapter 3. We use these to determine an initial sequence of moduli $\tau'(t)$. We then compare for each time $t = 2, \ldots, T - 1$ the generators $\gamma_i'(t)$ with those at time $t - 1$ and determine the modular transformation $m_t \in SL(2, \mathbb{Z})$ relating the two. Moreover, we can easily determine the linking number L_1 of the curves $\gamma_i'(1)$ at time $t = 1$ and the linking number L_0 of the curves $\gamma_i'(T - 1)$ at time $t = T - 1$. These linking numbers together with the matrices m_t provide enough information to construct for each time t the modular transformation that relates the $\gamma_i'(t)$ to the desired $\gamma_i(t)$, and therefore $\tau'(t)$ to $\tau(t)$.

The representation of the moduli evolution $\tau(t)$ in the upper half-plane is perhaps not the most convenient one. Instead, let us map the upper half-plane to the Poincaré disk by the fractional linear transformation

$$\tilde{\tau} = \frac{\tau - i}{\tau + i}.$$ (5.7)

The degenerate tori are now located on the boundary of the disk corresponding to $|\tilde{\tau}| = 1$. The initial and final singularity get mapped to $\tilde{\tau}(0) = -1$ and $\tilde{\tau}(T) = 1$. In figure 5.2 an example is shown of a trajectory in the Poincaré disk corresponding to a CDT configuration taken from one of our simulations. Apart from the compactness this representation has the advantage that the discrete symmetries of the CDT system are easily represented: parity symmetry corresponds to mirroring in the real axis, while time reversal symmetry corresponds to mirroring in the imaginary axis. The latter is of course only a real symmetry when the boundary lengths l_0 and l_1 are equal.

In section 3.2 we noticed that as a by-product of the construction of the moduli for a two-dimensional triangulation we obtain an explicit embedding into a parallelogram in the Euclidean plane. In figure 5.3 we show an example of such an embedding for a
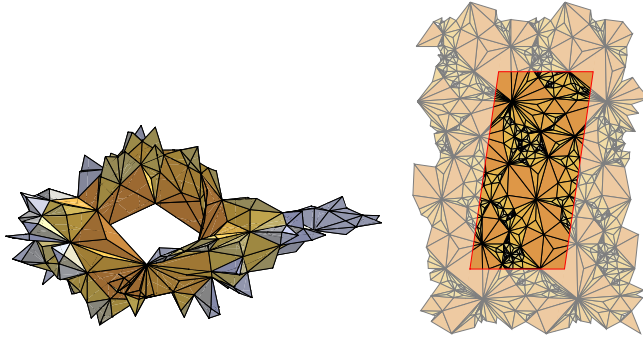
Figure 5.3: *A triangulated torus taken from a CDT simulation and a corresponding periodic embedding in the plane. This triangulation consists of 470 triangles and $\tau \approx 0.30 + 2.09i$. The triangles are colored according to their conformal factor, i.e. their area in the embedding.*

spatial triangulation close to the final singularity from an actual CDT simulation. We have coloured the triangles according to their area in the embedding. As we will see in section 5.3 the distribution of these areas is of importance when studying the dynamics of the moduli.

5.2 Classical solutions

Let us start, as in chapter 4 for the spatial volume, by comparing the average trajectories of the moduli to classical solutions of the Euclidean Einstein–Hilbert action. We saw in section 4.3 that our boundary conditions are homogeneous in space, which implies that the relevant classical solutions will have the same property. Moreover, we argued that we should restrict the Einstein–Hilbert action to geometries with a fixed distance T between the boundaries. These considerations allowed us to restrict our attention to space-time geometries of the form

$$ds^2 = dt^2 + V(t)\hat{g}_{ab}(\tau(t))dx^a dx^b, \tag{5.8}$$

where $\hat{g}_{ab}(\tau)$ is the flat background metric (4.12) determined by the moduli. The mini-superspace action is obtained by evaluating the Euclidean Einstein–Hilbert action on the metric (5.8), giving

$$S[V, \tau] = \kappa \int dt \left(-\frac{1}{2}\frac{\dot{V}^2}{V} + \frac{V}{2}\frac{\dot{\tau}_1^2 + \dot{\tau}_2^2}{\tau_2^2} + 2\Lambda V \right). \tag{5.9}$$

We already determined the spatial volumes of the classical solutions to be

$$V(t) = \begin{cases} l_0 l_1 \frac{\sinh\left(\sqrt{-\Lambda}(T-t)\right)\sinh\left(\sqrt{-\Lambda}\,t\right)}{\sinh^2\left(\sqrt{-\Lambda}\,T\right)} & \text{if } \Lambda < 0 \\ l_0 l_1 (T-t)t/T^2 & \text{if } \Lambda = 0 \\ l_0 l_1 \frac{\sin\left(\sqrt{\Lambda}(T-t)\right)\sin\left(\sqrt{\Lambda}\,t\right)}{\sin^2\left(\sqrt{\Lambda}\,T\right)} & \text{if } 0 < \Lambda < \left(\frac{\pi}{T}\right)^2. \end{cases} \tag{5.10}$$

The moduli trajectories can now be found easily by integrating the constant of motion $p = V\sqrt{\dot{\tilde{\tau}}_1^2 + \dot{\tilde{\tau}}_2^2}/\tau_2$,

$$\tau(t) = \begin{cases} i\frac{l_1}{l_0} \frac{\sinh\left(\sqrt{-\Lambda}\,t\right)}{\sinh\left(\sqrt{-\Lambda}(T-t)\right)} & \text{if } \Lambda < 0 \\ i\frac{l_1}{l_0} \frac{t}{T-t} & \text{if } \Lambda = 0 \\ i\frac{l_1}{l_0} \frac{\sin\left(\sqrt{-\Lambda}\,t\right)}{\sin\left(\sqrt{-\Lambda}(T-t)\right)} & \text{if } 0 < \Lambda < \left(\frac{\pi}{T}\right)^2. \end{cases} \tag{5.11}$$

In terms of the Poincaré disk coordinates $\tilde{\tau} = \tilde{\tau}_1 + i\tilde{\tau}_2$, these solutions parametrize the real axis $\tilde{\tau}_2 = 0$. In general the trajectories $\tilde{\tau}_1(t)$ depend on the dimensionless parameters l_1/l_0 and $v = V/(l_0 l_1 T)$. In figure 5.4a we have plotted the classical trajectories in the symmetric case $l_1/l_0 = 1$ for values v ranging from 0 to ∞. For $v = 1/6$ we find simply $\tilde{\tau}_2(t) = -1/2 + t/T$.

In chapter 4 we already reported on the measurement of the volume expectation value $\langle V(t) \rangle$ for CDT simulations with $k_0 = 2.5$ and $N_3 = 60\,000$ and boundary lengths $l_0 = l_1$ varying between 5 and 180 (see figure 4.10b). In figure 5.4b the corresponding average trajectories $\langle \tilde{\tau}_1(t) \rangle$ of the real part of the moduli in the Poincaré disk are shown. As for the spatial volumes, we observe that the measured trajectories are qualitatively represented by classical trajectories with certain values of v. However, when we compare the fitted values of v to those that we obtain from fitting the volume expectation values to the classical volume profiles, we find that they are systematically larger. This means that the moduli are attracted to the centre of the Poincaré disk more than expected from the classical solutions.

Some comments on our results are in order. First of all the distributions of the moduli in the Poincaré disk for a fixed time t are not sharply peaked around their average. This is illustrated in figure 5.5, which shows a sequence of density plots for $t = 1$ up to $t = 18$. We can conclude from this that as far as the moduli are concerned our system is situated quite far into the quantum regime. As a consequence we expect the back-reaction of the various degrees of freedom, including the conformal ones, on the volume and moduli evolution to be substantial. Secondly, it is hard to gather a lot of statistics in our simulations, since the autocorrelation time of the moduli within a Monte Carlo simulation is very high, much higher than the autocorrelation time of the spatial
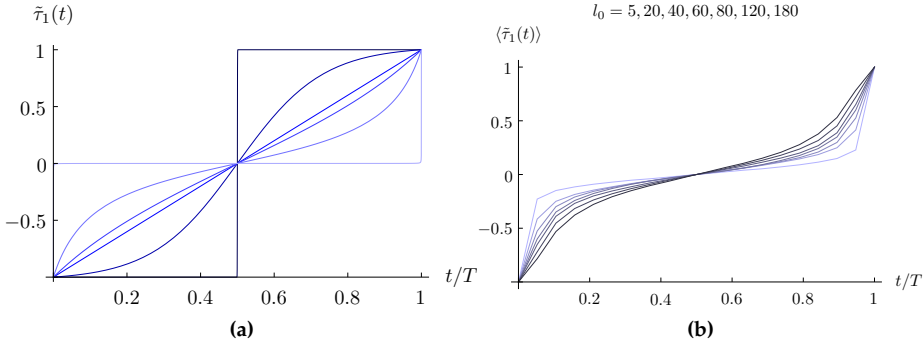
Figure 5.4: *(a) The classical trajectories $\tilde{\tau}_1$ for different values of $v = V_3/(l_0 l_1 T)$. The curves, from dark to light, correspond to $v = 0, 0.01, 1/6, 1/\pi, 2, \infty$ (as in figure 4.8). (b) Expectation values $\langle \tilde{\tau}_1(t) \rangle$ for simulations with $V_3 = 60\,000$, $k_0 = 2.5$ and boundary lengths running between 5 (lightest curve) and 180 (darkest curve).*
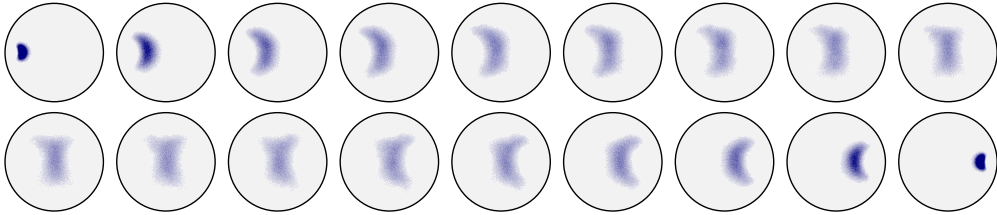
Figure 5.5: *Density plots of the measured moduli $\tilde{\tau}(t)$ in the Poincaré disk for each time $t = 1, \ldots, 18$ from a simulation with $V_3 = 60\,000$, $k_0 = 2.5$ and $l_0 = l_1 = 80$, based on $140\,000$ measurements.*

volumes. This means that one has to perform a very large number of moves to make sure that two consecutive measurements are uncorrelated. Even then one cannot be completely sure that one is not stuck in a local minimum of the free energy. This will probably get worse with increasing system size.

On the other hand we already noticed in the last chapter that (5.9) is not viable as an effective action to start with, since it cannot describe the quantum fluctuations around a classical solution. Therefore in the next section we will reconsider our ansatz and perform measurements that provide information concerning the effective kinetic term.

5.3 The effective kinetic term

Let us first describe briefly what we mean by an effective action for CDT in the current context. Remember that one of our goals is to establish what kind of effective geometric theory might emerge from CDT in a large-distance limit. By emergence of a geometric theory we will mean that there exists an effective action in terms of a space-time metric that agrees in a semi-classical approximation with measurements of large-scale observables in CDT. The classical solution to the effective action should determine expectation values, while the quadratic expansion around its minimum should agree with correlations of the first-order fluctuations.

There are two kinds of obstructions preventing the Euclidean Einstein–Hilbert action in its usual form to arise as an effective action for CDT in the sense defined above. The first obstruction has to do with the fixed time extent T between the boundaries, which we already discussed in chapter 4. The consequence of this constraint is that one should be able to gauge-fix the space-time metric in the effective action to proper time form without changing its equations of motion. In the case of the Euclidean Einstein–Hilbert action this means that we should consider the ADM action with the lapse N set equal to one,

$$\begin{aligned} S[g_{ab}, N^a] &= S_{ADM}[g_{ab}, N^a, N = 1] \\ &= \kappa \int_0^T \mathrm{d}t \int \mathrm{d}^2 x \sqrt{g} \left(K_{ab} \mathcal{G}^{abcd} K_{cd} - R + 2\Lambda \right), \end{aligned} \tag{5.12}$$

where

$$\mathcal{G}^{abcd} = \frac{1}{2}(g^{ac}g^{bd} - g^{ad}g^{bc}) - g^{ab}g^{cd} \tag{5.13}$$

is the Wheeler–DeWitt metric on the space of two-dimensional metrics.

Due to the global time t the new action (5.12) has a somewhat simpler interpretation than the full ADM action. It is formally of the form of a point particle moving through the infinite-dimensional superspace $\mathcal{M}$ of two-dimensional geometries with metric given by the Wheeler–DeWitt metric $\mathcal{G}$ and subjected to a potential

$$U[g] = \int \mathrm{d}^2 x \sqrt{g}(R - 2\Lambda). \tag{5.14}$$

In this picture the second obstruction becomes clear once we notice that the Wheeler–DeWitt metric is not an (infinite-dimensional) Riemannian metric but a pseudo-Riemannian metric. As a consequence the classical solutions are not local minima of the action (5.12), but saddle points. The Wheeler–DeWitt metric $\mathcal{G}$ is negative definite on the conformal directions in superspace, meaning that we can lower the value of the

action by adding to a classical solution a perturbation given by a fluctuating conformal factor. This fact is known as the *conformal mode problem* and has caused a lot of headaches for researchers investigating Euclidean approaches to quantum gravity (see for example [39, 55, 84]). In our case we want to derive from the effective action a prediction for the correlations in the fluctuations around classical solutions. To do this we really need the action expanded to second order in the fluctuations to be positive definite, which is not the case for (5.12).

We therefore need a different ansatz for an effective action. It is clear what would fix the problem: a positive definite metric on $\mathcal{M}$. Fortunately $\mathcal{G}$ is not the only ultra-local diffeomorphism-invariant metric on $\mathcal{M}$, there is a whole family parametrized by λ,

$$\mathcal{G}_\lambda^{abcd} = \frac{1}{2}(g^{ac}g^{bd} - g^{ad}g^{bc}) - \lambda\, g^{ab}g^{cd}. \tag{5.15}$$

This metric, which we will refer to as the *generalized Wheeler–DeWitt metric*, is positive definite in the regime $\lambda < 1/2$. Using $\mathcal{G}_\lambda$ instead of $\mathcal{G}$ in the gravitational action, values of λ different from 1 explicitly break general covariance, which at first seems an unphysical generalization. However, a careful look at the CDT ensemble shows that general covariance might not be manifest: the foliation requirement on the three-dimensional triangulations seems to introduce a preferred time slicing at the microscopic level. Whether this preferred time slicing survives in a continuum limit remains to be seen, but at present we cannot ignore it. Therefore, we have no reason not to consider actions that explicitly depend on the chosen time slicing.

Replacing $\mathcal{G}$ by $\mathcal{G}_\lambda$ in (5.12) we arrive at our final ansatz

$$S_{\text{eff}}[g_{ab}, N^a] = \kappa \int_0^T \mathrm{d}t \int \mathrm{d}^2x \sqrt{g} \left(K_{ab}\mathcal{G}_\lambda^{abcd} K_{cd} - U[g] \right), \tag{5.16}$$

where the potential $U[g]$ for the spatial metric g is allowed to have higher-power curvature terms.

Actions of similar form with Lorentzian signature have been introduced by Hořava [66, 67] as possible renormalizable extensions of general relativity. Possible connections between such anisotropic models and CDT have been previously put forward both in the context of the spectral dimension of space-time [68] and the phase diagram [9]. If (5.16) survives the non-trivial test that we are about to present, we can view our results as evidence strengthening these connections.

We will start by comparing the correlation functions of the volume $V(t)$ and the moduli $\tau_i(t)$ semi-classically to the minisuperspace action we get from (5.16) using the
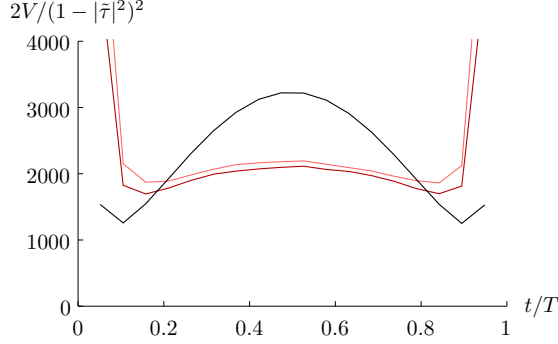
Figure 5.6: $V/(1-|\tilde{\tau}|^2)^2$ *as a function of time (black), together with the (rescaled) diagonals* $P_{11}(t,t)$ *(orange) and* $P_{22}(t,t)$ *(red). From a CDT simulation with* $V_3 = 60\,000$, $k_0 = 2.5$ *and* $l_0 = l_1 = 80$.

homogeneous ansatz (5.8),[20]

$$S[V,\tau] = \kappa \int dt \left((1/2 - \lambda)\frac{\dot{V}^2}{V} + \frac{V}{2}\frac{\dot{\tau}_1^2 + \dot{\tau}_2^2}{\tau_2^2} + 2\Lambda V \right) \tag{5.17}$$

$$= \kappa \int dt \left((1/2 - \lambda)\frac{\dot{V}^2}{V} + 2V\frac{\dot{\tilde{\tau}}_1^2 + \dot{\tilde{\tau}}_2^2}{(1 - |\tilde{\tau}|^2)^2} + 2\Lambda V \right). \tag{5.18}$$

To do this we generalize the method from section 4.5 to include the fluctuations of the moduli, i.e. we measure the correlation matrix

$$\langle \delta f^i(t)\delta f^j(t') \rangle = \langle f^i(t)f^j(t') \rangle - \langle f^i(t) \rangle\langle f^j(t') \rangle, \tag{5.19}$$

with $f^0 = V$, $f^1 = \tilde{\tau}_1$ and $f^2 = \tilde{\tau}_2$. This is a $3(T-1) \times 3(T-1)$ matrix whose inverse should be related to the second-order derivative

$$P_{ij}(t,t') = \frac{\delta^2 S_{eff}}{\delta f^i(t)\delta f^j(t)} \tag{5.20}$$

of the effective action evaluated at its classical solution.

We observe in the data that to high accuracy $P_{ij}(t,t')$ vanishes for $i \neq j$ and the $P_{ii}(t,t')$ have the structure of a second-order time derivative, i.e. the first subdiagonal has values approximately $-1/2$ times those on the diagonal. According to our ansatz

---

[20]The function $|d\tau|^2/\tau_2^2$ is the Poincaré metric in the upper half-plane, while $4|d\tilde{\tau}|^2/(1 - |\tilde{\tau}|^2)^2$ is its counterpart in the Poincaré disk.

(5.18) the diagonals $P_{11}(t,t)$ and $P_{22}(t,t)$ should be proportional to $2V/(1-|\tilde{\tau}|^2)^2$. However, this turns out not to be satisfied by the data, as is apparent from figure 5.6. This means that the minisuperspace action (5.18) does not properly describe the fluctuations in the moduli.

Does this mean that our ansatz (5.16) is wrong? This is not necessarily the case, since in the analysis above we put in the non-trivial assumption that the "average" geometry is homogeneous. If we evaluate the action (5.16) to second order around a non-homogeneous background metric, we might obtain a different kinetic term. Below we will derive the form of the kinetic term for the spatial volume and the moduli in terms of a general background geometry $g_{ab}(t)$. To be precise, we will determine the functional $G_{ij}[g]$ such that the action (5.16) can be written as

$$S_{eff}[g_{ab}] = \kappa \int_0^T dt \left(\frac{1}{4} \dot{f}^i G_{ij}[g_{ab}(t)] \dot{f}^j + \cdots \right) \tag{5.21}$$

with the velocities $\dot{f}^i$ not appearing elsewhere. We can then compare the correlations (5.19) to the expectation values $\langle G_{ij}[g_{ab}(t)] \rangle$ in the CDT simulations. This analysis does not require the geometries to be close to a single background geometry, as long as $G_{ij}[g_{ab}(t)]$ is peaked around its average $\langle G_{ij}[g_{ab}(t)] \rangle$.

The matrix $G_{ij}[g]$ in (5.21) corresponds to a restriction of the generalized Wheeler–DeWitt metric (5.15) on the tangent space to the space of metrics at the metric g_{ab}. It is the induced metric on the subspace spanned by the gradients of f^i, i.e. of V, τ_1, and τ_2. To find this induced metric, notice that its inverse $G^{ij}[g]$ is given by the inner products of the gradients of f^i, namely,

$$G^{ij}[g] = \int d^2x \frac{1}{\sqrt{g}} \frac{\delta f^i}{\delta g_{ab}(x)} \mathcal{G}^\lambda_{abcd} \frac{\delta f^j}{\delta g_{cd}(x)}, \tag{5.22}$$

where $\mathcal{G}^\lambda_{abcd}$ is the inverse Wheeler–DeWitt metric

$$\mathcal{G}^\lambda_{abcd} = \frac{1}{2}(g_{ac}g_{bd} + g_{ad}g_{bc}) - \mu\, g_{ab}g_{cd} \quad \text{with } \mu = \frac{\lambda}{2\lambda - 1}. \tag{5.23}$$

The volume-volume part G^{00} is easily evaluated, giving

$$G^{00}[g] = \int d^2x \frac{1}{\sqrt{g}} \frac{\delta V}{\delta g_{ab}} \mathcal{G}^\lambda_{abcd} \frac{\delta V}{\delta g_{cd}} = \frac{1}{4} \frac{V}{\frac{1}{2} - \lambda}, \tag{5.24}$$

which does not depend on the curvature. The gradient of the volume generates a global conformal transformation leaving the moduli invariant and therefore the off-diagonal entries $G^{01}[g]$ and $G^{02}[g]$ vanish.

Some more work is required to calculate the moduli-moduli part. First we have to investigate how the moduli parameter changes under a metric perturbation δg_{ab}. Recall from section 3.2 that we can express τ in terms of inner products $\langle \alpha^i, \alpha^j \rangle$ of harmonic forms. From the fact that under a metric perturbation the harmonic form α^i remains in the same cohomology class it follows that[21] $\delta \alpha^i$ is an exact differential form and therefore its inner product with α^j vanishes. Hence, when perturbing the inner product $\langle \alpha^i, \alpha^j \rangle$ we can regard the α^i to be invariant,

$$\delta \langle \alpha^i, \alpha^j \rangle = \delta \int \mathrm{d}^2 x \sqrt{g} \alpha_a^i g^{ab} \alpha_b^j = \int \mathrm{d}^2 x \sqrt{g} \left(\frac{1}{2} g^{ab} g^{cd} - g^{ac} g^{bd} \right) \alpha_a^i \alpha_b^j \delta g_{cd}. \tag{5.25}$$

It follows from (5.4) that

$$\frac{\delta \tau}{\delta g_{ab}(x)} = -\tau_2 \frac{\delta \langle \alpha^1, \alpha^2 \rangle}{\delta g_{ab}(x)} - \tau_2 \tau \frac{\delta \langle \alpha^2, \alpha^2 \rangle}{\delta g_{ab}(x)} \tag{5.26}$$

$$= -\frac{\tau_2}{2} \sqrt{g} \left(\alpha_1 \cdot \alpha_2 \, g^{ab} - \alpha_1^a \alpha_2^b - \alpha_1^b \alpha_2^a + \tau \left(\alpha_2 \cdot \alpha_2 \, g^{ab} - 2\alpha_2^a \alpha_2^b \right) \right). \tag{5.27}$$

To evaluate this expression let us gauge-fix the spatial coordinates to conformal gauge, as we did in section 3.2, in which the background metric takes the form

$$g_{ab}(x) = e^{2\phi(x)} \hat{g}_{ab}(\tau). \tag{5.28}$$

In these coordinates the harmonic forms are given simply by $\alpha^i = dx^i$. Plugging these into (5.27) we find

$$G^{ij}[g] = \int \mathrm{d}^2 x \frac{1}{\sqrt{g}} \frac{\delta \tau_i}{\delta g_{ab}} \mathcal{G}_{abcd}^\lambda \frac{\delta \tau_j}{\delta g_{cd}} = \frac{1}{2} \delta_{ij} \tau_2^2 \int \mathrm{d}^2 x \, e^{-2\phi} \equiv \frac{1}{2} \delta_{ij} \tau_2^2 A[g]. \tag{5.29}$$

In the case that g_{ab} is flat, ϕ is spatially constant and equal to $1/2 \log(V)$, hence $A[g] = 1/V$ in the homogeneous case as expected from (5.18). However, when inhomogeneities are present $A[g]$ is strictly larger than $1/V$.

We can express $A[g]$ in a coordinate-independent way by noticing that ϕ is related to the spatial curvature by $R = 2\Delta \phi$ where $\Delta = -1/\sqrt{g} \partial_a (\sqrt{g} g^{ab} \partial_b \cdot)$ is the (positive) Laplacian associated with g. It follows that $\phi = \phi_0 + \Delta^{-1} R/2$ for some constant ϕ_0 and Δ^{-1} is the inverse Laplacian with the singular constant mode projected out. The value for ϕ_0 follows from evaluating

$$1 = \int \mathrm{d}^2 x \sqrt{g} \, e^{-2\phi} = e^{-2\phi_0} \int \mathrm{d}^2 x \sqrt{g} \exp(-\Delta^{-1} R), \tag{5.30}$$

hence

$$A[g] = \int \mathrm{d}^2 x \sqrt{g} \, e^{-4\phi} = \frac{\int \mathrm{d}^2 x \sqrt{g} \exp(-2\Delta^{-1} R)}{\left(\int \mathrm{d}^2 x \sqrt{g} \exp(-\Delta^{-1} R) \right)^2}. \tag{5.31}$$

---

[21]Warning: in this paragraph δ will refer to the variation, not the dual of the exterior derivative.

We conclude that for arbitrary background metric g_{ab} the relevant part of the kinetic term is given by

$$S_{eff}[g_{ab}] = \kappa \int_0^T \mathrm{d}t \left((\frac{1}{2} - \lambda)\frac{\dot{V}^2}{V} + \frac{1}{2A[g]} \frac{\dot{\tau}_1^2 + \dot{\tau}_2^2}{\tau_2^2} + \cdots \right).$$ (5.32)

To test this general ansatz we have to find a suitable discretization $A[\mathbf{T}_0]$ of the curvature functional $A[g]$ applicable to equilateral triangulations $\mathbf{T}_0$. There are basically two approaches to obtain such a discretization. The first approach, which is the simplest and the one that we pursue here, is to discretize $A[g]$ using the expression in terms of the conformal factor ϕ. The discrete harmonic embedding of a triangulation $\mathbf{T}_0$ into a parallelogram in the Euclidean plane, which we discussed in section 3.2 and 5.1, can be interpreted as a discrete version of the conformal gauge fixing (5.28). Since the triangles all have equal volume with respect to the spatial metric g_{ab}, we can naturally assign a conformal factor ϕ to a triangle $\mathbf{t}$ according to its volume with respect to $\hat{g}_{ab}$. In this way we obtain the natural discretization

$$A[\mathbf{T}_0] = \frac{\sum_{\mathbf{t}} a(\mathbf{t})^2}{\left(\sum_{\mathbf{t}} a(\mathbf{t})\right)^2},$$ (5.33)

where the sum is over all triangles $\mathbf{t}$ and $a(\mathbf{t})$ is the area of $\mathbf{t}$ in the harmonic embedding. For a triangulation with N triangles we have $A[\mathbf{T}_0] \geq 1/N$ with equality only attained by regular triangulations. For example, the triangulation in figure 5.3 corresponds to a value of $A[\mathbf{T}_0] \approx 1/96 \approx 4.9/470$ which is 4.9 times as high as for a regular triangulation of 470 triangles.

The second approach is to mimic the derivation of $A[g]$ in the discrete setting. Notice that $A[g]$ quantifies how severely the moduli are affected by a random metric deformation. More precisely, $A[g]$ equals the expected squared distance of the displacement in moduli space caused by a random metric deformation normalized according to the Wheeler–DeWitt metric. Analogously, we can associate a number $A'[\mathbf{T}_0]$ to a triangulation $\mathbf{T}_0$ recording how much the discrete moduli are affected by a random local update of the triangulation. In appendix D we show that this definition leads to an expression similar to (5.33) but includes a term that takes into account the shape of the triangles in the embedding. Numerical investigations have shown that both definitions, $A[\mathbf{T}_0]$ and $A'[\mathbf{T}_0]$, are roughly proportional, but disagree on the precise overall factor. This is not a big problem here, since a change in the overall factor only renormalizes the couplings κ and $1/2 - \lambda$.

Taking into account these considerations, let us revisit the data from our Monte Carlo simulations. We should not compare the diagonals $P_{11}(t,t)$ and $P_{22}(t,t)$ of the inverse
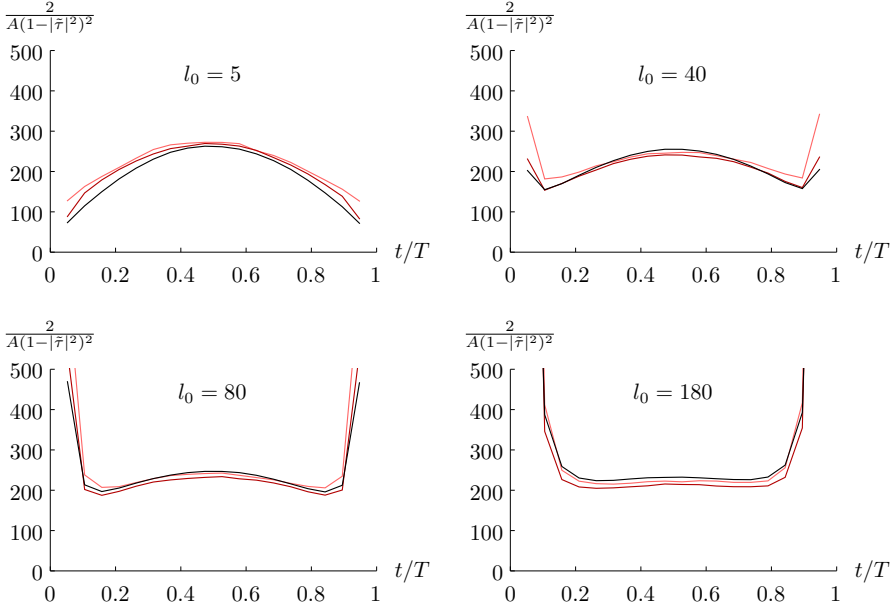
Figure 5.7: *The rescaled inverse correlators $P_{11}(t,t)/c_1$ (light red) and $P_{22}(t,t)/c_1$ (dark red) together with a plot of $2/(A[g](1 - |\tilde{\tau}|^2)^2)$ obtained from the measured expectation values. These are results from simulations at 3-volume $N_3 = 60\,000$, $k_0 = 2.5$, $T = 19$, and boundary lengths as indicated.*

correlators of the moduli to $2V/(1 - |\tilde{\tau}|^2)^2$ as in figure 5.6, but instead to

$$\frac{2}{A[g]} \frac{1}{(1 - |\tilde{\tau}|^2)^2}.$$ (5.34)

This we have done for a range of different parameters. In figure 5.7 we have plotted (in black) expression (5.34) as constructed from the expectation values $\langle A[\mathbf{T}_t] \rangle$ and $\langle \tilde{\tau}(t) \rangle$ for fixed coupling $k_0 = 2.5$, 3-volume $N_3 = 60\,000$, time extent $T = 19$, and various boundary lengths $l_0 = 5, 40, 80, 180$. In red we have plotted the diagonals $P_{11}(t,t)$ and $P_{22}(t,t)$ divided by a constant c_1, which is determined by a best fit for all four plots simultaneously as $c_1 \approx 0.75$. Although the fit is not perfect, we see that qualitatively the shapes of the curves, which change significantly with the boundary length, are well reflected in the inverse correlators.

The precise value of the proportionality constant c_1 is not very interesting, since it is related to the dimensionful couplings in certain lattice units. However, we can combine it with the proportionality constant c_0 that we deduced from the volume correlators in

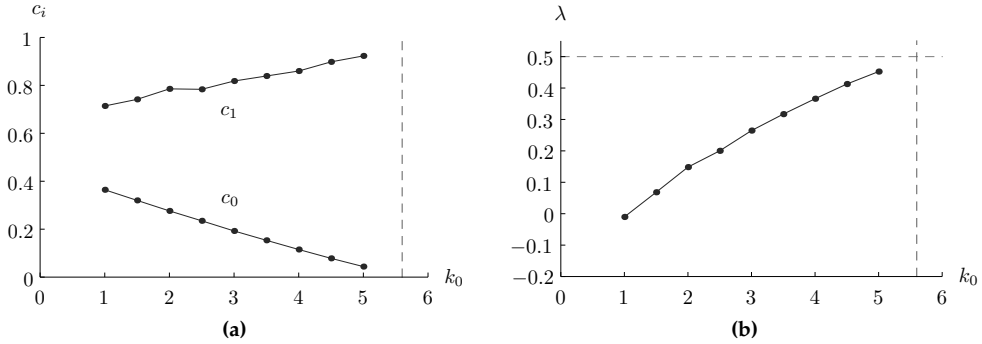**Figure 5.8:** *The measured values of (a) the effective couplings c_0 and c_1 and (b) $\lambda = 1/2 - c_0/c_1$ as function of the coupling k_0. All simulations were performed at 3-volume $N_3 = 60\,000$ and boundary lengths $l_0 = l_1 = 60$. The vertical dashed line corresponds to the critical coupling $k_0^* \approx 5.6$ and the horizontal dashed line to the conformal value $\lambda = 1/2$.*

section 4.5 to determine the value of the dimensionless coupling $\lambda = 1/2 - c_0/c_1$. From the data shown in figure 5.7 we deduce a value $\lambda \approx 0.22$. It turns out that the effective couplings c_0 and c_1, and therefore λ, depend only mildly on the 3-volume N_3 and the boundary conditions l_0 and l_1. Their dependence on the coupling k_0 is shown in figure 5.8. We see that when we increase k_0 towards the critical value $k_0^* \approx 5.6$, the parameter λ approaches $1/2$ from below.

What does it mean that the coupling λ approaches $1/2$? Recall from section 4.4 that the value of the coupling k_0 affects the number of 22-simplices in the system. Beyond the phase transition $k_0 > k_0^*$ the number of 22-simplices drops to the minimal number allowed by the requirements on the triangulation. Since consecutive spatial triangulations can only interact through the 22-simplices in between, we expect the coupling between the geometries to decrease with increasing k_0. This is certainly the case for the spatial volumes, as is apparent from the plot of c_0 in figure 5.8a. However, judging from the k_0-dependence of the dimensionful c_1, the moduli do not seem to decouple. At least, they decouple slower than the spatial volumes, judging only from the dimensionless quantity λ.

5.4 Conclusions

We have managed to fill in some of the gaps in our understanding of the effective action (5.1) of CDT on the torus. Both the correlations of the spatial volumes and the moduli are well described by an effective action of the form

$$S_{\text{eff}}[g_{ab}(t)] = \int_0^T \mathrm{d}t \left(\frac{c_0}{2} \frac{\dot{V}^2}{V} + \frac{c_1}{4A[g]} \frac{\dot{\tau}_1^2 + \dot{\tau}_2^2}{\tau_2^2} + \cdots \right). \tag{5.35}$$

This is in agreement with the general ansatz (5.16) in which the parameter λ is related to the couplings c_0 and c_1 through the relation $\lambda = 1/2 - c_0/c_1$. The parameters c_0 and c_1 are necessarily positive and therefore correspond to $\lambda < 1/2$. Clearly this excludes the special value $\lambda = 1$ which corresponds to the generally covariant case. A straightforward canonical analysis of the action (5.16) reveals that for $\lambda \neq 1/2$ the number of local physical degrees of freedom is equal to one. This is quite different from general relativity, which has no local physical degrees of freedom.

Where does this leave us? Suppose that the continuum action (5.16) correctly captures the observed dynamics of the space-time geometry and that this remains true in the infinite-volume limit. Then it seems that, as long as we are dealing with a system with a preferred time foliation, there is no way of getting rid of the spurious local degree of freedom, unless some new local symmetry emerges in the system. In the present setup of the model of CDT we see little room for such new symmetries. The only concrete opportunity we see is when λ becomes equal to $1/2$, at which point the kinetic term of pure trace degrees of freedom disappears. According to figure 5.8b we approach such a point when we tune the CDT coupling k_0 towards its critical value.

Let us try to understand why the moduli seem not to decouple when approaching the phase transition. A possible explanation for this comes from the fact that the moduli are topological degrees of freedom, which are absent in the spherical case. As we will see in section 6.2, in CDT with spherical spatial topology having a minimal number of 22-simplices does not put any restrictions on the spatial triangulations. However, in the case of the torus, in order to arrive at a small number of 22-simplices, the spatial tori have to contain short topologically non-trivial loops. As a consequence the number of triangles that significantly contribute to the moduli, i.e. the ones with large area in the harmonic embedding, becomes small. It might well be that precisely these triangles remain coupled by the few 22-simplices, while most of the spatial volume sits in decoupled spatial baby universes.

On the other hand, we derived our ansatz for the correlations of the moduli from the full effective action (5.16), in which λ affects not only topological degrees of freedom. To see whether the difference between the conformal modes and the traceless modes

is also present locally, we will attempt to probe individual components of the extrinsic curvature in chapter 6.

Let us end this chapter with an outlook on how we can go beyond the kinetic term (5.35) in the effective minisuperspace action. In particular, we would like to have an action depending only on the spatial volume and the moduli that describes both the average trajectories and the correlations. Once we find an expression that relates the curvature functional $A[g]$ to the spatial volume and the moduli, the form of the kinetic term is fixed by the correlations according to (5.35). The remaining challenge is to establish a potential $U(V, \tau)$ for the spatial volume and moduli, in such a way that the classical solutions agree with the average trajectories that we described in section 5.2. A first hint towards a suitable potential comes from our derivations in appendix C. There we show that, in the case that $A(V)$ scales "classically", $A(V) \propto 1/V$, a potential $U(V, \tau)$ proportional to $1/V$ yields a class of solutions containing all the general relativistic solutions that we encountered in sections 4.3 and 5.2.

Fixed boundaries in CDT

A major challenge faced by any approach to quantum gravity is the identification of relevant observables. If the fundamental theory possesses a diffeomorphism symmetry, the observables are required to be diffeomorphism-invariant. Such observables are in general hard to construct as they are necessarily non-local. This is a fact that we are well aware of in the context of CDT, although the situation is slightly better due to the presence of a preferred time slicing. It allows us to construct quantities that explicitly refer to this time slicing. As a consequence, we can construct observables which are local in time but will still be non-local in space. In chapters 4 and 5 we have studied precisely observables of this type, namely, the spatial volume and the moduli parametrizing the shape of the spatial geometry at a certain fixed time. From their measurements we have learned some non-trivial facts about the effective dynamics of the global degrees of freedom associated to them.

To obtain observables that are local in space we should in some way break the spatial diffeomorphism symmetry. One way to achieve this is by fixing the geometry of one of the time slices, say, at time $t = 0$, in which case we can regard it as a non-trivial initial boundary condition. If the two-dimensional geometry does not possess any symmetries, we can geometrically distinguish its points (at least in principle) and attach observables to them. In particular, we can fix a spatial coordinate system x^i at $t = 0$ and define an observable that measures some aspect of the space-time geometry in the vicinity of a point with given coordinates. A natural observable associated to a surface embedded in a three-dimensional geometry is the extrinsic curvature tensor $K_{ab}(x)$. It is this quantity that we will attempt to measure in our CDT simulations. In the ADM formalism (see section 4.3) the extrinsic curvature is related to the time derivative of the

Some of the results in this chapter have appeared in [32].

spatial metric. This means that the correlations of the extrinsic curvature can be directly related to the kinetic term for the spatial metric in the effective action. We will make this correspondence precise in section 6.1.

In order for a tensor object like the extrinsic curvature to make sense in a discrete setting, it is necessary that the triangulation on which it lives approximates a Riemannian manifold. This means that in our CDT simulations we have to put in "nice" boundary triangulations by hand. In section 6.3 we will consider spatial topology of the torus for which we can construct boundary triangulations simply from a regular triangular lattice. By contrast, in section 6.2 we will be interested in smoothly curved boundary geometries. Such triangulations can be constructed using a method called *Poisson–Delaunay triangulation*, which is briefly described in appendix E.

6.1   Extrinsic curvature in the continuum

In section 5.3 we put forward an ansatz for the effective action for CDT inspired by the presence of a preferred time foliation, namely,

$$S_{\text{eff}}[g_{ab}, N^a] = \kappa \int_0^T \mathrm{d}t \int \mathrm{d}^2x \sqrt{g} \left(K_{ab} \mathcal{G}_\lambda^{abcd} K_{cd} - U[g] \right), \tag{6.1}$$

where the extrinsic curvature is given by

$$K_{ab} = \frac{1}{2} \left(\dot{g}_{ab} - \nabla_a N_b - \nabla_b N_a \right) = \frac{1}{2} \left(\dot{g}_{ab} - (\mathcal{L}_N g)_{ab} \right), \tag{6.2}$$

and $\mathcal{G}_\lambda^{abcd}$ is the generalized Wheeler–DeWitt metric

$$\mathcal{G}_\lambda^{abcd} = \frac{1}{2} (g^{ac} g^{bd} - g^{ad} g^{bc}) - \lambda \, g^{ab} g^{cd}. \tag{6.3}$$

In this chapter we will be concerned with CDT simulations with fixed non-degenerate boundaries, therefore we consider boundary conditions $g_{ab}(0) = g_{ab}^0$ and $g_{ab}(T) = g_{ab}^1$.

Let us briefly summarize how we got to the ansatz (6.1). We started by taking the Euclidean Einstein–Hilbert action and restricting its domain to the space-time geometries having a fixed distance T between the initial and final boundaries. As a consequence of this restriction all these geometries possess a canonical time slicing, compatible with the boundaries, given by the surfaces of constant distance to the initial boundary. In this time-slicing the Einstein–Hilbert action becomes of the form of a point particle moving through the infinite-dimensional superspace $\mathcal{M}$ of two-dimensional metrics. However, the superspace $\mathcal{M}$ comes equipped with a metric, the Wheeler–DeWitt metric, which is not positive definite. To arrive at the action (6.1) we replaced this metric with the more

general, but still ultra-local, metric $\mathcal{G}_\lambda^{abcd}$ given in (6.3), which is positive definite for $\lambda < 1/2$.

In sections 4.5 and 5.3 we observed that the correlations of the fluctuations in the spatial volume and the moduli are most sensitive to the kinetic term in (6.1). Let us discuss this relation between the quantum fluctuations of observables and the effective kinetic term using the interpretation of (6.1) as the action of a point particle in super-space. Consider the action

$$S[q^i(t)] = \int dt \left(\frac{1}{2} \dot{q}^i \mathcal{G}_{ij}(q) \dot{q}^j - U(q) \right) \tag{6.4}$$

for the coordinates q^i of a point particle in a curved configuration space with metric $\mathcal{G}_{ij}(q)$ and potential $U(q)$. When we fix q^i at time $t = 0$ and $t = T$ there will be a unique classical solution which we denote by $q_0^i(t)$. Now we write $q^i(t) = q_0^i(t) + \delta q^i(t)$ and expand the action to second order in δq^i,

$$S[q] = S[q_0] + \int_0^T dt \, \delta q^i \left(-\partial_t (\mathcal{G}_{ij}(q_0)\partial_t \cdot) - \partial_i \partial_j U(q_0) \right) \delta q^j. \tag{6.5}$$

In a semi-classical treatment the expectation values of q^i are given by the classical solution $q_0(t)$,

$$\langle q^i(t) \rangle = q_0^i(t), \tag{6.6}$$

and the correlation functions of the fluctuations follow from the inverse of the operator appearing in (6.5),

$$\langle q^i(t)q^i(t') \rangle - \langle q^i(t) \rangle \langle q^i(t') \rangle = \langle \delta q^i(t) \delta q^j(t') \rangle = \left(-\partial_t (\mathcal{G}_{ij}(q_0)\partial_t \cdot) - \partial_i \partial_j U(q_0) \right)^{-1}(t,t'). \tag{6.7}$$

It is not hard to see that this inverse operator treated as function of t is continuous at t' but its first derivative jumps by an amount equal to twice the inverse $\mathcal{G}^{ij}(q_0)$ of the metric $\mathcal{G}_{ij}(q_0)$. As a consequence to leading order in $(t - t')$ we have

$$\langle (q^i(t) - q^i(t'))(q^j(t) - q^j(t')) \rangle = |t - t'| \mathcal{G}^{ij}(q^0(t)) + \mathcal{O}(|t - t'|^2). \tag{6.8}$$

So by measuring the correlations of differences of the configuration variables between one moment in time and a short time later we can deduce the configuration space metric. In particular, if we take $t' = 0$ we find

$$\langle q^i(t)q^j(t) \rangle - \langle q^i(t) \rangle \langle q^j(t) \rangle = t \, \mathcal{G}^{ij}(q^0(0)) + \mathcal{O}(t^2). \tag{6.9}$$

We see that close to the boundary the fluctuations are completely determined by the kinetic term. We will use this fact throughout the rest of this chapter to test the ansatz (6.1).

Let us apply this reasoning to the spatial metric g_{ab}. It is convenient at this point to assume that we have fixed a coordinate system at $t = 0$ and have propagated it such that the shift N^a vanishes identically (at least close to the initial boundary). In this way we can view the full spatial metric $g_{ab}(x)$ as configuration variables and (6.9) becomes

$$\langle g_{ab}(x,t)g_{cd}(x',t)\rangle - \langle g_{ab}(x,t)\rangle\langle g_{cd}(x',t)\rangle = \frac{2t\,T}{\kappa}\mathcal{G}^\lambda_{abcd}\frac{\delta(x,x')}{\sqrt{g}} + \mathcal{O}(t^2), \qquad (6.10)$$

where $\mathcal{G}^\lambda_{abcd}$ is the inverse supermetric

$$\mathcal{G}^\lambda_{abcd} = \frac{1}{2}(g_{ac}g_{bd} - g_{ad}g_{bc}) - \mu\,g_{ab}g_{cd} \quad \text{with } \mu = \frac{\lambda}{2\lambda - 1}, \qquad (6.11)$$

which is to be evaluated at $t = 0$.

In the case of vanishing shift, the extrinsic curvature $K_{ab}(x)$ is simply given by one half the time derivative $\dot{g}_{ab}$ of the metric at $t = 0$. Therefore, according to (6.10) its correlation function $\langle K_{ab}(x)K_{cd}(x')\rangle$ diverges, which is simply a consequence of the Heisenberg uncertainty principle. To obtain a sensible correlation we introduce the *regularized extrinsic curvature* $\tilde{K}_{ab}$, given by the time average of K_{ab} over a small fixed time interval Δt,

$$\tilde{K}_{ab}(x) = \frac{g_{ab}(x,\Delta t) - g_{ab}(x,0)}{2\Delta t} = \frac{1}{\Delta t}\int_0^{\Delta t} \mathrm{d}t\, K_{ab}(x,t). \qquad (6.12)$$

In terms of $\tilde{K}_{ab}$ the relation (6.10) implies a correlation function at the boundary given by

$$\langle \tilde{K}_{ab}(x)\tilde{K}_{cd}(x')\rangle = \frac{1}{2\Delta t\,\kappa}\mathcal{G}^\lambda_{abcd}\frac{\delta(x,x')}{\sqrt{g}} + \mathcal{O}(\Delta t^0). \qquad (6.13)$$

In CDT we have a natural short-time cut-off Δt given by the distance between the initial boundary and the spatial triangulation at time $t = 1$. With this Δt the regularized extrinsic curvature $\tilde{K}_{ab}$ should capture how the spatial geometry changes when going from the boundary $t = 0$ to the triangulation at $t = 1$. We can split $\tilde{K}_{ab}$ into two parts, a pure trace $\tilde{K} = g^{ab}\tilde{K}_{ab}$ and a traceless part $\tilde{K}_{ab} - 1/2 g_{ab}\tilde{K}$. The latter, which corresponds to the traceless metric deformations, turns out to be very hard to measure in the CDT configuration. The trace $\tilde{K}$ on the other hand corresponds to changes in the local volume and has a simple interpretation in the triangulation. Therefore we will first see what we can learn from studying the trace $\tilde{K}$ of the extrinsic curvature alone. In section 6.3 we will revisit the traceless deformations by introducing an approximation, namely, that the regularized extrinsic curvature $\tilde{K}_{ab}$ is closely related to the real extrinsic curvature at the boundary in the sense of piecewise linear manifolds.

It follows from (6.13) that the trace $\tilde{K}(x)$ is correlated according to

$$\langle \tilde{K}(x)\tilde{K}(x') \rangle = \frac{\delta(x,x')}{\Delta t\, \kappa(\frac{1}{2} - \lambda)\sqrt{g}}, \tag{6.14}$$

but this is not a very interesting ansatz to test as it predicts a position-independent ultra-local correlation. Moreover, it does not allow us to determine the parameter λ itself, since it appears only in combination with the dimensionful coupling κ.

It turns out that we can get more non-trivial information from measuring the trace $\tilde{K}$ in the special situation $T \to 0$. We can mimic this regime in CDT by reducing the number T of slices of tetrahedra to one, i.e. we take two fixed triangulations and the only freedom is in the way they are connected. We will study this system in detail in the next section. First let us see what happens to our ansatz in this limit. The main simplification is that, as long as we keep the boundary conditions at $t = 0$ and $t = T$ fixed, the potential $U[g]$ becomes irrelevant in the action (6.1) as $T \to 0$. Therefore we end up with an action which is precisely that of geodesics in superspace. To make this more precise let us eliminate the shift N^a. We cannot simply set the shift N^a to zero identically while fixing the metric on the boundary, because that would force the coordinate systems on the initial and final boundary to align. To make sure that we do not change the equations of motion when setting $N^a = 0$, we should not fix the spatial metric at $t = T$ but only the spatial geometry. We can do this by introducing a spatial diffeomorphism f at the final boundary, i.e. we fix the initial metric to g^0_{ab} and the final metric to the pull-back $(f^*g^1)_{ab}$ of g^1_{ab}. By allowing both the metric $g_{ab}(t)$ and the diffeomorphism f to be varied in the action we can safely put $N^a = 0$, leading to the action

$$S[g_{ab}, f] = \frac{\kappa}{4} \int_0^T \mathrm{d}t \int \mathrm{d}^2 x \sqrt{g}\, \dot{g}_{ab}\mathcal{G}^{abcd}_\lambda \dot{g}_{cd} \quad \text{and} \quad g_{ab}(0) = g^0_{ab},\, g_{ab}(T) = (f^*g^1)_{ab}. \tag{6.15}$$

We will be interested in the dynamics of f and therefore we would like to eliminate g_{ab} from this action. It is not hard to see that in order to obtain $S[f]$ to second order in f we can plug in for g_{ab} its classical solution, i.e. the geodesic connecting g^0_{ab} and $(f^*g^1)_{ab}$.[22] The action for f then becomes simply

$$S[f] = \frac{\kappa}{4T}d(g^0, f^*g^1)^2, \tag{6.16}$$

where $d(\cdot, \cdot)$ is the $\mathcal{G}_\lambda$-distance function in superspace.

---

[22]The reason for this is that the fluctuations of g_{ab} around the geodesic do not couple to the fluctuations in f.

If we take g^1_{ab} identical to g^0_{ab} and $\lambda < 1/2$ the minima of (6.16) are clearly given by the isometries of g^0_{ab}. In the next section we illustrate that this classical behaviour is qualitatively reproduced in CDT.

Assuming that f fluctuates around the identity map, we can write $f(x^a) = x^a + N^a(x)$ in terms of a vector field N^a, which for obvious reasons we call the shift vector field. Then (6.16) becomes

$$S[N^a] = \frac{\kappa}{4T} \int \mathrm{d}^2x \sqrt{g} (\mathcal{L}_N g^0)_{ab} \mathcal{G}_\lambda^{abcd} (\mathcal{L}_N g^0)_{cd}, \tag{6.17}$$

which we can rewrite as

$$S[N^a] = \frac{\kappa}{4T} \int \mathrm{d}^2x \sqrt{g} \left(\frac{1}{2}(dN)_{ab} g^{ac} g^{bd} (dN)_{cd} + (1-\lambda)(\nabla_a N^a)^2 - R_{ab} N^a N^b \right), \tag{6.18}$$

where $(dN)_{ab} = \nabla_a N_b - \nabla_b N_a$ is the exterior derivative of N_a viewed as 1-form. We can interpret $\rho = \nabla_a N^a$ as the divergence part and dN as the rotational part of the vector field, which together determine N^a. In general both parts interact with each other through the curvature term, unless we have a constant Ricci curvature $R_{ab} = \frac{1}{2} R g_{ab}$ like in the case of the 2-sphere S^2. In that case we can write down an action just in terms of the divergence ρ,

$$S[\rho] = \frac{\kappa}{4T} \int \mathrm{d}^2x \sqrt{g} \, \rho (1 - \lambda - \frac{1}{2} R \Delta^{-1}) \rho, \tag{6.19}$$

where Δ^{-1} is the inverse Laplacian with the constant mode projected out.[23]

If we choose the time cut-off Δt for the regularized extrinsic curvature equal to T, the trace $\tilde{K}$ is related to divergence by $\tilde{K} = \rho/(2T)$. Hence, we obtain from (6.19) the correlation function

$$\langle \tilde{K}(x)\tilde{K}(x') \rangle = \frac{(1 - \lambda - R\Delta^{-1}/2)^{-1}(x, x')}{T \kappa \sqrt{g}}. \tag{6.20}$$

A more convenient form is obtained by expanding $\tilde{K}$ in terms of normalized eigenfunctions ϕ_i of the Laplacian, i.e. $\tilde{K} = \sum \tilde{K}_i \phi_i$ with $\int \mathrm{d}^2x \sqrt{g} \phi_i \phi_j = \delta_{ij}$ and $\Delta \phi_i = \lambda_i \phi_i$,

$$\langle \tilde{K}_i \tilde{K}_j \rangle = \frac{\delta_{ij}}{T \kappa} \frac{\lambda_i}{(1-\lambda)\lambda_i - R/2}. \tag{6.21}$$

We see that here, in contrast to the finite-T case in (6.14), we can deduce information about λ from the measurement of $\tilde{K}$ because of the presence of a curvature term. In the next section we will compare (6.21) to measurements and obtain a preliminary dependence of λ on the couplings.

---

[23]By definition the constant mode of ρ is required to vanish, $\int \mathrm{d}^2x \sqrt{g} \rho = \int \mathrm{d}^2x \sqrt{g} \nabla_a N^a = 0$
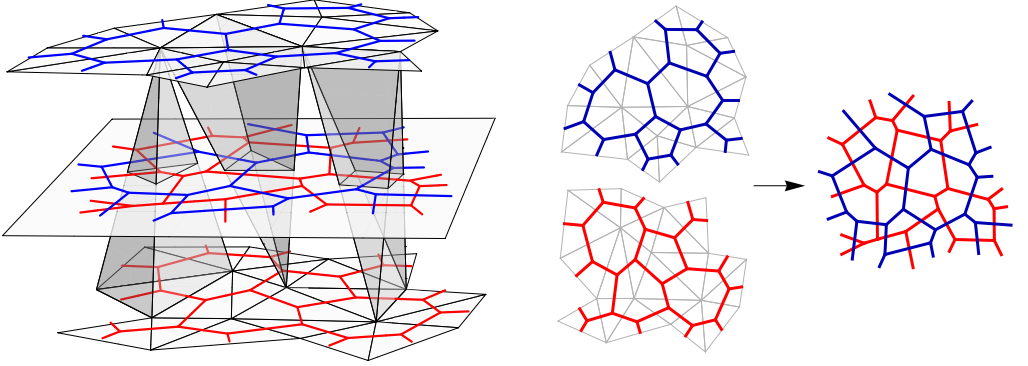
Figure 6.1: *A slice of tetrahedra bounded by two 2D triangulations is characterized by a superposition of two three-valent graphs.*

6.2 Single-slice configuration

Before we go into the details of the CDT simulations, let us introduce a convenient graphical representation for the single-slice configurations [13]. Such configurations consist of two spatial triangulations which are connected by tetrahedra. We can represent the spatial triangulations by their dual three-valent graphs. In the case of spherical topology, which we will restrict to in this section, these three-valent graphs are planar, i.e. we can embed them in the plane (or in the sphere) without intersections. It turns out that we can characterize a configuration of tetrahedra connecting them by superimposing both graphs in a non-trivial way (see figure 6.1). More precisely, a single slice configuration corresponds to a bicoloured graph containing three-valent red vertices dual to 31-simplices, three-valent blue vertices dual to 13-simplices, and mixed four-valent vertices dual to 22-simplices.

Since we are keeping the spatial triangulations fixed the CDT partition function (4.2) reduces to a sum over inequivalent superpositions of the blue and red graphs. Notice also that the number N_0 of vertices does not depend on the configuration and the number N_3 of tetrahedra is given up to an additive constant by the number N_{22} of 22-simplices. Therefore the CDT partition function (4.2) for $T = 1$ reduces (up to an
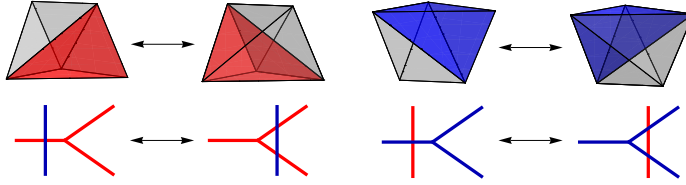
Figure 6.2: *The set of update moves used in the single-slice Monte Carlo simulations.*

overall factor) to[24]

$$Z_{T=1}[\mathbf{T}_0, \mathbf{T}_1, k_3] = \sum_{\mathbf{T} \in \mathcal{T}} e^{-k_3 N_{22}}. \tag{6.22}$$

In terms of the graph representation, N_{22} represents the number of intersections of the blue and the red graph.

To evaluate expectation values we use the Monte Carlo methods described in 4.1. Since we are keeping the spatial triangulations fixed, we only need one of the three types of local update moves. This move is shown in figure 6.2 and amounts to pulling a red or blue vertex across an edge of the opposite colour and the reverse of this operation. The initial configuration we have to put in by hand and for this we construct a configuration with a minimal number of 22-simplices.[25] In such a minimal configuration all but one of the 31-simplices point to the same vertex and similarly for the 13-simplices (see figure 6.3a). To complete such a degenerate configuration one has to add four 22-simplices.

We expect the expectation value for the number N_{22} of 22-simplices to decrease with increasing coupling k_3, since this coupling acts like a chemical potential. This is indeed the case as can be seen in figure 6.3b. We obtained this figure by performing simulations at different values of the coupling k_3 and spherical boundary triangulations consisting of 500 triangles. Clearly a phase transition is present at k_3 equal to $k_3^* \approx 1.6$. Larger values of k_3 result in minimal configurations of the type mentioned before. We will restrict our attention to the phase $k_3 < k_3^*$ where it seems that 22-simplices are spread out rather uniformly among the edges.

---

[24]We assume that either one of the boundary triangulations has a trivial automorphism group or that we have fixed a labelling of the boundary vertices. In both cases we do not need to worry about the symmetry factor $C_{\mathbf{T}}$ appearing in (4.2).

[25]In CDT we put certain restrictions on the connectivity of the tetrahedra. In terms of the dual graphs these restrictions amount to the following (see [13]): 1) The red and blue graph should intersect at least once; 2) the intersection of a blue cell with a red cell should be connected; 3) the intersection of a blue edge with a red cell should be connected and vice versa. From these restrictions one can deduce that the minimal number of intersections in the case of spherical topology is four.
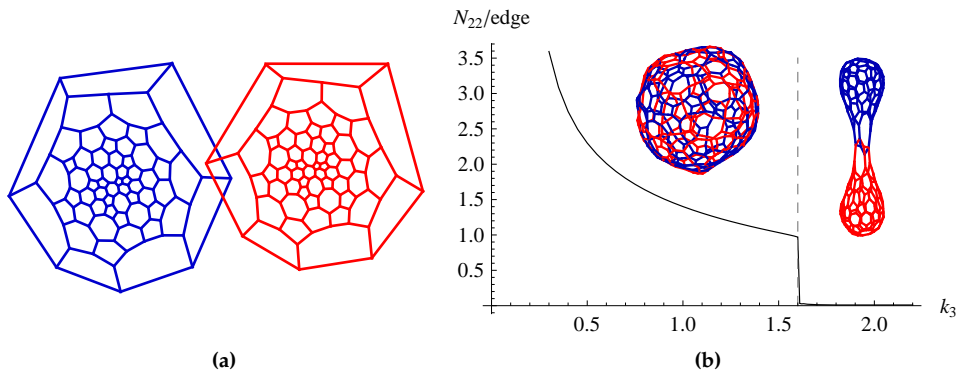
Figure 6.3: *(a) A minimal single-slice configuration. (b) The expectation value for the number N_{22} of 22-simplices per edge of the initial boundary as a function of the coupling k_3. Two typical configurations on either side of the phase transition are depicted.*

In section 6.1 we observed that in the case of identical boundary geometries, the minimum of the effective action (6.16) occurs when the boundaries align isometrically. To illustrate that something similar happens in CDT we have constructed, using the methods outlined in appendix E, a triangulation with 300 triangles approximating an ellipsoid (to be more precise, a prolate ellipsoid with eccentricity $\epsilon = 0.7$). We then performed simulations using this triangulation at both boundaries $\mathbf{T}_0$ and $\mathbf{T}_1$ and with coupling $k_3 = 1.2$. To see how both triangulations align we have colour-marked a couple of vertices in the initial triangulation (see figure 6.4), two blue vertices at the tips of the ellipsoid and four red vertices on the equator. Then we measured how often a triangle in the final triangulation is connected through a 13-simplex to one of these coloured vertices. The result is shown on the right-hand side of figure 6.4, where we coloured the triangles according to these measurements. We observe a clear preference of the system to sit in a configuration in which the tips and the equators of the triangulations are approximately aligned. This illustrates nicely how the CDT partition function dynamically determines the alignment of its spatial geometries.

In this sense CDT seems to implement a statistical version of the *best matching principle* [24] in space-time. Let us briefly discuss what we mean by this in the current context. A classical solution to the action (6.1) determines a path in the space of two-dimensional geometries, i.e. the space of orbits of the spatial diffeomorphism group in the superspace $\mathcal{M}$ of two-dimensional metrics. Given such a path, to reconstruct the full space-time geometry (in the gauge $N^a = 0$) we need to lift it to a path $t \rightarrow g_{ab}(t)$ in the superspace $\mathcal{M}$ itself. This can be done consistently by demanding the lifted path
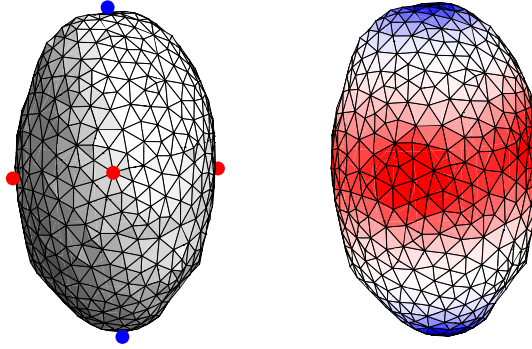
Figure 6.4: *Two spatial triangulations approximating an ellipsoid: we have marked several vertices on the first and coloured the triangles of the second according to how often they connect to them through 13-simplices.*

to be perpendicular to the gauge orbits with respect to the supermetric $\mathcal{G}_\lambda$. In other words, given a metric $g_{ab}(t)$ at some time t and a geometry at time $t + \delta t$, we should choose spatial coordinates at time $t + \delta t$ such that the metric $g_{ab}(t + \delta t)$ is as close as possible to $g_{ab}(t)$, as measured by $\mathcal{G}_\lambda$. To see whether it is really the supermetric $\mathcal{G}_\lambda$ that effectively determines the alignment in CDT we will perform a quantitative analysis of the deviations from isometry. However, to do this we switch to spherically symmetric boundary conditions, for which we have the explicit ansatz (6.21).

The quantity we want to probe is $\tilde{K}$, the trace of the (regularized) extrinsic curvature (6.12). If the metrics on the boundary are close to each other, as we will assume here, $\tilde{K}$ can also be written in terms of the ratio of the volume forms,

$$\tilde{K}(x) = \frac{1}{T}\left(\frac{\sqrt{g(x,T)}}{\sqrt{g(x,0)}} - 1 \right). \tag{6.23}$$

This expression allows for a rather straightforward discretization. Given a vertex v in $\mathbf{T}_0$, we can associate to it a volume (in units of the volume of a triangle) in $\mathbf{T}_1$ equal to the number $n_{13}(v)$ of triangles in $\mathbf{T}_1$ that are connected to v through a 13-simplex. A corresponding volume in $\mathbf{T}_0$ is given by one third of the degree $n_2(v)$ of v, i.e. the number of triangles attached to v.[26] Putting $\Delta t = 1$ we therefore arrive at our discrete definition

$$\tilde{K}(v) := 3\frac{n_{13}(v)}{n_2(v)} - 1. \tag{6.24}$$

---

[26]The factor of three is due to the fact that the volume of a triangle is shared by three vertices.

In a CDT simulation we can easily measure the expectation value $\langle \tilde{K}(v) \rangle$ and the correlations $\langle \tilde{K}(v)\tilde{K}(v') \rangle$. This we have done for triangulations $\mathbf{T}_0 = \mathbf{T}_1$ consisting of 1600 triangles approximating a round 2-sphere and various values of the coupling k_3. We find that the $\langle \tilde{K}(v) \rangle$ for all vertices v are distributed closely around zero, however, at the level of individual vertices there are systematic deviations from zero of the order 0.05. This means that to large extent the expectation value $\langle n_{13}(v) \rangle$ for the number of 13-simplices at a vertex v is determined by its degree $n_2(v)$, but that the further structure of the triangulation around v also has a small but statistically significant influence. To correct for these systematic deviations in the correlations, we will from now on subtract from $\langle \tilde{K}(v)\tilde{K}(v') \rangle$ the small quantity $\langle \tilde{K}(v) \rangle \langle \tilde{K}(v') \rangle$.

To test (6.21) we need to expand $\tilde{K}(v)$ in terms of eigenmodes ϕ_i of the Laplacian on $\mathbf{T}_0$. A natural discretization of the Laplacian acting on real functions with support on the vertices is given by

$$(\Delta f)(v) = \frac{1}{n_2(v)} \sum_{v'} \left(f(v) - f(v') \right), \tag{6.25}$$

where the sum is over the vertices v' adjacent to v. This Laplacian is self-adjoint with respect to the inner product

$$\langle f, f' \rangle_{\mathbf{T}_0} = \sum_v \frac{n_2(v)}{3} f(v) f'(v). \tag{6.26}$$

Numerically we can easily find the eigenvalues λ_i of Δ on $\mathbf{T}_0$ and the corresponding normalized eigenmodes $\phi_i(v)$.[27] Recall that we should exclude the constant eigenmode ϕ_0 corresponding to $\lambda_0 = 0$, as we are only interested in the non-constant modes. We can now express the modes of $\tilde{K}$ as

$$\tilde{K}_i = \langle \phi_i, \tilde{K} \rangle_{\mathbf{T}_0}. \tag{6.27}$$

First of all we find that to high accuracy the matrix $\langle \tilde{K}_i \tilde{K}_j \rangle$ is diagonal, so we can restrict our attention to the values $\langle \tilde{K}_i^2 \rangle$. According to the ansatz (6.21), if we plot $\lambda_i / \langle \tilde{K}_i^2 \rangle$ against λ_i we should get a straight line. We have done this for three different values of the coupling k_3 in figure 6.5a showing the first 24 eigenvalues. At least for couplings $k_3 \lesssim 1.5$ we observe a good linear behaviour. According to (6.21) the effective coupling λ is related to the value ξ at which the linear fit intersects the horizontal axis. Using the fact that on a round 2-sphere the scalar curvature R in the continuum coincides with the first couple of eigenvalues $\lambda_1 = \lambda_2 = \lambda_3$ we find

$$\lambda = 1 - \frac{\lambda_1}{2\xi}. \tag{6.28}$$

---

[27]The continuum eigenvalues on the unit sphere are $0, 2, 2, 2, 6, 6, 6, 6, 6, 12, 12, \ldots$. Up to an overall factor the eigenvalues λ_i on $\mathbf{T}_0$ closely approximate these, at least for small i.
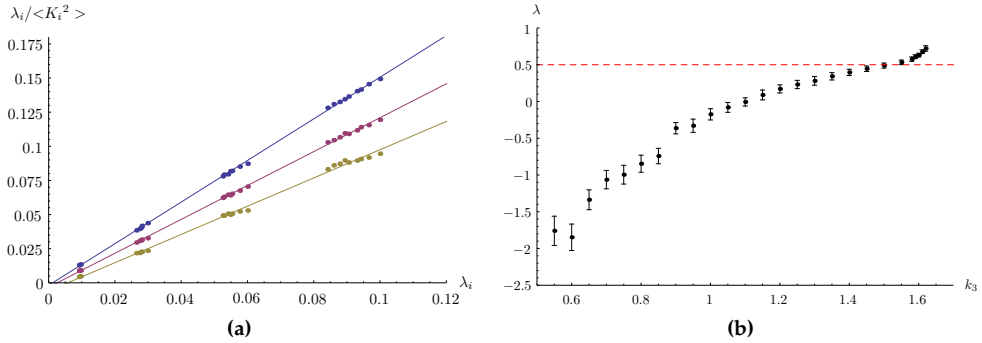
Figure 6.5: *(a) The autocorrelation $\langle \tilde{K}_i^2 \rangle$ of the Fourier modes $\tilde{K}_i$ compared to the eigenvalues λ_i for different values of $k_3 = 0.4, 0.8, 1.2$ (the top curve corresponds to $k_3 = 0.4$). Solid lines correspond to best linear fits. (b) The parameter λ extracted from best linear fits as function of the coupling k_3.*

The special value $\lambda = 1/2$, at which point the metric $\mathcal{G}_\lambda$ becomes indefinite, occurs when $\xi = \lambda_1$, i.e. when the fluctuations in the lowest modes diverge, $\langle \tilde{K}_1^2 \rangle \to \infty$. The dependence of λ on the coupling k_3 is shown in figure 6.5b.

Several remarks are in order. First of all, as far as the trace of the extrinsic curvature is concerned, our measurements agree with the ansatz that the system is effectively described by a generalized Wheeler–DeWitt kinetic term with parameter λ. We see that the observed phase transition corresponds to λ approaching the value $1/2$ at which $\mathcal{G}_\lambda$ becomes degenerate. Now we can also understand the two phases from the effective action (6.16): in the phase $\lambda < 1/2$ the configuration fluctuates around isometric identifications f, while for $\lambda > 1/2$ the minimum is obtained by maximizing the change in conformal factor. Qualitatively it is clear that such a minimum can be achieved by a Dirac delta-like volume distribution, which is what happens in our simulations for $k_3 > k_3^*$.

There are a number of drawbacks to this approach. Foremost, our determination of λ rested upon the fact that the amplitude of the extrinsic curvature fluctuation is not completely scale-invariant. The scale invariance is broken by the appearance of the curvature of the 2-sphere. To determine λ we use the deviations at the global curvature scale, which is necessarily a small energy scale. In figure 6.5a we determine λ by fitting a straight line to only the first few eigenmodes, and especially for small k_3 the fits are hardly distinguishable from intersecting the origin, leading to large error bars. Increasing the system size does not significantly improve the results, because the curvature scale will decrease accordingly.

A second drawback is that we cannot directly compare these results to unconstrained CDT simulations. In particular, there is no straightforward way to relate the single coupling k_3 we have here to the two couplings k_0 and k_3 that we usually have. One way to relate the systems is to look at the number of 22-simplices per spacelike edge. In other words, we use the 1-to-1 map in figure 6.3b. However, it turns out that this quantity depends sensitively on the local structure of the boundary triangulations we put in by hand.

In the next section we pursue another approach, which does not suffer from these two problems, by attempting to verify the local correlation (6.13) directly.

6.3 Regular torus boundary

In the following we will consider CDT configurations with more than one time slice. We will take the time extent large enough for the fluctuations at the initial boundary not to be influenced any more by the presence of the final boundary. Our simulations are performed with $T = 6$ time slices, but we have observed that the results we obtain are already qualitatively present with just $T = 2$.

We are interested in the regularized extrinsic curvature $\tilde{K}_{ab}$ which measures the change in geometry when we go from the initial boundary at $t = 0$ to the first spatial triangulation at $t = 1$. We have seen that the trace $\tilde{K}$ can be quite easily probed, since it measures local volumes. The traceless degrees of freedom are much harder to probe: basically one has to define some region in the initial boundary, translate it to $t = 1$ and then measure how its shape has changed. We have so far not been able to define sensible local observables that do this directly. However, we do have an indirect probe of this change in geometry, namely, through the extrinsic curvature at the boundary when we view the triangulation as a piecewise linear manifold.

It is not hard to see that the extrinsic curvature of a two-dimensional triangulation, embedded in three dimensions, is a distribution with support on its edges (see also [31]). More precisely, suppose we choose Cartesian coordinates x^1, x^2 in the neighbourhood of an edge, such that the edge is given by $n_a x^a = 0$ with n^a a unit normal to the edge, then the extrinsic curvature is given by

$$K_{ab} = (\theta - \pi)\delta(n_a x^a)n_a n_b, \tag{6.29}$$

where θ is the exterior angle at which the planes meet in the three-dimensional triangulation. In a CDT configuration the angle θ at an edge e is up to a constant proportional to the number of 22-simplices $n_{22}(e)$ connecting to e (see figure 6.6a). As a consequence, the extrinsic curvature tensor K_{ab} is determined by the function $n_{22}(e)$ on the edges.
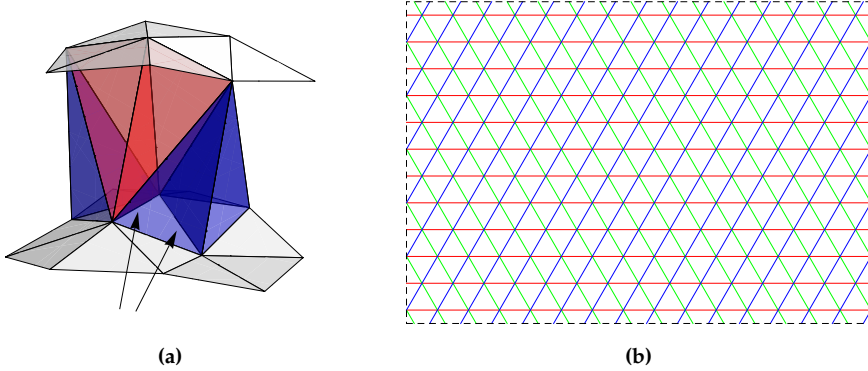
(a)   **(b)**

Figure 6.6: *(a) The extrinsic curvatures at the indicated edges differ by two units. (b) If we identify the opposite sides of this parallelogram we obtain a regular triangulation of the torus. A constant mode on this triangulation is one that assigns the same value to edges of the same colour.*

Therefore, in the CDT model, the $n_{22}(e)$ are the natural quantities to study in order to learn about the dynamics of K_{ab}.

We would like to identify this K_{ab} with the regularized extrinsic curvature $\tilde{K}_{ab}$ from section 6.1, but it is clear that the numbers of 22-simplices at every edge do not completely determine the geometry at $t = 1$. However, we expect large-scale features of the geometry to be reflected in these quantities. For example, a geometry elongated in a certain direction will have on average more 22-simplices at edges with normals pointing in that direction than at other edges. In the following we will assume that the two extrinsic curvatures are indeed related to each other. We have to keep in mind though that it is possible that the relation may involve a mixing of the trace and traceless parts of the two-tensor. To illustrate this, notice that the extrinsic curvature corresponding to a 22-simplex signals an expansion in the direction perpendicular to the edge to which it is attached. If we consider what a 22-simplex means for the change in geometry when we go from $t = 0$ to $t = 1$, we see that in addition to the expansion there is a contraction in the perpendicular direction, which is not taken into account in K_{ab} but does appear in $\tilde{K}_{ab}$. A consequence of this mixing is that the value of $1/2 - \lambda$ gets effectively rescaled, since it measures the ratio of the autocorrelation of the trace and traceless parts of the extrinsic curvature. With these considerations in mind we will simply take (6.13) as ansatz for the discrete extrinsic curvature K_{ab}.

The ansatz (6.13) predicts that the extrinsic curvatures only correlate ultra-locally and the parameter λ tells us how their correlation depends on the relative orientation
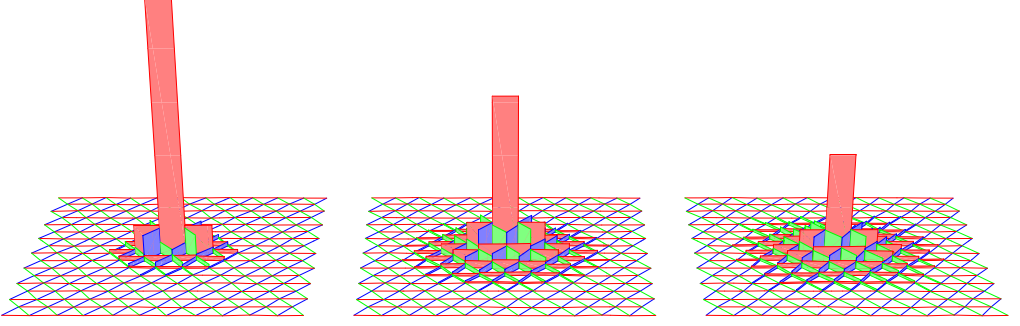
Figure 6.7: *Illustration of the correlation $C(e, e')$ for a fixed edge e and couplings k_0 equal to 2.5, 4.5 and 5.2 respectively (the highest peaks correspond to the autocorrelation $C(e, e)$).*

of the measurements. Upon discretization the correlation cannot remain ultra-local: if $n_{22}(e)$ would only correlate with itself we would never get a non-trivial correlation between extrinsic curvatures in different directions. In general, when discretizing a local continuum operator one always obtains errors proportional to higher-derivative terms. However, these higher-derivative terms will scale with the cut-off and therefore generically disappear in the continuum limit. To get an idea of the non-locality of the correlations we have measured

$$C(e, e') = \langle n_{22}(e) n_{22}(e') \rangle - \langle n_{22}(e) \rangle \langle n_{22}(e') \rangle \tag{6.30}$$

for various choices of boundary triangulations. In figure 6.7 results are shown for simulations in which we took the boundaries to be regular triangulated flat tori.

In general we find that $C(e, e')$ is non-zero only for edges e' in a finite neighbourhood of e.[28] The size of this neighbourhood grows with increasing coupling k_0 but is insensitive to the system size. This means that in the infinite-volume limit, while keeping k_0 fixed, only the ultra-local part survives. When the triangulation approximates a flat geometry we can extract this ultra-local part by measuring the correlation of the spatial averages of the extrinsic curvature components. According to the ansatz (6.13),

---

[28]For edges e and e' far apart $C(e, e')$ is not exactly zero but equal to some small constant value C_0. This non-local correlation is an artefact of our simulation set-up. For computational reasons we fix the total number of tetrahedra in the triangulation. This restriction leads effectively to an autocorrelation of the total number of 22-simplices in the first slice. We can compensate for this effect by determining C_0 and subtracting it from $C(e, e')$. Near the phase transition the correlation distance becomes of the order of the system size making it hard to determine C_0. In that case it is easier to determine and subtract the constant from the inverse of $C(e, e')$.

we should find

$$\left\langle \int \mathrm{d}^2x\sqrt{g}K_{ab}(x)\int \mathrm{d}^2x'\sqrt{g}K_{cd}(x') \right\rangle \propto \mathcal{G}^\lambda_{abcd}. \tag{6.31}$$

To minimize the ambiguity of determining this spatial average we take the boundary to be a regular triangulation of the torus (see figure 6.6b). The 22-simplices contribute to the spatial average of K_{ab} according to the orientations of the edges they are connected to. If we denote by n^1_{22}, n^2_{22} and n^3_{22} the numbers of 22-simplices connected to the red, green and blue edges respectively (see figure 6.6b), we have up to an overall factor

$$\int \mathrm{d}^2x\sqrt{g}K_{ab} \propto \begin{pmatrix} \frac{3}{4}(n^2_{22}+n^3_{22}) & \frac{\sqrt{3}}{4}(n^2_{22}-n^3_{22}) \\ \frac{\sqrt{3}}{4}(n^2_{22}-n^3_{22}) & n^1_{22}+\frac{1}{4}(n^2_{22}+n^3_{22}) \end{pmatrix}. \tag{6.32}$$

This allows us to express (6.31) in terms of the correlations of n^i_{22},

$$\langle n^i_{22} n^j_{22} \rangle \propto 6\delta^{ij}-1-2\mu = 6\delta^{ij} - \frac{4\lambda+1}{2\lambda-1}. \tag{6.33}$$

We have used (6.33) to determine λ for a system with boundary triangulations consisting of 768 triangles and a fixed total number of $15\,000$ tetrahedra. The results for various values of the coupling k_0 are shown in figure 6.8. The behaviour of λ as one approaches the phase transition is qualitatively similar to what we observed in the single-slice simulations (figure 6.5b). Close to the phase transition the system is dominated by fluctuations in the conformal factor. These fluctuations affect all directions equally and therefore lead to a correlation matrix which is direction-independent. From examining equation (6.33), this corresponds to the limit $\lambda \to 1/2$. One can also see this happening in figure 6.7: the colour asymmetry in the correlations decreases for increasing k_0, which is mainly due to the decrease of the autocorrelation $C(e,e)$. If we were able to make sensible measurements at the phase transition, the corresponding plot would show a correlation $C(e,e')$ between the edges e and e' that depends only on the distance between e and e' and not on their relative orientation. Of course, we observe finite-size effects in our system when we approach the phase transition and should therefore not trust the measurements for $k_0 \gtrsim 5.2$.

6.4 Conclusions

In this chapter we have again put to the test the ansatz that the geometries in CDT are effectively described by an action with a kinetic term given by the generalized Wheeler–DeWitt metric $\mathcal{G}_\lambda$. We find for different configurations that the fluctuations of the geometry near a fixed boundary are well described by $\mathcal{G}_\lambda$ with appropriately chosen value
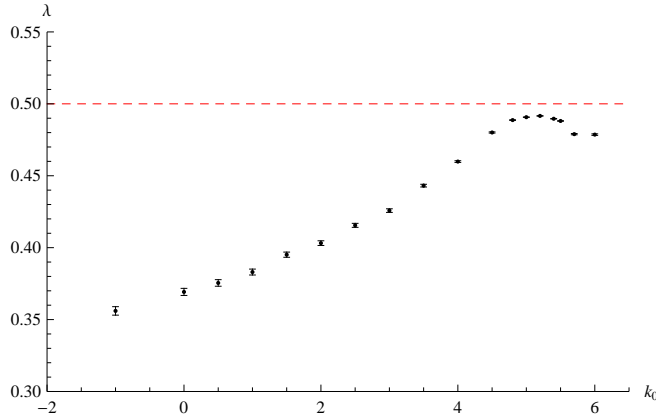
Figure 6.8: *Values for λ determined from the correlations of the numbers of 22-simplices in different orientations at a regular torus boundary with 768 triangles.*

λ. This should not come as too much of a surprise, since the form of the (generalized) Wheeler–DeWitt supermetric is the most general local supermetric one can form from the metric without derivatives. Its prediction for the extrinsic curvature correlations (6.13) corresponds to the simplest tensor operator that we can construct from the spatial metric. Of course, curvature terms could be involved but they would only produce corrections in regions where the spatial metric is strongly curved. Such corrections could provide non-trivial information about the effective action, but numerically it is hard to distinguish their effect from corrections due to the discretization. We chose to restrict to spatial geometries with approximately constant (zero or small) curvature to prevent such corrections from interfering with the measurements. In any case, we have learned in this chapter how to make contact between continuum extrinsic curvatures and observables in CDT.

The values of λ that we extract from the measurements put non-trivial restrictions on the effective action. We cannot compare directly the results from the single-slice configurations in figure 6.5b to the results in figure 6.8 from the last section, because of the different couplings involved. However, we can compare the latter to the values of λ that we obtained in chapter 5 from the moduli correlations. The curves in figures 5.8b and 6.8 differ roughly by a factor of four in $1/2 - \lambda$, a discrepancy which has remained after a careful check of all calculations. The conclusion at this stage is that this must be due to the approximations and non-trivial discretizations we had to make, some of which are known to have a significant effect on the overall normalization of $1/2 - \lambda$ (see for instance appendix D).

103

Qualitatively, though, all three plots (figures 5.8b, 6.5b, 6.8) lead to the same conclusion. As one approaches the phase transition in CDT, the strength of the kinetic term of the conformal factors decreases faster than that of the traceless modes of the spatial metric. This leaves open the possibility that near the phase transition an approximate spatial conformal symmetry appears, which might bring back the number of local physical degrees of freedom from one to zero, assuming that such a degree of freedom is indeed present. A hint in this direction comes from the fact that beyond the phase transition, at least for spherical spatial topology, the spatial triangulations completely decouple. In that case we are left with a number of independent two-dimensional dynamical triangulations, which we studied in chapters 2 and 3. These models are known to possess conformal properties and their continuum limit is rather well understood. Whether any of these properties survive when the coupling is lowered across the critical point is at present unknown.

CHAPTER 7

Shape dynamics in 2+1 dimensions

Our attempts to find an effective description of the large-distance limit of CDT have led us to consider actions with a symmetry group different from general relativity. If the continuum actions of the metric introduced in section 5.3 capture correctly the degrees of freedom of CDT, a more natural symmetry group to consider is the group of foliation-preserving diffeomorphisms. In the Lorentzian setting actions that break the refoliation symmetry of general relativity are usually deemed unphysical, especially in the light of recent tight bounds on variations in the speed of light [50]. In this chapter, however, we will show that a reduced diffeomorphism symmetry is not necessarily in contradiction with general relativity, if an additional symmetry group is present to maintain the correct number of physical degrees of freedom.

We will show that, without changing the classical content of the theory, the refoliation symmetry in general relativity can be traded for spatial conformal symmetry, at the expense of locality. This is achieved by a model called *shape dynamics*, which was introduced as a reformulation of general relativity in 3+1 dimensions in [58]. Its development was inspired by Dirac's work [44] on the constant mean curvature (CMC) gauge, York's method for solving the initial value problem [90, 109, 110] and Machian ideas developed by Barbour and collaborators [21, 25].

Let us outline the basic idea behind shape dynamics in $d + 1$ dimensions. In the canonical framework of general relativity, dynamics takes place in the ADM phase space Γ_{ADM}, in which a point corresponds to a pair consisting of a d-dimensional metric and its momentum density. The symmetries in the ADM formalism are given by the Hamiltonian constraints $S(x)$, which generate refoliations, and the diffeomorphism constraints
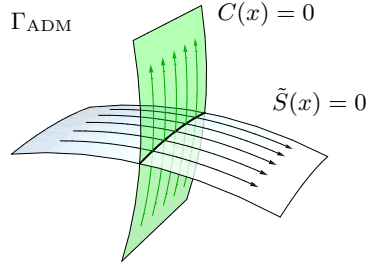
This chapter is based on [33].

Figure 7.1: *The volume-preserving conformal constraint $C(x) = 0$ as a gauge fixing for the refoliation symmetry generated by (all but one of) the Hamiltonian constraints $S(x)$.*

$H_a(x)$, which generate spatial diffeomorphisms. Space-time solutions correspond to gauge orbits within the constraint surface in phase space. A convenient way to identify the gauge orbits is by gauge fixing. To do this we consider another set of constraints for which the constraint surface intersects each of the gauge orbits exactly once. The additional constraints turn all of the original first-class constraints into second-class constraints and by solving these we end up with the reduced phase space of general relativity. A particularly useful and well-studied gauge for the Hamiltonian constraint is the so-called constant mean curvature (CMC) gauge $C(x)$. This gauge-fixes all but one of the Hamiltonian constraints $S(x)$, therefore leaving only a global time evolution. In addition to being a good gauge fixing the CMC constraint has the interesting property that it generates volume-preserving conformal transformations, which is illustrated in figure 7.1. Notice that there is an apparent duality present in figure 7.1: we can view the CMC constraints as gauge fixing for the refoliation symmetries, but just as well view the Hamiltonian constraints as gauge fixing for the conformal symmetries. This duality has been made precise in the case $d = 3$ in [58, 59] and the resulting dual theory is referred to as *shape dynamics*.[29] It is defined by a set of first-class constraints on the ADM phase space: a global Hamiltonian H_{SD}, the volume-preserving conformal constraints $C(x)$, together with the usual diffeomorphism constraints $H_a(x)$.

The explicit construction of the shape dynamics Hamiltonian, however, requires the general solution of a partial differential equation, which is equivalent to partially solving the initial value problem of general relativity using York's method. This is a serious complication, which introduces nonlocalities into the Hamiltonian and obstructs many straightforward investigations. To learn about shape dynamics it is therefore valuable to consider exactly solvable non-trivial gravitational models. This provides the main motivation for this chapter: we consider a non-trivial model in which shape dynamics

---

[29]For details and background on shape dynamics we refer to the PhD theses by Gryb [60] and Gomes [57].

can be constructed explicitly allowing us to study its generic features.

The probably best-known example of a non-trivial exactly solvable gravitational system is pure gravity on the torus in 2+1 dimensions [35, 36, 83, 85]. The technical reason for the simplifications in this model is two-fold. First, one is able to solve the initial value problem of ADM gravity explicitly on the torus. This is important for the construction of classical shape dynamics and occurs only on the torus and the 2-sphere.[30] Pure gravity on higher-genus surfaces is more intricate since we lack methods to solve the initial value problem in general. Second, the physical, reduced phase space (after solving for initial data) is finite-dimensional, which is a generic feature of pure gravity in 2+1 dimensions. This is important for quantization, because a finite-dimensional system admits generic quantum theories, while non-trivial quantum systems with infinitely many degrees of freedom are sparse.

The plan for this chapter is as follows: we start with the explicit construction of pure shape dynamics on the torus in section 7.1 and demonstrate its equivalence with general relativity using the method of linking gauge theories. The trading of refoliation invariance for local spatial conformal invariance turns all local constraints into phase space functions that are linear in the momenta, while the remaining shape dynamics Hamiltonian turns out to formally coincide with the reduced phase space Hamiltonian, which at large CMC-volume becomes the conformal constraint that changes the total volume. In section 7.2 we consider shape dynamics on a higher-genus surface, which does not admit straightforward solutions to the initial value problem. In this sense the problem of nonlocality for higher genus is closer in spirit to that encountered in higher dimensions. We attack this problem by constructing a perturbation expansion and recover a fully conformal theory in the large-volume regime. We find that at large volume the generically nonlocal Hamiltonian becomes the integral over a local density and turns again into the conformal constraint that changes the total volume. We then use the classical results to formally quantize shape dynamics on the torus in section 7.3. Due to linearity of the local constraints, one can implement them at the quantum level and thus formally quantize the analogue of the Wheeler–DeWitt equation, with infinitely many degrees of freedom. In this construction we refrain from giving a complete description of the Hilbert space, which would require to solve additional measure-theoretic problems.

---

[30]The sphere is a degenerate case, since it admits only one canonical pair of degrees of freedom (the volume and the mean extrinsic curvature). This leaves only the de Sitter solution which contains no interesting dynamics.

7.1   Equivalence of general relativity and shape dynamics

In this section we establish the equivalence between general relativity and shape dynamics on the $(2+1)$-dimensional torus universe by explicitly constructing the linking theory relating the two. For simplicity we assume a positive cosmological constant Λ. We start with the general construction of the linking theory before focusing on the torus, which allows us, other than in higher dimensions or even on a higher-genus surface, to explicitly work out shape dynamics.

Our starting point is the ADM Hamiltonian on the usual ADM phase space Γ_{ADM}, expressed in terms of the metric $g_{ab}(x)$ and its canonically conjugate momentum density $\pi^{ab}(x)$,

$$H = S(N) + H(\xi),$$
$$S(N) = \int \mathrm{d}^2 x\, N \left(\pi^{ab} \mathcal{G}_{abcd} \pi^{cd} / \sqrt{|g|} - \sqrt{|g|}\, (R - 2\Lambda) \right), \qquad (7.1)$$
$$H(\xi) = \int \mathrm{d}^2 x\, \pi^{ab} \mathcal{L}_\xi g_{ab}.$$

Here $\mathcal{G}_{abcd} = 1/2(g_{ac}g_{bd} + g_{ad}g_{bc}) - g_{ab}g_{cd}$ is the Wheeler–DeWitt supermetric we have already encountered in section 5.3, and S and H denote the ADM Hamiltonian and diffeomorphism constraints.

The central idea behind shape dynamics is to trade the local Hamiltonian ADM constraints $S(N)$, which are quadratic in momenta, for local constraints that are linear in momenta, because linear constraints admit a geometric interpretation as generators of transformations of the spatial metric. A priori there is an infinite set of such constraints possible, all of the form $T[g; x)_{ab}\pi^{ab}(x)$, where $T[g, x)_{ab}$ denotes a local symmetric tensor constructed from the metric and its derivatives. Arguably the simplest choice is $\pi(x) = g_{ab}(x)\pi^{ab}(x)$, the generator of spatial conformal transformations. However, we do not want to trade all Hamiltonian constraints, but rather seek to retain one combination of the ADM Hamiltonian constraints to generate classical dynamics. The simplest choice to achieve this is to restrict oneself to those conformal transformations that preserve the total spatial volume generated by $\pi(x) - \langle \pi \rangle_g \sqrt{|g|}(x)$. This choice has the surprising feature that one can prove that symmetry trading is always possible, because the volume-preserving conformal transformations turn out to generate York scaling.[31] We do not know of any other generator that can be shown to always allow for symmetry trading, but we also lack a uniqueness proof.

---

[31] By York scaling we mean that the transverse parts of π^{ab} and π scale with opposite conformal weights, which is important for having a unique solution to the Lichnerowicz–York equation appearing in York's method for solving the initial value problem.

To perform this trading of symmetries we construct a linking theory following the "best matching procedure" outlined in [24]. To best match with respect to conformal transformations that preserve the total volume we consider the ADM phase space as a subspace of a larger phase space $\Gamma_{ext} = \Gamma_{ADM} \times \Gamma_\phi$, where Γ_ϕ is the phase space of a scalar field $\phi(x)$, whose canonically conjugate momentum density is denoted by $\pi_\phi(x)$. The phase space functions on Γ_{ADM} are naturally identified with those phase space functions on Γ_{ext} that are independent of (ϕ, π_ϕ). We can thus recover usual ADM gravity in this larger system by introducing an additional first-class constraint

$$Q(x) := \pi_\phi(x) \approx 0 \tag{7.2}$$

and add it smeared with a Lagrange multiplier $\rho(x)$ to the ADM Hamiltonian, which is now $H = S(N) + H(\xi) + Q(\rho)$. Let us now consider a canonical transformation from $(g_{ab}, \pi^{ab}, \phi, \pi_\phi)$ to $(G_{ab}, \Pi^{ab}, \Phi, \Pi_\phi)$ generated by the generating functional

$$F = \int d^2x \left(g_{ab}(x) e^{2\hat{\phi}(x)} \Pi^{ab}(x) + \phi(x) \Pi_\phi(x) \right). \tag{7.3}$$

Here $\hat{\phi}$ is defined in terms of ϕ by subtracting a spatial average, which has a non-trivial dependence on the metric,

$$\hat{\phi}(x) := \phi(x) - \frac{1}{2} \ln \left\langle e^{2\phi} \right\rangle_g, \tag{7.4}$$

where we use the shorthands $\langle f \rangle_g = V_g^{-1} \int d^2x \sqrt{|g|} f$ and $V_g = \int d^2x \sqrt{|g|}$. Notice that we constructed $\hat{\phi}$ such that the conformal factor $e^{2\hat{\phi}}$ preserves the total volume. The canonical transformation of the elementary variables, which is generated by (7.3), can be worked out explicitly,

$$
\begin{array}{rcl}
g_{ab}(x) \rightarrow G_{ab}(x) &=& e^{2\hat{\phi}(x)} g_{ab}(x), \\
\pi^{ab}(x) \rightarrow \Pi^{ab}(x) &=& e^{-2\hat{\phi}(x)} \left(\pi^{ab}(x) - \frac{1}{2} \sqrt{|g|}(x) g^{ab}(x) \langle \pi \rangle \left(1 - e^{2\hat{\phi}(x)} \right) \right), \\
\phi(x) \rightarrow \Phi(x) &=& \phi(x), \\
\pi_\phi(x) \rightarrow \Pi_\phi(x) &=& \pi_\phi(x) - 2 \left(\pi(x) - \langle \pi \rangle \sqrt{|g|}(x) \right),
\end{array}
\tag{7.5}
$$

using shorthand notation $\pi(x) = \pi^{ab}(x) g_{ab}(x)$ and $\langle \pi \rangle = V^{-1} \int d^2x \, \pi(x)$. This transformation leads us to the constraints of the linking theory,

$$
\begin{array}{rcl}
H &=& S(N) + H(\xi) + Q(\rho), \\
S(N) &=& \int d^2x N \left[\frac{e^{-2\hat{\phi}}}{\sqrt{|g|}} \left(\pi^{ab} \mathcal{G}_{abcd} \pi^{cd} - \frac{1}{2} \left(\pi - \langle \pi \rangle (1 - e^{6\hat{\phi}}) \sqrt{|g|} \right)^2 + \frac{1}{2} \pi^2 \right) \right. \\
&& \left. - \sqrt{|g|} \left(R[g] - 2\Delta\hat{\phi} - 2\Lambda e^{2\hat{\phi}} \right) \right], \\
H(\xi) &=& \int d^2x \, e^{-2\hat{\phi}} \left(\pi^{ab} - \frac{1}{2} \sqrt{|g|} g^{ab} \langle \pi \rangle \left(1 - e^{2\hat{\phi}} \right) \right) \left(\mathcal{L}_\xi e^{2\hat{\phi}} g \right)_{ab}(x), \\
Q(\rho) &=& \int d^2x \, \rho(x) \left(\pi_\phi(x) - 2 \left(\pi(x) - \langle \pi \rangle \sqrt{|g|}(x) \right) \right),
\end{array}
\tag{7.6}
$$

where $S(N)$, $H(\xi)$ and $Q(\rho)$ are obtained by applying (7.5) to (7.1) and (7.2). One can check that after integrating by parts and using $Q = 0$ the constraint $H(\xi)$ turns into the usual form of the diffeomorphism constraint $H(\xi) = \int \mathrm{d}^2x \left(\pi^{ab} \mathcal{L}_\xi g_{ab} + \pi_\phi \mathcal{L}_\xi \phi \right)$. We will use this form of the constraint below. The linking theory thus contains the usual diffeomorphism constraint, a conformal constraint that preserves the total 2-volume and a Hamiltonian constraint that arises as a modification of the ADM refoliation constraint.

7.1.1 Linking theory on the torus

We will now exploit some properties of two-dimensional metrics on the torus, which we already encountered in previous chapters, to simplify the constraints (7.6). We will follow [35, 36] where possible. First of all, recall that all metrics on the torus are conformally flat. The space of flat metrics modulo diffeomorphisms is finite-dimensional and admits a convenient parametrization by the Teichmüller parameters τ_1 and τ_2.

To make this more explicit let us fix a global chart on the torus, which allows us to uniquely identify any point with its coordinates $(x^1, x^2) \in [0,1)^2$. In these coordinates we can decompose an arbitrary metric g_{ab} as

$$g_{ab}(x) = e^{2\lambda(x)} \left(f^* \bar{g} \right)_{ab} (x), \tag{7.7}$$

where λ is a conformal factor, f a small diffeomorphism, i.e. a diffeomorphism continuously connected to the identity, and $\bar{g}$ a flat reference metric. We can make this decomposition unique by requiring $\bar{g}$ to be of the form

$$\bar{g}_{ab} = \frac{1}{\tau_2} \begin{pmatrix} 1 & \tau_1 \\ \tau_2 & \tau_1^2 + \tau_2^2 \end{pmatrix}, \tag{7.8}$$

where $\tau = \tau_1 + i\tau_2$ denote the Teichmüller parameters (as in sections 3.1 and 4.3). There is a slight redundancy left in the decomposition having to do with the fact that f is only determined up to an isometry of $\bar{g}$, i.e. up to translations in x^1 and x^2. If we require f to leave $(0,0)$ invariant, we obtain a one-to-one map between metrics on the torus and the data (λ, f, τ).

We can explicitly decompose the momentum density[32]

$$\pi^{ab} = e^{-2\lambda} \left(p^{ab} + \frac{1}{2} \pi \bar{g}^{ab} + \sqrt{|\bar{g}|} \left(\bar{D}^a Y^b + \bar{D}^b Y^a - \bar{g}^{ab} \bar{D}_c Y^c \right) \right), \tag{7.9}$$

---

[32]All indices here are raised with the reference metric $\bar{g}$, and $\bar{D}$ denotes the covariant derivative with respect to $\bar{g}$.

in terms of a trace π, a vector field Y and a transverse traceless tensor density (w.r.t. $\bar{g}$), which we can explicitly parametrize by

$$p^{ab} = \frac{1}{2} \begin{pmatrix} (\tau_1^2 - \tau_2^2)p_2 - 2\tau_1\tau_2 p_1 & \tau_2 p_1 - \tau_1 p_2 \\ \tau_2 p_1 - \tau_1 p_2 & p_2 \end{pmatrix}. \tag{7.10}$$

This decomposition is such that π is conjugate to 2λ and p_i is conjugate to τ_i.

Writing the linking theory constraints (7.6) in terms of λ, f, τ, π, Y and p we get

$$
\begin{aligned}
S(N) &= \int \mathrm{d}^2 x N \left[\frac{e^{-2(\hat{\phi}+\lambda)}}{\sqrt{|\bar{g}|}} \left((p^{ab} + (PY^{ab})\sqrt{|\bar{g}|})\bar{g}_{ac}\bar{g}_{bd}(p^{cd} + (PY^{cd})\sqrt{|\bar{g}|}) \right. \right. \\
&\quad \left. \left. - \tfrac{1}{2}(\pi - \langle\pi\rangle\sqrt{|\bar{g}|}(1 - e^{2(\hat{\phi}+\lambda)}))^2 \right) + \sqrt{|\bar{g}|} \left(2\bar{\Delta}(\hat{\phi} + \lambda) + 2\Lambda e^{2(\hat{\phi}+\lambda)} \right) \right] \\
H(\xi) &= \int \mathrm{d}^2 x \xi^a \left(\sqrt{|\bar{g}|}\bar{\Delta}Y_a + \tfrac{1}{2}e^{2\lambda}\bar{D}_a(e^{-2\lambda}\pi) + \pi_\phi \phi_{,a} \right) \\
Q(\rho) &= \int \mathrm{d}^2 x \rho(x) \left(\pi_\phi(x) - 2 \left(\pi(x) - \langle\pi\rangle\sqrt{|\bar{g}|}(x)e^{2\lambda(x)} \right) \right),
\end{aligned}
\tag{7.11}
$$

where we used the shorthand $PY_{ab} = \bar{D}_a Y_b + \bar{D}_b Y_a - \bar{g}_{ab}\bar{g}^{cd}\bar{D}_c Y_d$.

To complete the definition of a linking theory, we specify two sets of gauge-fixing conditions,

$$\phi(x) = 0 \quad \text{for GR and} \quad \pi_\phi(x) = 0 \quad \text{for SD}, \tag{7.12}$$

which we will now use to reconstruct general relativity and shape dynamics respectively.

7.1.2 Recovering general relativity

To recover standard ADM gravity on the torus let us impose the gauge-fixing condition $\phi(x) = 0$ to the linking theory. To perform the phase space reduction from the extended phase space to the ADM phase space, we need to fix the Lagrange multipliers such that the gauge-fixing is propagated. Since the momentum density π_ϕ occurs only in the constraints Q, we have to solve

$$0 = \{Q(\rho), \phi(x)\} = \rho(x) \tag{7.13}$$

for the Lagrange multiplier ρ, which implies $\rho = 0$. The constraints $Q(x)$ are gauge-fixed and drop out of the Hamiltonian, which becomes independent of π_ϕ. Hence, one can perform the phase space reduction by setting $\phi \equiv 0$, $\rho \equiv 0$ and π_ϕ arbitrary[33] in (7.6). The Hamiltonian on the ADM phase space thus reads

$$H = S(N) + H(\xi), \tag{7.14}$$

---

[33]Had the constraints $Q(\rho)$ not dropped out after gauge fixing ρ, we would have had to solve $Q \equiv 0$ for π_ϕ to complete the phase space reduction.

where $S(N)$ and $H(\xi)$ are precisely the Hamiltonian and diffeomorphism constraint of general relativity in the ADM formulation as given in (7.1). We note that we explicitly retained refoliation invariance.

7.1.3 Recovering shape dynamics

To recover shape dynamics we employ the gauge-fixing condition $\pi_\phi(x) = 0$. We will see that the decomposed form (7.11) of the constraints allows us to find the explicit shape dynamics Hamiltonian through a phase space reduction $(\phi, \pi_\phi) \rightarrow (\phi_0, 0)$. To find this map we can use $\pi_\phi \equiv 0$, so the Q constraints become

$$Q(\rho) = \int d^2x \rho(x) \left(\pi(x) - \langle \pi \rangle \sqrt{|g|(x)} \right), \tag{7.15}$$

which implies that $\pi(x)$ is a covariant constant. Using this and $\pi_\phi = 0$, we find that the diffeomorphism constraint implies that

$$PY_{ab}(x) = 0, \tag{7.16}$$

which implies that the Hamiltonian constraint is independent of $Y_a(x)$. With these simplifications and plugging in the explicit representations (7.8) and (7.10), we find

$$S(N) = \int d^2x \sqrt{|\bar{g}|} N \left(e^{-2(\hat{\phi}+\lambda)} \frac{\tau_2^2}{2}(p_1^2 + p_2^2) - \frac{e^{2(\hat{\phi}+\lambda)}}{2}(\langle\pi\rangle^2 - 4\Lambda) + 2\bar{\Delta}(\hat{\phi}+\lambda) \right). \tag{7.17}$$

We see that the constraints $S(N)$ would be solved if we were able to choose

$$e^{4(\hat{\phi}+\lambda)} = \frac{\tau_2^2(p_1^2 + p_2^2)}{\langle\pi\rangle^2 - 4\Lambda}. \tag{7.18}$$

However, this is in general obstructed by the volume-preservation condition

$$\int d^2x \sqrt{|\bar{g}|} e^{2(\hat{\phi}+\lambda)} = V. \tag{7.19}$$

This means that the constraints generating the refoliations are not completely gauge-fixed by the condition $\pi_\phi(x) = 0$. It turns out that among the infinitely many constraints $S(N)$ one remains first class, which after phase space reduction becomes the shape dynamics Hamiltonian H_{SD}. More concretely, there exists a lapse N_0 such that $S(N_0)$ Poisson-commutes with π_ϕ, and satisfies the lapse-fixing equation

$$\{S(N_0), \pi_\phi(x)\} = F_{N_0}(x) - e^{2(\hat{\phi}+\lambda)}\sqrt{|\bar{g}|}\langle F_{N_0}\rangle = 0,$$
$$\text{where } F_N = N\left(-e^{-2(\hat{\phi}+\lambda)}\tau_2^2(p_1^2 + p_2^2) - |\bar{g}|e^{2(\hat{\phi}+\lambda)}(\langle\pi\rangle^2 - 4\Lambda)\right) + \sqrt{|\bar{g}|}\bar{\Delta}N. \tag{7.20}$$

If one imposes on N_0 a normalization condition $\int \mathrm{d}^2x \sqrt{|\bar{g}|} e^{2(\hat{\phi}+\lambda)} N_0 = V$, (7.20) has a unique solution. We want to project out this first-class part $S(N_0)$ from the full set of constraints $S(x)$ to end up with a purely second-class set of constraints $\widetilde{S}(x)$ that we can solve. We can perform the projection in different ways, but a particularly convenient way of doing this is by defining

$$\widetilde{S}(x) := S(x) - \frac{S(N_0)}{V}\sqrt{|\bar{g}|(x)} e^{2(\hat{\phi}(x)+\lambda(x))}, \tag{7.21}$$

which automatically satisfies $\widetilde{S}(N_0) = 0$. Identifying $H_{\mathrm{SD}} = S(N_0)$, we arrive at the modified Lichnerowicz–York equations

$$0 = \widetilde{S}(x) = \sqrt{|\bar{g}|}\left(e^{-2(\hat{\phi}+\lambda)}\frac{\tau_2^2(p_1^2 + p_2^2)}{2} \right.$$
$$\left. - e^{2(\hat{\phi}+\lambda)}\frac{\langle\pi\rangle^2 - 4\Lambda + 2\frac{H_{\mathrm{SD}}}{V}}{2} - 2\bar{\Delta}(\hat{\phi}+\lambda) \right), \tag{7.22}$$
$$V = \int \mathrm{d}^2x \sqrt{|\bar{g}|} e^{2(\hat{\phi}+\lambda)},$$

which we need to solve for $\hat{\phi}$ and H_{SD}. A solution is found by taking $\hat{\phi}+\lambda$ to be spatially constant. More precisely, from the second equation it follows that

$$\hat{\phi} = -\lambda + \frac{1}{2}\ln V. \tag{7.23}$$

Now H_{SD} can be easily determined from the first equation in (7.22),

$$H_{\mathrm{SD}} = \frac{\tau_2^2}{2V}(p_1^2 + p_2^2) - \frac{V}{2}\left(\langle\pi\rangle^2 - 4\Lambda\right). \tag{7.24}$$

Notice that to find $H_{\mathrm{SD}} = S(N_0)$ we did not have to solve the lapse-fixing equation explicitly. In this case we can solve (7.20) straightforwardly using the fact that $\hat{\phi}+\lambda$ is constant. The result is simply $N_0 = 1$. In general, however, the lapse-fixing equation is quite complicated and we are lucky that we do not have to solve it to derive the shape dynamics Hamiltonian (as we will again see in section 7.2). As a constraint $\widetilde{S} = 0$ is completely equivalent to

$$S(x) - \langle S\rangle \sqrt{|\bar{g}|(x)} e^{2(\hat{\phi}(x)+\lambda(x))} = 0, \tag{7.25}$$

which does not refer to a lapse at all.

The shape dynamics Hamiltonian H_{SD} (7.24) is exactly the reduced phase space Hamiltonian constraint. The more familiar Hamiltonian H_{York} generating evolution in

York time $\langle\pi\rangle$ (see e.g. [35] section 3.3) is obtained by noting that the variable canonically conjugate to $\langle\pi\rangle$ is V. Therefore, by solving $H_{\text{SD}} = 0$, we obtain

$$H_{\text{York}} = V = \tau_2 \frac{\sqrt{p_1^2 + p_2^2}}{\sqrt{\langle\pi\rangle^2 - 4\Lambda}}. \tag{7.26}$$

We can now perform explicitly the phase space reduction of the linking theory and describe shape dynamics on the ADM phase space through its total Hamiltonian and first-class constraints

$$
\begin{aligned}
H &= \mathcal{N} H_{\text{SD}} + H(\xi) + C(\rho) \\
H_{\text{SD}} &= \frac{\tau_2^2}{2V}(p_1^2 + p_2^2) - \frac{V}{2}\left(\langle\pi\rangle^2 - 4\Lambda\right) \\
H(\xi) &= \int \mathrm{d}^2x\, \pi^{ab} \mathcal{L}_\xi g_{ab} \\
C(\rho) &= \int \mathrm{d}^2x\, \rho\left(\pi - \langle\pi\rangle\sqrt{|g|}\right).
\end{aligned}
\tag{7.27}
$$

The gauge symmetries are spatial diffeomorphisms, conformal transformations that preserve the total volume and global time reparametrizations. Despite the different set of symmetries, the equivalence with standard general relativity is obvious: the shape dynamics Hamiltonian coincides on the reduced phase phase with the CMC Hamiltonian, while the constraints C provide the CMC gauge-fixing conditions.

Although we know the shape dynamics Hamiltonian explicitly on the torus, it is instructive to observe that the shape dynamics Hamiltonian constraint H can be expanded in powers of the inverse volume, because it exhibits two properties that we can investigate in more complicated models. This expansion is a systematic approximation to shape dynamics that is a good approximation in an asymptotic large-volume regime, where $V \to \infty$ while keeping the other degrees of freedom finite. In this regime we find two important features of shape dynamics:

1. **Asymptotic Locality:** The leading order of the Hamiltonian, which becomes exact in the limit $V \to \infty$, is $\langle\pi\rangle^2 - 4\Lambda + \mathcal{O}(V^{-2}) \approx 0$. As a constraint, this is equivalent to

$$V\left(\langle\pi\rangle - 2\sqrt{\Lambda}\right) = \int \mathrm{d}^2x\left(\pi(x) - 2\sqrt{\Lambda}\sqrt{|g|}(x)\right) \approx 0 \quad \text{for } V \to \infty, \tag{7.28}$$

   which is diffeomorphism-invariant as the integral over a *local* density and by inspection invariant under conformal transformations that preserve the total volume.

2. **Full Conformal Invariance:** Since the shape dynamics Hamiltonian constraint is asymptotically equivalent to $\langle\pi\rangle - const. \approx 0$, we can add it to the conformal

constraints C to obtain in the large-volume limit $C(x) + H_{\mathrm{SD}} = \pi(x) - const. \approx 0$, which generates full conformal transformations, i.e., including those that change the total spatial volume. This requires us to interpret the shape dynamics Hamiltonian as a constraint, rather than a generator of physical dynamics.

Let us have a quick look at the 2-sphere. The linking theory and phase space reduction can be performed following the same steps as on the torus with two small modifications. Firstly, there are no Teichmüller parameters on the sphere, so there is only one canonical pair of physical degrees of freedom (V and $\langle \pi \rangle$). Secondly, the total spatial curvature does not vanish, but is equal to 8π. Shape dynamics on the sphere thus takes the form of (7.27), except for the Hamiltonian, which is $H_{\mathrm{SD}} = -\frac{V}{2}(\langle \pi \rangle^2 - 4\Lambda) - 8\pi$.

7.2 Higher-genus surfaces

On a higher-genus surface, we can still use the decomposition analogous to (7.7) and (7.9), but the explicit construction of the shape dynamics Hamiltonian constraint on the torus rested on the explicit solvability of the modified Lichnerowicz–York equation (7.22). The Lichnerowicz–York equation on a higher-genus surface (or in higher dimensions) is not explicitly solvable. We thus restrict our construction of shape dynamics to an approximation scheme and consider an expansion that becomes exact in the large-volume limit.[34] Again, we follow [35, 36] when possible.

In genus $g \geq 2$ we can perform a decomposition analogous to (7.7) and (7.9),

$$
\begin{aligned}
g_{ab}(x) &= e^{2\lambda(x)}(f^*\bar{g})_{ab}(x), \\
\pi^{ab}(x) &= e^{-2\lambda}\left(p^{ab}(x) + \tfrac{1}{2}\bar{g}^{ab}(x)\pi(x) + \sqrt{|\bar{g}|}(x)\bar{g}^{ab}(x)\bar{g}^{cd}(x)PY_{cd}(x)\right),
\end{aligned} \tag{7.29}
$$

where now we take the reference metric $\bar{g}$ to be of unit volume $\int \mathrm{d}^2x \sqrt{|\bar{g}|} = 1$ and constant scalar curvature $\bar{R}$. According to the Gauss–Bonnet theorem, $\bar{R}$ is given by

$$
\bar{R} = -8\pi(g-1). \tag{7.30}
$$

Modulo diffeomorphisms the space of such metrics corresponds to the genus-g Teichmüller space, which has dimension $6g - 6$. No simple explicit parametrization for $\bar{g}$ is known, so we will keep the parametrization implicit.

We can again write the linking theory using the decomposition (7.29). The only difference compared to the constraints (7.11) for the torus is the subtraction from $S(N)$ of a spatial curvature term.

---

[34]See [23] for an analogous expansion.

When we impose the gauge fixing $\pi_\phi = 0$, we obtain the analogue of (7.17),

$$S(N) = \int d^2x \sqrt{|\bar{g}|} N \left(e^{-2(\hat{\phi}+\lambda)} \frac{\bar{g}_{ac}\bar{g}_{bd}p^{ab}p^{cd}}{|\bar{g}|} - e^{2(\hat{\phi}+\lambda)} \frac{\langle\pi\rangle^2 - 4\Lambda}{2} + 2\bar{\Delta}(\hat{\phi}+\lambda) - \bar{R} \right). \quad (7.31)$$

Reusing our discussion for the torus, we construct the second-class part $\widetilde{S}$ of S according to (7.25),

$$\widetilde{S}(x) = S(x) - \langle S \rangle \sqrt{|\bar{g}|(x)} e^{2(\hat{\phi}(x)+\lambda(x))}. \quad (7.32)$$

Identifying the remaining first-class constraint $\langle S \rangle$ with H_{SD}/V, we obtain the modified Lichnerowicz–York equations for genus $g \geq 2$,

$$\begin{aligned}
0 = \widetilde{S}(x) = \sqrt{|\bar{g}|} \Big(& e^{-2(\hat{\phi}+\lambda)} \frac{\bar{g}_{ac}\bar{g}_{bd}p^{ab}p^{cd}}{|\bar{g}|} \\
& - e^{2(\hat{\phi}+\lambda)} \frac{\langle\pi\rangle^2 - 4\Lambda + 2\frac{H_{\text{SD}}}{V}}{2} + 2\bar{\Delta}(\hat{\phi}+\lambda) - \bar{R} \Big),
\end{aligned} \quad (7.33)$$

$$V = \int d^2x \sqrt{|\bar{g}|} e^{2(\hat{\phi}+\lambda)}.$$

To simplify the notation let us define $\mu = \hat{\phi} + \lambda - \frac{1}{2}\ln V$ and $p^2 := \frac{\bar{g}_{ac}\bar{g}_{bd}p^{ab}p^{cd}}{|\bar{g}|}$. Then (7.33) can be written as

$$\frac{1}{V}p^2 e^{-2\mu} - \frac{1}{2}V \left(\langle\pi\rangle^2 - 4\Lambda + \frac{2H_{\text{SD}}}{V} \right) e^{2\mu} + 2\bar{\Delta}\mu - \bar{R} = 0 \quad \text{and} \quad \langle e^{2\mu} \rangle_{\bar{g}} = 1. \quad (7.34)$$

In the following we will drop the subscript $\bar{g}$ and keep in mind that averages $\langle \cdot \rangle$ are taken with respect to $\bar{g}$ (except for $\langle \pi \rangle$).

Equation (7.34) is nearly identical to the standard Lichnerowicz–York equation in 2+1 dimensions. The only difference is that we have a restriction on μ. To compensate for this we have an additional constant H_{SD} to solve for. The existence of a unique solution for μ and H_{SD} (as a function of $\bar{g}_{ab}$, p^{ab}, V and $\langle \pi \rangle$) is a direct consequence of the existence and uniqueness properties of the usual Lichnerowicz–York equation.

The key simplification that allowed us to explicitly construct shape dynamics on the torus is that there one can choose the constant-curvature metric $\bar{g}_{ab}$ such that p^2 is spatially constant. For genus 2 and higher the Lichnerowicz–York equation is much harder to solve. However, we can already deduce some properties of H_{SD} by integrating expression (7.34),

$$H_{\text{SD}} = -\frac{V}{2}(\langle\pi\rangle^2 - 4\Lambda) - \bar{R} + \frac{1}{V}\langle p^2 e^{-2\mu} \rangle. \quad (7.35)$$

We have chosen our second-class constraints (7.32) in such a way that the solution μ will not depend on $\langle \pi \rangle$ (or Λ), and therefore the same holds for the last term in (7.35). Hence, our choice is special in that it produces a Hamiltonian quadratic in the momentum $\langle \pi \rangle$ conjugate to V.

7.2.1 Large-volume expansion

Although we cannot solve (7.34) explicitly, the modified Lichnerowicz–York equation does allow for an interesting perturbative expansion. Notice that the volume V appears explicitly in (7.34) and should be treated as a parameter when solving the equation. Therefore we can try to find solutions μ and H_{SD} expanded in powers of $1/V$ and construct the shape dynamics in the infinite-volume limit.[35] To do this we make the ansatz

$$e^{2\mu} = \sum_{k=0}^{\infty} \Omega_k V^{-k} \quad \text{and} \quad H_{\text{SD}} = \sum_{k=-1}^{\infty} H_k V^{-k}. \tag{7.36}$$

Looking carefully at (7.34) it follows that higher powers of V cannot occur. From the normalization $\langle e^{2\mu} \rangle = 1$ we get the restrictions $\langle \Omega_0 \rangle = 1$ and $\langle \Omega_k \rangle = 0$ for $k > 0$.

The leading order of (7.34) is proportional to V and fixes $H_{-1} = -\frac{1}{2}(\langle \pi \rangle^2 - 4\Lambda)$. At order V^0 the equation then reads

$$-\Omega_0 H_0 - \bar{R} + 2\bar{\Delta} \ln(\Omega_0) = 0, \tag{7.37}$$

which is clearly solved by $H_0 = -\bar{R}$ and $\Omega_0 = 1$. The Lichnerowicz–York equation now becomes

$$\frac{1}{V} \frac{1}{1 + \sum_k \frac{\Omega_k}{V^k}} p^2 - \left(1 + \sum_k \frac{\Omega_k}{V^k}\right)\left(-\bar{R} + \sum_k \frac{H_k}{V^k}\right) - \bar{R} + \bar{\Delta} \ln\left(1 + \sum_k \frac{\Omega_k}{V^k}\right) = 0. \tag{7.38}$$

If we define the polynomials A_k and B_k as functions of Ω_1 to Ω_k by[36]

$$\frac{1}{1 + \sum_k \frac{\Omega_k}{V^k}} = \sum_k \frac{A_k[\Omega]}{V^k} \quad \text{and} \quad \ln(1 + \sum_k \frac{\Omega_k}{V^k}) - \sum_k \frac{\Omega_k}{V^k} = \frac{1}{V} \sum_k \frac{B_k[\Omega]}{V^k}, \tag{7.39}$$

from (7.35) or from integrating (7.38) it follows that for $k \geq 1$

$$H_k = \left\langle p^2 A_{k-1}[\Omega] \right\rangle. \tag{7.40}$$

The order-V^{-k} equation in (7.38) then allows us to solve Ω_k recursively in terms of the $\Omega_i, 1 \leq i < k$, as

$$\Omega_k = (\bar{\Delta} + \bar{R})^{-1} \left(-A_{k-1}[\Omega] p^2 - \bar{\Delta} B_{k-1}[\Omega] + \sum_{l=1}^{k} H_l \Omega_{k-l}\right), \tag{7.41}$$

---

[35]This cannot be done easily in the reduced phase space approach, in which also the volume itself has to be solved for in terms of $\bar{g}$ and the momenta.

[36]The first few polynomials are $A_0 = 1$, $A_1 = -\Omega_1$, $A_2 = -\Omega_2 + \Omega_1^2$, $A_3 = -\Omega_3 + 2\Omega_1\Omega_2 - \Omega_1^3$ and $B_0 = 0$, $B_1 = -\Omega_1^2/2$, $B_2 = \Omega_1^3/3 - \Omega_1\Omega_2$.

where the operator $\bar{\Delta} + \bar{R}$ is negative definite and therefore has a well-defined inverse.

In this way, we have obtained a general algorithm to solve the modified Lichnero-wicz–York equation order by order through the recurrence relation (7.41) together with (7.40). We have calculated the first few H_k explicitly, leading to a Hamiltonian

$$
\begin{aligned}
H_{\text{SD}} = &-\frac{V}{2}(\langle\pi\rangle^2 - 4\Lambda) - \bar{R} + \frac{1}{V}\langle p^2\rangle \\
&+ \frac{1}{V^2}\Big\langle (p^2 - \langle p^2\rangle)(\bar{\Delta} + \bar{R})^{-1}(p^2 - \langle p^2\rangle)\Big\rangle \\
&+ \frac{1}{2V^3}\Big[\bar{R}\Big\langle\Big((\bar{\Delta} + \bar{R})^{-1}(p^2 - \langle p^2\rangle)\Big)^3\Big\rangle \\
&\qquad + 3\Big\langle (p^2 + \langle p^2\rangle)\Big((\bar{\Delta} + \bar{R})^{-1}(p^2 - \langle p^2\rangle)\Big)^2\Big\rangle\Big] + \cdots.
\end{aligned}
\tag{7.42}
$$

In general H_k will be a function homogeneous in p^2 of order k.[37]

The expansion has features similar to a tree-level (Feynman diagram) expansion with propagator $(\bar{\Delta} + \bar{R})^{-1}$ and source term p^2/V. To make this connection more explicit, let us view the modified Lichnerowicz–York equation (7.34) as the Euler–Lagrange equation of some action S_{LY}. Such an action can be easily constructed,

$$
S_{LY}[\mu, H] = \int \mathrm{d}^2x\sqrt{\bar{g}}\left(\mu\bar{\Delta}\mu - \bar{R}\mu - \left(H - \frac{\bar{R}}{2}\right)\left(e^{2\mu} - 1\right) - \frac{1}{2}\frac{e^{-2\mu}}{V}p^2\right),
\tag{7.43}
$$

where μ is now viewed as an unrestricted function since the Lagrange multiplier

$$
H = \frac{1}{2}\left(H_{\text{SD}} + \frac{V}{2}(\langle\pi\rangle^2 - 4\Lambda) + \bar{R}\right)
\tag{7.44}
$$

enforces the constraint $\langle e^{2\mu}\rangle = 1$ on variation. We can rewrite (7.43) by singling out the quadratic part in μ and H,

$$
\begin{aligned}
S_{LY}[\mu, H] = \int \mathrm{d}^2x\sqrt{\bar{g}}\Big(&\mu(\bar{\Delta} + \bar{R})\mu - 2\mu H + \bar{R}(\frac{2}{3}\mu^3 + \frac{1}{3}\mu^4 + \ldots) \\
&- H(2\mu^2 + \ldots) - \frac{1}{2}\frac{e^{-2\mu}}{V}p^2\Big).
\end{aligned}
\tag{7.45}
$$

The Feynman rules can be read off and we can find H (and therefore H_{SD}) by computing its tree-level one-point function. Notice that the action (7.43) which we use to derive the Hamiltonian is similar to that of two-dimensional Liouville gravity [56]. More precisely,

---

[37] As the H_k are functions on the cotangent bundle to Teichmüller space, one might ask how natural they are from the perspective of Teichmüller spaces. As a partial answer we notice that $H_1 = \langle p^2\rangle$ is related to the canonical Weil–Petersson metric [100, 107], while H_2 is closely related to its curvature [108].

it is of the form of a Liouville action plus a perturbation given by a source term proportional to p^2/V.

Two remarks are in order. Firstly, we observe from (7.35) that in the limit $V \to \infty$ the shape dynamics Hamiltonian again approaches a form that is equivalent to (7.28). The Hamiltonian is thus asymptotically local and provides the volume-changing generator of conformal transformations, so full conformal invariance is asymptotically attained. Secondly, the first three terms in the large-volume expansion (7.42) sum up to an expression equivalent to the temporal gauge Hamiltonian $S(N \equiv 1)$, which is *local*.

7.3 Dirac quantization in metric variables

To expose the difference between shape dynamics and general relativity, we consider the Dirac quantization of pure gravity on the torus in 2+1 dimensions in metric variables, usually referred to as Wheeler–DeWitt quantization. For the sake of completeness we first follow [35] and revisit the problems associated with the nonlocality arising from the solution of the diffeomorphism constraint in the Wheeler–DeWitt approach. Subsequently we show how these problems are solved by trading local Hamiltonian constraints for local conformal constraints, which allows us to perform a Dirac quantization program for shape dynamics.

7.3.1 Dirac quantization of general relativity on the torus

Contrary to first-order variables, one cannot readily quantize general relativity in metric variables even in 2+1 dimensions on the torus and sphere. The reason is explained well in [35], which we follow here. Using the standard decomposition of the metric and momenta, we can solve the diffeomorphism constraints for the transverse part of the momenta according to

$$\bar{Y}_i = -\frac{1}{2}\left(\bar{\Delta} + \frac{k}{2}\right)^{-1}\left(e^{2\lambda}\bar{\nabla}_i\left(e^{-2\lambda}\pi\right)\right), \tag{7.46}$$

where $k = 0$ for the torus. To perform a Wheeler–DeWitt quantization, reference [35] chooses a polarization for which the configuration operators are given by functionals of the spatial metric and formally considers a Schrödinger representation on wave functions $\psi[f, \lambda; \tau]$, which reduces to $\psi[\lambda; \tau]$. Assuming that the inner product is constructed from a divergence-free measure, we can quantize the momenta by replacing $\pi \to -\frac{i}{2}\frac{\delta}{\delta\lambda}$ and $p^{ab} \to -i\frac{\partial}{\partial\hat{g}_{ab}}$. The diffeomorphism constraint on the torus still acts non-trivially on

the conformal factor, and its solution can be quantized as

$$\bar{Y}_i[\hat{\pi}] = \frac{i}{4}\bar{\Delta}^{-1}\left(e^{2\lambda}\bar{\nabla}_i\left(e^{-2\lambda}\frac{\delta}{\delta\lambda}\right)\right).\tag{7.47}$$

This expression is plugged into the Hamiltonian and leads to nonlocal terms in the Wheeler–DeWitt equation that are not practically manageable and lead to notorious difficulties in the Wheeler–DeWitt approach [34].

7.3.2 Dirac quantization of shape dynamics on the torus

We now follow essentially the same strategy as in the previous subsection but for shape dynamics. We choose a polarization where functionals of the metric are configuration variables and formally consider a Schrödinger representation on functionals $\psi[\lambda, f; \tau]$, such that functionals of the metric are represented by multiplication operators. We would like to specify a Hilbert space by defining it as the space of square-integrable functionals with respect to a measure $D\lambda\, Df\, d^2\tau$, but it is difficult to construct an explicit measure Df on the diffeomorphism group, such that the Hilbert space is separable and supports the diffeomorphism generators as essentially self-adjoint operators. We will thus refrain from such a construction and rather *assume* that there exists a measure Df such that the operators $U_{f_0}\psi[\lambda, f; \tau] := \psi[f_0^*\lambda, f_0 \circ f; \tau]$ are unitary. We will also assume that there is a measure $D\lambda$ such that $i\int d^2x \rho(x)\frac{\delta}{\delta\lambda(x)}$ extends to an essentially self-adjoint operator for all smooth smearing functions $\rho(x)$.

We seek a representation of the local constraints of shape dynamics, whose non-vanishing Poisson brackets are:

$$\{H(\xi), C(\rho)\} = C(\mathcal{L}_\xi \rho) \quad \text{and} \quad \{H(\xi_1), H(\xi_2)\} = H([\xi_1, \xi_2]).\tag{7.48}$$

We start with the local conformal constraint $\pi(x) - \frac{\sqrt{|\bar{g}|}e^{2\lambda(x)}}{V}\int d^2y\,\pi(y) = 0$, which, taking into account the aforementioned assumptions about the measure $D\lambda\, Df\, d^2\tau$, can be readily quantized as

$$-\frac{i}{2}\left(\frac{\delta}{\delta\lambda(x)} - \frac{\sqrt{|\bar{g}|}e^{2\lambda(x)}}{V}\int d^2y\,\frac{\delta}{\delta\lambda(y)}\right)\psi[\lambda, f; \tau] = 0,\tag{7.49}$$

working in a chart where the components of $\bar{g}_{ab}$ are constant. The solution to this constraint is that ψ depends only on the homogeneous mode of $\lambda(x)$. We can thus write the general solution to the local conformal constraints as a wave function of $\psi[f; V, \tau]$, where V denotes the spatial volume.

We now turn to the spatial diffeomorphism constraint. Exponentiating the spatial diffeomorphism constraint to finite diffeomorphisms implies that for each small diffeomorphism f_0 there is a unitary operator acting as the pull-back under a diffeomorphism,

$$U_{f_0}\psi : [\lambda, f; \tau) \mapsto \psi[f_0^*\lambda, f_0 \circ f; \tau), \tag{7.50}$$

where we assumed above that U_{f_0} is unitary. The pull-back action $f_0^*\lambda$ on the conformal factor is the source of the nonlocal terms that we encountered in the action of the diffeomorphisms in the previous subsection. However, this action is trivial on the space of solutions to the local conformal constraint, since $f_0^*V = V$. We can thus easily impose the diffeomorphism constraint

$$U_{f_0}\psi[f; V, \tau) = \psi[f_0 \circ f; V, \tau) \equiv \psi[f, V, \tau) \tag{7.51}$$

for all diffeomorphisms f_0, which implies for solutions to the local conformal constraint that $\psi[f; V, \tau)$ is independent of f. We thus find that the solution space to the local constraints of shape dynamics consists of Schrödinger wave functions $\psi(V, \tau)$. We would have ended up with an induced measure $d\mu(V, \tau)$ for these functions had we specified an explicit measure at the beginning, but due to the formal nature of our discussion, we do not have such a result.

To proceed, we assume from now on that the wave functions $\psi(V, \tau)$ are elements of the Hilbert space $\mathcal{H}_0$ used in reduced phase space quantization [83]. We now consider the shape dynamics Hamiltonian $H_{\mathrm{SD}} = \tau_2^2 \left(p_1^2 + p_2^2\right) - V \left(\langle\pi\rangle^2 - 4\Lambda\right)$, which can be quantized on the factor $\mathcal{H}_0$ that remains after solving the linear constraints by replacing $p_i \to -i\frac{\partial}{\partial\tau^i}$ and $\langle\pi\rangle \to -i\frac{\partial}{\partial V}$. This leads to the quantum shape dynamics Hamiltonian

$$H = -\tau_2^2 \left(\partial_{\tau_1}^2 + \partial_{\tau_2}^2\right) + V^2 \left(\partial_V^2 + 4\Lambda\right). \tag{7.52}$$

This is the covariant reduced phase space Hamiltonian [83]. We thus confirmed the expectation of the last subsection that Dirac quantization of shape dynamics should be equivalent to reduced phase space quantization.

7.4 Conclusions

The true value of pure gravity on a torus in 2+1 dimensions is that it is a non-trivial yet completely solvable model that exhibits many of the features of more complicated gravitational systems. It has thus established itself as a valuable testing ground for new gravitational theories such as shape dynamics that one can use to learn about the new theory. The main difficulty in constructing shape dynamics is to obtain explicit expressions for the shape dynamics Hamiltonian, which is generically nonlocal, on the full

ADM phase space, so we are mainly interested in obtaining an explicit shape dynamics Hamiltonian.

The explicit (rather than formal) solvability of the initial value problem on the torus (and 2-sphere) in CMC gauge is the technical reason for the explicit constructability of the shape dynamics Hamiltonian on these topologies. We find that the shape dynamics Hamiltonian formally coincides with the reduced phase space Hamiltonian and that this Hamiltonian is invariant under diffeomorphisms and conformal transformations that preserve the total volume. The difference between the two is that the shape dynamics Hamiltonian is a function of the full ADM phase space, which happens to functionally depend only on the image of reduced phase space under the canonical embedding, while the reduced phase space Hamiltonian is a phase space function on reduced phase space itself.

Although we cannot construct the shape dynamics Hamiltonian on higher-genus Riemann surfaces explicitly, we can construct it perturbatively, using an expansion that is suitable in a large-volume regime. The leading orders of this expansion turn out to coincide with the temporal gauge Hamiltonian.

The Hamiltonian is in general a nonlocal phase space function, but it becomes local in the large-volume limit. One finds that the leading order in a large-volume expansion turns the Hamiltonian into the conformal constraint that changes the total volume, so full conformal invariance is attained in this limit.

Since all local constraints are linear in momenta, one can formally quantize them as vector fields on configuration space assuming that there are measures which render them divergence-free. Then gauge invariance implies that the wave function is invariant under the flow generated by these vector fields, which in turn implies that the wave function depends only on reduced configuration space, which is finite-dimensional. The Hamiltonian depends only on operators that preserve the reduced phase space, and thus Dirac quantization of the field theory is effectively reduced to reduced phase space quantization.

CHAPTER 8

Conclusions and outlook

In this thesis, we have investigated the effective dynamics of 2d and 3d lattice gravity using a combination of analytical and numerical methods. Measurements of various gauge-invariant observables in chapters 2 to 6 have led both to non-trivial confirmations of anticipated results and to new insights into the large-scale properties of the models.

The first observable we encountered was the shortest loop length in chapter 2. Its distribution showed a very accurate scaling with the two-volume in accordance with the predicted Hausdorff dimensions $d_h = 4$ for pure gravity and $d_h = (3 + \sqrt{17})/2$ for gravity coupled to matter with central charge $c = -2$. Also, the measured distribution of the moduli, which we introduced as observables in chapter 3, were matched accurately to continuum results. In this sense, two-dimensional dynamical triangulations as an ideal testing ground for geometric observables has lived up to its expectations. Some interesting questions remain unanswered at present and might lead to further investigations. Can we quantitatively explain the effect of matter fields on the distribution of shortest loop lengths? What is the continuum distribution of moduli in Liouville theory on higher-genus surfaces? How does the observable $A[\mathbf{T}]$, which we introduced in section 5.3, scale with two-volume in dynamical triangulations? More generally, can we understand better the fractal nature of the two-dimensional triangulations in the harmonic embedding (see figure 3.3)?

In chapters 4, 5 and 6 we studied a number of observables in 2+1 dimensions, with the main goal of understanding the semi-classical effective dynamics of CDT. Contrary to the two-dimensional models, we do not know what to expect of a potential continuum limit. An obvious starting point is to take other approaches to quantum gravity in 2+1 dimensions as reference. The classical theory of general relativity in 2+1 dimensions is much simpler than its higher-dimensional counterpart due to the absence of local degrees of freedom. As a consequence of the topological nature, several attempts

to quantize gravity in 2+1 dimensions have turned out, at least partially, successful (see [35] for an overview and section 7.3 for an example of such an attempt in the context of shape dynamics). These successes, and the fact that CDT was introduced as a path integral quantization of the Einstein–Hilbert action, led us to initially consider the Einstein–Hilbert action as an ansatz for the effective description of CDT. However, we soon encountered difficulties in comparing the measurements of observables to this ansatz. In order to make progress we had to be more open-minded concerning the effective action and take seriously the preferred time foliation in CDT. The measurements of the spatial volumes and the moduli in chapters 4 and 5 allowed us to narrow down the form of the effective action. We established the effective kinetic term for the spatial volumes and the moduli, which turned out to be in agreement with a kinetic term in the full effective action given by the generalized Wheeler–DeWitt metric $\mathcal{G}_\lambda$ in (5.15). In chapter 6 we demonstrated that such a kinetic term also describes well the correlations of the extrinsic curvature at a fixed boundary.

These results seem to strengthen the connection between CDT and Hořava–Lifshitz gravity already mentioned in the introduction. However, a direct comparison is nontrivial since we are still in the Euclidean setting and our range of couplings $\lambda < 1/2$ is unusual from the point of view of Hořava–Lifshitz gravity.

In chapter 1 we partly motivated the construction of large-scale observables by emphasizing that they can help in the search for a continuum limit. Throughout this thesis we have identified several such observables, but we have not yet seen a concrete realization of this idea. Instead, we have mainly focussed on establishing effective descriptions of CDT models with fixed system sizes. To obtain a continuum limit we should in some way decrease the physical lattice spacing, both in the timelike and spacelike direction. In the computer simulations this can be done in principle by increasing the number N_3 of tetrahedra (and the time extent T) and adjusting the CDT couplings such that the dimensionless large-scale observables remain invariant. It is unlikely that this will be possible in general with the small number of couplings that are currently available in the CDT action in 2+1 dimensions. Nonetheless, by way of an outlook, let us see whether we can use the measurements we performed in chapter 5 to understand how the coupling k_0 should be adjusted with increasing N_3.

A dimensionless quantity that can be directly extracted from the correlation functions of the spatial volume $V(t)$ and the moduli $\tau_i(t)$ is[38]

$$f_{ij}(t) = \lim_{t' \to t} \frac{\langle (\tau_i(t) - \tau_i(t'))(\tau_j(t) - \tau_j(t')) \rangle}{\langle (V(t) - V(t'))^2 \rangle} \frac{\langle V(t) \rangle \langle V(t') \rangle}{\langle \tau_2(t) \rangle \langle \tau_2(t') \rangle}. \qquad (8.1)$$

---

[38]We write $f_{ij}(t)$ in this form to emphasize the direct relation to the correlation functions. In line with the analysis in section 5.3 we could also have written $f_{ij}(t)$ in terms of the inverse correlators, which is more convenient from a numerical point of view.

In section 5.3 we gathered evidence that this quantity in CDT is well described by

$$f_{ij}(t) = 2(\tfrac{1}{2} - \lambda) \langle V(t)A(t) \rangle \delta_{ij},$$ (8.2)

for some value of λ, and $A(t)$ is the curvature functional (5.31) evaluated on the spatial metric. Keeping $f_{ij}(t)$ fixed, perhaps up to rescaling of the time variable t, is equivalent to keeping the product $(\tfrac{1}{2} - \lambda) \langle V(t)A(t) \rangle$ fixed. Recall that $V(t)A(t) \geq 1$ is a measure of the deviation from flatness of the spatial geometry at time t. A preliminary investigation has shown that, for fixed k_0, $\langle V(t)A(t) \rangle$ seems to grow with the spatial volume and therefore with the system size N_3. To keep $f_{ij}(t)$ fixed, $\tfrac{1}{2} - \lambda$ should decrease and we know that this can be achieved by increasing k_0. This leads to the preliminary conclusion that, in order to preserve the minisuperspace dynamics with increasing spatial lattice size, the coupling k_0 should be increased towards the phase transition. Notice that this is a necessary requirement; we have by no means shown that it is sufficient.

It would be interesting to understand whether this observation can be related to the conjectured scaling of λ in Hořava–Lifshitz gravity [67] (see [99, 102] for status reports). Also, the analysis above can in principle be extended to CDT actions with additional terms, like the Hořava–Lifshitz-like CDT action introduced in [20].

APPENDIX A

Volume contained in baby universes for $c = -2$

In this appendix we will show that the model of dynamical triangulations coupled to conformal charge $c = -2$ is not only numerically convenient, but also allows some properties to be investigated analytically. Here we will discuss baby universes with neck size one and two, which were introduced in chapter 2. These baby universes are relevant in this chapter because they contain precisely the triangles with zero area in the conformal embedding in the Euclidean plane (see section 3.2). We will compute the expected fractions $\langle N_{b,1} \rangle / N$ and $\langle N_{b,2} \rangle / N$ of triangles contained in baby universes of neck size $L = 1$ and $L = 2$ respectively, as $N \to \infty$. In terms of the dual 3-valent graphs we will count the number of vertices contained in tadpole and self-energy diagrams following the methods in [29, 41, 77].

The idea behind this computation is that for large N we can treat subsystems in DT, like baby universes, in a grand canonical way, in the sense that these subsystems will feel a constant cosmological constant μ. The value of this constant is given by the critical cosmological constant, i.e. the smallest value μ for which the grand canonical partition function $Z(\mu)$ yields a finite expected volume. In the case of $c = -2$ it is given by $\mu = \log(8)$, which follows from the asymptotics of the explicit expression for the fixed-volume partition function (2.19),

$$Z(N) = \frac{1}{N+2} C(N) C \left(\frac{N}{2} + 1 \right),$$ (A.1)

where $C(n)$ represent the Catalan numbers

$$C(n) = \frac{1}{n+1} \binom{2n}{n} = \frac{(2n)!}{(n+1)!n!}.$$ (A.2)

The number $Z_1(N)$ of decorated triangulations with N triangles and a boundary consisting of one edge is given by

$$Z_1(N) = C(N)C\left(\frac{N+1}{2}\right) \tag{A.3}$$

for N odd, and $Z_1(N) = 0$ for N even. Its generating function $Z_1(\mu)$ is given by

$$Z_1(\mu) = \sum_{k=0}^{\infty} C(2k+1)C(k+1)e^{-\mu(2k+1)} = \frac{1}{2}e^{\mu}\left(1 - {}_2F_1\left(-\frac{1}{4}, \frac{1}{4}; 2; 64e^{-2\mu}\right)\right) \tag{A.4}$$

in terms of the ordinary hypergeometric function ${}_2F_1$.

In $c = -2$ triangulations we have two types of dual edges, those that are part of the spanning tree, which we will call decorated edges and represent by fat lines, and those that are not, which we will call undecorated edges and represent by thin lines. If we denote the renormalized edges by an arrow, we can write down a Dyson-like equation in which the blob represents $Z_1(\mu)$ (see also [41]), namely,
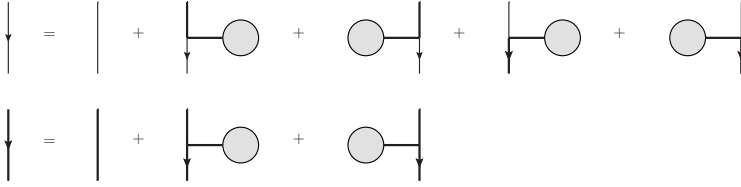
Hence we have for the decorated propagator $Z_e^*(\mu)$ and the undecorated propagator $Z_e(\mu)$

$$Z_e^*(\mu) = 1 + 2e^{-\mu}Z_1(\mu)Z_e^*(\mu) \tag{A.5}$$
$$Z_e(\mu) = 1 + 2e^{-\mu}Z_1(\mu)(Z_e^*(\mu) + Z_e(\mu)). \tag{A.6}$$

The solution is found to be

$$Z_e^*(\mu) = \frac{1}{1 - 2e^{-\mu}Z_1(\mu)} \quad \text{and} \quad Z_e(\mu) = Z_e^*(\mu)^2 = \frac{1}{(1 - 2e^{-\mu}Z_1(\mu))^2}. \tag{A.7}$$

The expectation values $\langle n_e^* \rangle$ and $\langle n_e \rangle$ for the number of triangles per renormalized decorated and undecorated edge are

$$\langle n_e^* \rangle = \frac{1}{2}\langle n_e \rangle = -\frac{d}{d\mu}\log Z_e^*(\mu) = \frac{d}{d\mu}\log(1 - 2e^{-\mu}Z_1(\mu)). \tag{A.8}$$

Evaluating (A.8) at $\mu = \log(8)$ using Mathematica we find $\langle n_e^* \rangle = 1/8$ and $\langle n_e^* \rangle = 1/4$. In a renormalized triangulation with N_0 triangles we have exactly $N_0 - 1$ decorated dual

edges and $N_0/2 + 1$ undecorated edges. If we denote by $\tilde{N}_{b,1}$ the number of triangles contained in baby universes, including the triangle attaching it to the dual edge, we have for large N_0

$$\frac{\langle \tilde{N}_{b,1} \rangle}{N_0} = \langle n_e^* \rangle + \frac{1}{2} \langle n_e \rangle = \frac{1}{4}, \tag{A.9}$$

and hence

$$\frac{\langle \tilde{N}_{b,1} \rangle}{N} = \frac{\langle \tilde{N}_{b,1} \rangle}{N_0 + \langle \tilde{N}_{b,1} \rangle} = \frac{1}{5}. \tag{A.10}$$

This is not exactly the number that we were looking for because the triangle attaching the baby universe to the dual edge is technically not inside the baby universe. Hence, to obtain the expected volume $\langle N_{b,1} \rangle$ contained in all baby universes we have to subtract from $\langle \tilde{N}_{b,1} \rangle$ the expected number σN_0 of baby universes. The expected number of baby universes per decorated dual edge is

$$-\frac{d}{d\lambda}\bigg|_{\lambda=0} \log(1 - 2e^{-\mu}e^{\lambda} Z_1(\mu)) = \left(\Gamma\left(\frac{7}{4}\right) \Gamma\left(\frac{9}{4}\right) - 1 \right)/2 = \left(\frac{15\pi}{32\sqrt{2}} - 1 \right)/2, \tag{A.11}$$

and for an undecorated dual edge it is exactly twice this number. Therefore we have

$$\sigma = \frac{15\pi}{32\sqrt{2}} - 1. \tag{A.12}$$

We conclude that

$$\frac{\langle N_{b,1} \rangle}{N} = \frac{\langle \tilde{N}_{b,1} \rangle/N_0 - \sigma}{1 + \langle \tilde{N}_{b,1} \rangle/N_0} = \frac{1}{5}(1 - 4\sigma) = \frac{9}{5} - \frac{3\pi}{4\sqrt{2}} \approx 0.133919. \tag{A.13}$$

From a Monte Carlo simulation of torus triangulations with $N = 25\,000$ triangles we have established numerically $\langle N_{b,1} \rangle/N = 0.13395 \pm 0.00002$.

Let us now turn to the case of baby universes with neck size two. Above we normalized away self-energy diagrams that consist of multiple tadpoles. Now we want to get rid of all self-energy diagrams, which is actually slightly easier. We have to consider two types of self-energies, $Z_2^*(\mu)$ for which the renormalized dual edge is decorated, and $Z_2(\mu)$ for an undecorated renormalized dual edge.

Let $Z_2^*(N)$ be the number of decorated triangulations with N triangles of a disk with boundary of two edges (of which we have marked one edge). For N even we have

$$Z_2^*(N) = C(N) \sum_{k=0}^{N/2} C(k) C\left(\frac{N}{2} - k\right) = C(N) C\left(\frac{N}{2} + 1\right) \tag{A.14}$$

and $Z_2^*(N) = 0$ for N odd. Therefore its generating function is

$$Z_2^*(\mu) = \sum_{k=0}^{\infty} C(2k)C(k+1)e^{-2\mu k} = {}_2F_1\left(\frac{1}{4}; \frac{3}{4}; 3; 64e^{-2\mu}\right). \tag{A.15}$$

The undecorated renormalized dual edges also originate from triangulations of a disk with a boundary of two edges. However, now the triangulation should be decorated with two disjoint trees which together span the dual graph and which are rooted at the two boundary edges. Let $Z_2(N)$ be the number of such triangulations with N triangles. We can find this number by noticing that such a triangulation can be constructed from two arbitrary trees and a pairwise gluing of the external lines of both trees combined. However, we have to disregard the pairwise gluings that do not result in a connected triangulation. Hence we obtain

$$Z_2(N) = \sum_{k=0}^{N} C(k)C(N-k)C\left(\frac{N}{2} + 1\right)$$

$$- \sum_{l=0}^{N/2-1} C(2l+1)C(N-2l-1)C(l+1)C\left(\frac{N}{2} - l\right) \tag{A.16}$$

$$= Z_1(N+1) - \sum_{l=0}^{N} Z_1(l)Z_1(N-l).$$

Its generating function becomes

$$Z_2(\mu) = e^{\mu}Z_1(\mu) - Z_1(\mu)^2 = \frac{1}{4}e^{2\mu}\left(1 - {}_2F_1\left(-\frac{1}{4}, \frac{1}{4}; 2; 64e^{-2\mu}\right)^2\right). \tag{A.17}$$

Again we can calculate the expected numbers $\langle n_e^* \rangle$ and $\langle n_e \rangle$ of triangles per renormalized edge at $\mu = \log(8)$, resulting in

$$\langle n_e^* \rangle = -\frac{d}{d\mu} \log Z_2^*(\mu) = \frac{3}{8}, \tag{A.18}$$

$$\langle n_e \rangle = -\frac{d}{d\mu} \log Z_2(\mu) = \frac{512}{225\pi^2 - 2048} - 2 \quad (\approx 0.965). \tag{A.19}$$

As a consequence the expected number $\langle N_{b,2} \rangle$ of triangles contained in baby universes with neck size two for large N is given by

$$\frac{\langle N_{b,2} \rangle}{N} = \frac{\langle n_e^* \rangle + \frac{1}{2}\langle n_e \rangle}{1 + \langle n_e^* \rangle + \frac{1}{2}\langle n_e \rangle} = 3\frac{2^{12} - 375\pi^2}{675\pi^2 - 2^{12}} \approx 0.46169248. \tag{A.20}$$

This fraction is exactly the fraction of triangles that have zero volume in a harmonic embedding of the torus in the Euclidean plane. Again this value agrees with a Monte Carlo simulation of torus triangulations with $N = 25\,000$ triangles which gave

$$\langle N_{b,2} \rangle / N = 0.46167 \pm 0.00002\,. \tag{A.21}$$

Higher-genus moduli measurements

The way we have set up the moduli measurements in section 3.2 allows for a rather straightforward generalization to surfaces of genus h larger than 1.[39] For such surfaces the complex structure is characterized by the Teichmüller space of complex dimension $3h-3$. Identifying explicitly $3h-3$ complex moduli parameters is a difficult task and one which we will not pursue for general genus. Instead, we will use a direct generalization of the genus-1 moduli parameter τ in the complex upper half-plane $\mathbb{H}$ to matrices Ω in the h-dimensional Siegel upper half-plane $\mathbb{H}_h$, known as period matrices [49]. The Siegel complex upper half-plane $\mathbb{H}_h$ consists of all symmetric complex $h \times h$ matrices Ω with a positive-definite imaginary part. A period matrix corresponding to a surface is known to determine its complex structure completely. For genus $h \leq 2$ we can identify $\mathbb{H}_h$ with Teichmüller space, but for $h \geq 3$ Teichmüller space appears as a non-trivial submanifold in $\mathbb{H}_h$ (as is apparent from comparing their dimensions).

In order to define the period matrix for a Riemannian manifold we first have to choose a set of $2h$ closed curves $a_1, \ldots, a_h, b_1, \ldots, b_h$ that generate the fundamental group and satisfy

$$i(a_i, a_j) = i(b_i, b_j) = 0 \quad \text{and} \quad i(a_i, b_j) = \delta_{ij}, \tag{B.1}$$

where $i(\cdot, \cdot)$ denotes the oriented intersection number. The space of harmonic 1-forms is $2h$-dimensional and it is possible to choose a basis $\{\alpha_i, \beta_i\}$ dual to the curves a_i and b_i in the sense that

$$\int_{a_i} \beta_j = \int_{b_i} \alpha_j = 0 \quad \text{and} \quad \int_{a_i} \alpha_j = \int_{b_i} \beta_j = \delta_{ij}. \tag{B.2}$$

---

[39]A method similar to the one described here has been previously employed in a completely different context in [61].

A complex basis of holomorphic 1-forms is given by

$$\omega_i = \alpha_i + i * \alpha_i, \tag{B.3}$$

where $*$ is the Hodge dual. The period matrix Ω is then given by $\Omega = A^{-1}B$ in terms of the matrices

$$A_{ij} = \int_{a_j} \omega_i \quad \text{and} \quad B_{ij} = \int_{b_j} \omega_i. \tag{B.4}$$

We can express these integrals in terms of the inner products $\langle \alpha_i | \alpha_j \rangle$, $\langle \alpha_i | \beta_j \rangle$ and $\langle \beta_i | \beta_j \rangle$ by using the Riemann bilinear relations [49], which state that any two closed 1-forms ρ and σ satisfy

$$\int \rho \wedge \sigma = \sum_{i=1}^{h} \int_{a_i} \rho \int_{b_i} \sigma - \int_{a_i} \sigma \int_{b_i} \rho. \tag{B.5}$$

Therefore

$$A_{ij} = \delta_{ij} + i \int_{a_j} *\alpha_i = \delta_{ij} + i \int *\alpha_i \wedge \beta_j = \delta_{ij} - i\langle \alpha_i | \beta_j \rangle \tag{B.6}$$

and

$$B_{ij} = i \int_{b_j} *\alpha_i = i \int \alpha_j \wedge *\alpha_i = i\langle \alpha_i | \alpha_j \rangle. \tag{B.7}$$

Another consequence of (B.5) is that

$$
\begin{aligned}
\delta_{ij} &= \int \alpha_i \wedge \beta_j = \int *\alpha_i \wedge *\beta_j = \sum_{k=1}^{h} \int_{a_k} *\alpha_i \int_{b_k} *\beta_j - \int_{a_k} *\beta_j \int_{b_k} *\alpha_i \\
&= \sum_{k=1}^{h} \int \beta_k \wedge *\alpha_i \int \alpha_k \wedge *\beta_j - \int \beta_k \wedge *\beta_j \int \alpha_k \wedge *\alpha_i \\
&= \sum_{k=1}^{h} \langle \alpha_i | \alpha_k \rangle \langle \beta_k | \beta_j \rangle - \langle \alpha_i | \beta_k \rangle \langle \alpha_k | \beta_j \rangle.
\end{aligned} \tag{B.8}
$$

We can directly apply these formulae to DT piecewise linear geometries by replacing α_i and β_i by their discrete counterparts and the inner product by the discrete one from (3.26). For genus $h = 1$ we used (B.8) to establish the normalization of the discrete inner product leading to the expression for $\Omega = [\tau]$ in (3.24). For genus $h \geq 2$ there is an overall ambiguity in the definition of Ω because (B.8) is not exactly satisfied (up to an overall factor) due to discretization artefacts. However, we expect (and have confirmed numerically for genus 2) that for large random surfaces (B.8) is close to a multiple of the identity matrix with high probability. In that case we can unambiguously normalize the inner product and determine Ω.

The modular group $SL(2, \mathbb{Z})/\mathbb{Z}_2$, which acts on the upper half-plane as in (3.9) generalizes to the action of the symplectic group $Sp(2h, \mathbb{Z})/\mathbb{Z}_2$ on the Siegel upper half-plane $\mathbb{H}_h$. Fundamental domains can again be worked out but become increasingly cumbersome for larger genus (see e.g. [54]).

Finally, let us mention that our algorithm for generating random DT surfaces coupled to $c = -2$ conformal matter can be extended straightforwardly to genus $h \geq 2$. The only missing ingredient is a construction of a random unicellular map of genus h. Here again we can use results from [38] where for any genus h an explicit bijection is found between the set of unicellular maps of genus h and a union of sets of unicellular maps of lower genus with a particular number of distinguished vertices.

APPENDIX C

A bounded minisuperspace action

We have seen in section 4.4 that, at least in the presence of time reversal symmetry, the measured volume profiles agree qualitatively with classical solutions of the minisuperspace action

$$S[V, \tau_i] = \kappa \int dt \left(-\frac{1}{2} \frac{\dot{V}^2}{V} + \frac{V}{2} \frac{\dot{\tau}_1^2 + \dot{\tau}_2^2}{\tau_2^2} + 2\Lambda V \right). \tag{C.1}$$

By contrast, we observed in chapter 5 that the correlations in the quantum fluctuations of the spatial volume and the moduli point towards a minisuperspace action of the form[40]

$$S[V, \tau_i] = \kappa \int dt \left(\rho \frac{\dot{V}^2}{V} + \frac{V}{2} \frac{\dot{\tau}_1^2 + \dot{\tau}_2^2}{\tau_2^2} + U(V) \right), \tag{C.2}$$

with an unknown potential function $U(V)$ and $\rho > 0$. Obviously, changing ρ from $-1/2$ in (C.1) to $\rho > 0$ will have a large effect on the classical solutions. However, in this appendix we will show that any solution to (C.1) can be obtained from (C.2) with $\rho > 0$ provided that we choose an appropriate potential $U(V)$. This shows that an effective action of the form (C.2) is not necessarily incompatible with our considerations concerning the volume profiles in sections 4.3 and 4.4. Moreover, it leads to a natural potential term that we may consider later in a more thorough investigation of the effective action.

Let us for the moment assume that we have chosen boundary conditions at $t = 0$ and $t = T$ with non-zero spatial volume and finite moduli.[41] To find the classical solutions of (C.2) we first solve the equations of motion for the moduli. Recall from section 4.3 that

---

[40]We assume here that the prefactor $A[g]$ appearing in (5.35) scales canonically with volume and is independent of the moduli, i.e. $A[g] \propto V^{-1}$.

[41]A more careful treatment is needed for degenerate boundary conditions, but the results remain essentially the same.

the momentum $p = V\sqrt{\dot{\tau}_1^2 + \dot{\tau}_2^2}/\tau_2$ defines a conserved quantity and that the moduli evolution takes place on a geodesic in the upper half-plane. Since p is proportional to the speed along the geodesic, we have

$$d(\tau(0), \tau(T)) = \int_0^T dt \frac{\sqrt{\dot{\tau}_1{}^2 + \dot{\tau}_2{}^2}}{\tau_2} = p \int_0^T dt \frac{1}{V(t)}, \tag{C.3}$$

where $d(\cdot, \cdot)$ is the hyperbolic distance in the upper half-plane defined by the Poincaré metric. Using this relation, we can eliminate the moduli from the action (C.2), giving

$$S[V] = \kappa \int dt \left(\rho \frac{\dot{V}^2}{V} + U(V) \right) + \kappa \frac{d(\tau(0), \tau(T))^2}{\int_0^T dt \frac{1}{V(t)}}. \tag{C.4}$$

Now suppose $V_0(t)$ is the solution to (C.1). Using this expression one can show that $V_0(t)$ is also a solution to (C.2) if we choose

$$U(V) = -4\rho\Lambda V + \frac{\alpha}{V} \tag{C.5}$$

with the coupling α given by

$$\alpha = (1 + 2\rho) \frac{d(\tau(0), \tau(T))^2}{\left(\int_0^T dt \frac{1}{V_0(t)} \right)^2}. \tag{C.6}$$

We conclude that, as far as the classical solutions are concerned, a change in ρ can be compensated by changing the strength of a inverse-volume potential. However, this only holds at the level of individual classical solutions. Given a set of solutions to (C.2) as function of the boundary conditions, we can deduce the value of ρ without knowledge of the potential $U(V)$. The simplest way to do this is by considering the limit $T \to 0$, because then the potential $U(V)$ drops out of the equations of motion (see also our discussion in section 6.1).

Moduli change under an edge flip

In this appendix we will have a closer look at the discretization of the functional $A[g]$, introduced in section 5.3. In the continuum it describes the expected change (squared) of the moduli τ_i, as measured by the Poincaré metric, under a random metric deformation that is normalized with respect to the Wheeler–DeWitt metric. A natural discretization is to define $A'[\mathbf{T}_0]$ to be proportional to the expected change in the discrete moduli under a random local update of the triangulation. To fix the proportionality constant we demand that $A'[\mathbf{T}_0]$ evaluated on a regular triangulation $\mathbf{T}_0$ with N triangles gives precisely $A'[\mathbf{T}_0] = 1/N$. A convenient random update move is the random *edge flip*, which we used in our Monte Carlo simulations of 2d dynamical triangulations in section 2.2. Let us see whether we can work out explicitly the definition of $A'[\mathbf{T}_0]$ in terms of harmonic forms.

Suppose we are given a triangulation $\mathbf{T}_0$ of the torus with N triangles and harmonic 1-forms α^i dual to a pair of generators of the fundamental group. Let e be an edge of the triangulation and denote by $\bar{e}$ the edge that appears after flipping e as in figure D.1. The harmonic 1-forms after flipping are denoted by $\bar{\alpha}^i$. With a slight abuse of notation, let us denote by $\alpha^i(\bar{e})$ the vector connecting the initial and final vertex of $\bar{e}$ in the old embedding and likewise by $\bar{\alpha}^i(e)$ the vector connecting the initial and final vertex of e in the new embedding. Then it can be shown that the new inner product $\langle \bar{\alpha}^i, \bar{\alpha}^j \rangle$ can be expressed in terms of the old one as

$$\langle \bar{\alpha}^i, \bar{\alpha}^j \rangle = \langle \alpha^i, \alpha^j \rangle + \alpha^i(\bar{e})\bar{\alpha}^j(\bar{e}) - \alpha^i(e)\bar{\alpha}^j(e). \tag{D.1}$$

Hence, the change in the inner product can be deduced from the geometries before and after the flip of the quadrilateral of which e and e' are the diagonals.

It follows from the derivation in section 3.2 that the flat metric of the embedding space, which is characterized by the discrete modular parameter τ, is determined by
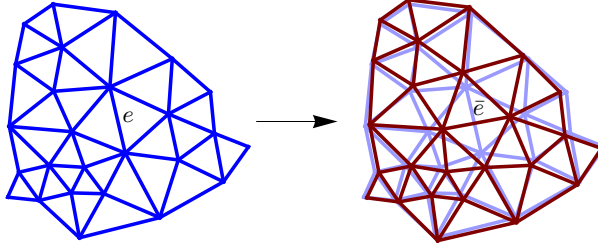
Figure D.1: *Harmonic embedding before and after an edge flip.*

the inverse g_{ij} of $g^{ij} = \langle \alpha^i, \alpha^j \rangle$. Let us assume that the change $\delta_e g^{ij} = \langle \bar{\alpha}^i, \bar{\alpha}^j \rangle - \langle \alpha^i, \alpha^j \rangle$ in the inverse metric under the edge flip is small compared to g^{ij}, which will definitely be the case for $N \to \infty$. Then we can write the quadratic displacement in moduli space using the inverse Wheeler–DeWitt metric projected onto the traceless modes

$$\frac{|\delta_e \tau|^2}{\tau_2^2} = \frac{1}{2} \delta_e g^{ij} \left(\frac{1}{2} (g_{ik} g_{jl} + g_{il} g_{jk}) - \frac{1}{2} g_{ij} g_{ik} \right) \delta_e g^{kl}. \tag{D.2}$$

Using expression (D.1) we obtain

$$\frac{|\delta_e \tau|^2}{\tau_2^2} = \frac{1}{4} (\alpha(e) \cdot \bar{\alpha}(e) + \alpha(\bar{e}) \cdot \bar{\alpha}(\bar{e}))^2 - (\alpha(e) \cdot \bar{\alpha}(\bar{e}))(\alpha(\bar{e}) \cdot \bar{\alpha}(e)), \tag{D.3}$$

where the dot product refers to the metric g_{ij}. This expression is exact in the large-N limit, but not manageable in practice since we need to know the geometry of the quadrilateral after the edge flip. Therefore we apply an approximation: we replace $\bar{\alpha}$ in (D.3) by α. Roughly speaking, this corresponds to neglecting the change in position of the vertices in the embedding and only taking into account the fact that the sum in the inner product is over a different set of edges. To show that this is a reasonable approximation we took a random triangulation with $N = 800$ triangles and computed for all possible edge flips the exact distance $d(\tau, \tau')$ between the moduli τ and τ' before and after the flip. In figure D.2a we have plotted these values together with the predictions from (D.3) with and without the approximation $\bar{\alpha}^i = \alpha^i$. We observe that the approximation introduces a systematic but small over-estimation.

The combined area a_e of the two triangles sharing the edge e is given by

$$a_e = \frac{1}{2} \sqrt{(\alpha(e) \cdot \alpha(e))(\alpha(\bar{e}) \cdot \alpha(\bar{e})) - (\alpha(\bar{e}) \cdot \alpha(\bar{e}))^2}. \tag{D.4}$$
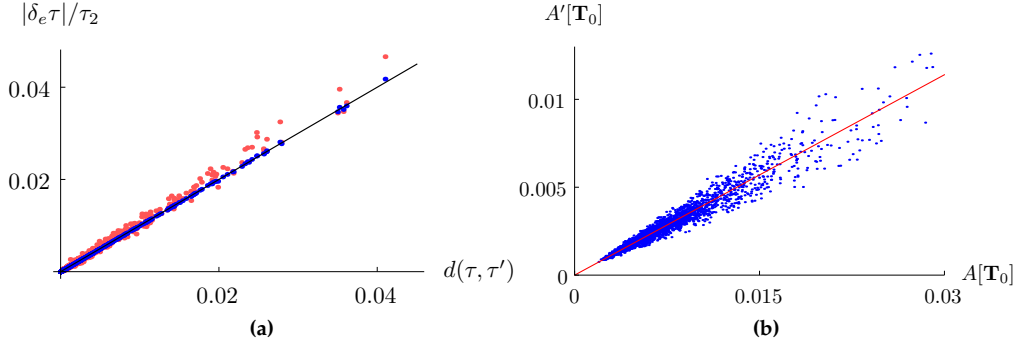
Figure D.2: *(a) For each edge e the predicted change $|\delta_e \tau|/\tau_2$ of the moduli is plotted according to (D.3) with (red) and without (blue) the approximation $\bar{\alpha}^i = \alpha^i$. On the horizontal axis is the exact distance $d(\tau, \tau')$ between the moduli τ and τ' before and after the edge flip. (b) Measurements of the new $A'[\mathbf{T}_0]$ compared to the original $A[\mathbf{T}_0]$ in an ensemble of dynamical triangulations with $N = 5\,000$ triangles. The fit corresponds to $A'[\mathbf{T}_0] = 0.38 A[\mathbf{T}_0]$.*

Therefore in the approximation $\alpha^i = \bar{\alpha}^i$ we can write

$$\frac{|\delta_e \tau|^2}{\tau_2^2} \approx 4a_e^2 + \frac{1}{4}(\alpha(e) \cdot \alpha(e) - \alpha(\bar{e}) \cdot \alpha(\bar{e}))^2. \tag{D.5}$$

The expected change of the moduli under a random edge flip is obtained simply by taking the average of (D.3) over all $3N/2$ edges e,[42]

$$\frac{|\delta \tau|^2}{\tau_2^2} = \frac{2}{3N} \sum_e \left[4a_e^2 + \frac{1}{4}(\alpha(e) \cdot \alpha(e) - \alpha(\bar{e}) \cdot \alpha(\bar{e}))^2 \right]. \tag{D.6}$$

To complete our definition for $A'[\mathbf{T}_0]$ we have to find the correct normalization of (D.6) by evaluating it on a regular triangulation with N triangles. A straightforward calculation gives $|\delta \tau|^2/\tau_2^2 = 64/(9N^2)$ and therefore we define $A'[\mathbf{T}_0]$ by

$$A'[\mathbf{T}_0] = \frac{9}{64} N \frac{|\delta \tau|^2}{\tau_2^2} = \frac{3}{16} \sum_e \left[a_e^2 + \frac{1}{16}(\alpha(e) \cdot \alpha(e) - \alpha(\bar{e}) \cdot \alpha(\bar{e}))^2 \right]. \tag{D.7}$$

This definition is a bit more complicated than the original $A[\mathbf{T}_0]$ we used in section 5.3, due to the presence of the second term and the sum being over the edges instead of the

---

[42]We disregard the fact that some edges are not allowed to be flipped depending on the chosen ensemble of triangulations.

triangles. The second term tells us that among the triangles with a particular area the ones that are far from equilateral have the most influence on the moduli.

We have tested the relation between $A'[\mathbf{T}_0]$ and $A[\mathbf{T}_0]$ for an ensemble of dynamical triangulations with $N = 5\,000$ triangles, whose results are shown in figure D.2b. Up to statistical fluctuations we find a relation $A'[\mathbf{T}_0] \approx 0.38A[\mathbf{T}_0]$. We conclude from this analysis that the discretization of A in terms of a sum over squares of areas is quite robust up to overall normalization. Luckily the normalization does not affect any results from section 5.3 other than a possible rescaling of $1/2 - \lambda$.

Poisson Delaunay triangulations

Our treatment of CDT with fixed boundaries requires a method of producing two-dimensional triangulations approximating a Riemannian manifold. To approximate a flat torus we can simply start with a regular triangular lattice which we periodically identify to obtain a triangulated torus. However, constructing by hand triangulations approximating a *curved* Riemannian manifold is non-trivial. To accomplish this we use a random lattice technique known as Poisson Delaunay triangulation [28, 48, 69, 89].

Let us describe first the algorithm applied to a domain in the Euclidean plane. By a Poisson process, we sprinkle the preferred number of points into the domain with a probability density ρ. Then we construct the corresponding so-called Delaunay triangulation having these points as vertices. A Delaunay triangulation is a triangulation that satisfies for each triangle the condition that its circumscribed circle encircles no vertices other than its own. Such a triangulation always exists and for vertices in generic positions is unique [89]. In order to get a purely combinatorial manifold as required in CDT we simply throw away the information about the edge lengths and regard every triangle as being equilateral.

The procedure can in principle be generalized directly to two-dimensional Riemannian manifolds. The sprinkling process is now performed with respect to a probability density proportional to the volume form. This density and therefore the number of vertices must be large enough to ensure existence [81]. Moreover, in order to obtain a good approximation we have to make sure the average distance between nearby vertices is much smaller than the curvature scale of the manifold.

Figure E.1 illustrates the Poisson Delaunay triangulation of a constant-curvature two-sphere. Constructing the Delaunay triangulation is particularly simple in this case because it is equivalent to finding the convex hull of the vertices in $\mathbb{R}^3$ (i.e. the shape we would get by wrapping the vertices in plastic wrap, say).
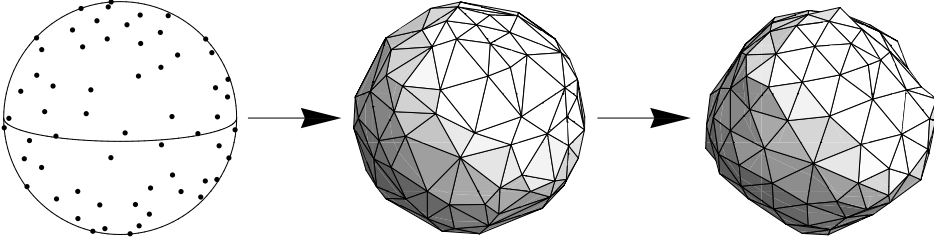
Figure E.1: *How to construct a Poisson Delaunay triangulation of the sphere: 1. sprinkle vertices into the sphere, 2. construct the convex hull of the vertices in $\mathbb{R}^3$, 3. replace the triangles by equilateral ones.*

We can use this Delaunay triangulation procedure also to produce triangulations of surfaces which are conformally related to the sphere (and by the uniformization theorem any metric on the sphere is). To see this, notice that the Delaunay conditions on the triangulation only depend on ratios of distances between nearby points. This means that the Delaunay triangulation is insensitive to conformal transformations that vary little at the discretization scale. The information about the volume form (or the conformal factor) only appears in the sprinkling density ρ. In particular, to construct a Poisson Delaunay triangulation of an ellipsoid we only need to determine a function $\rho : S^2 \to \mathbb{R}$ such that $ds^2 = \rho^2 d\Omega^2$ is isometric to that ellipsoid.[43] Then we can use this density to sprinkle points into S^2.

In practice, to increase the quality of the triangulations, we impose a requirement on the minimal distance between vertices during the sprinkling process. Of course, in case of a non-constant density ρ we should take this minimal distance to be proportional to $\rho^{-1/2}$ to maintain the conformal properties.

---

[43]Using the relation between the conformal latitude and the latitude θ of the sphere, which is well-known by cartographers, we can find ρ. No expression for ρ in closed form is known to us, but expanded in the eccentricity ϵ we have $\rho(\theta) = 1 - 2\sin^2\theta\,\epsilon^2 - \frac{1}{12}(9 + 23\cos(2\theta))\sin^2\theta\,\epsilon^4 + \mathcal{O}(\epsilon^6)$.

Bibliography

[1]   M. E. Agishtein and A. A. Migdal, 'Simulations of four-dimensional simplicial quantum gravity as dynamical triangulation', *Modern Physics Letters A* 7 (1992) 1039–1061.

[2]   J. Ambjørn, J. Barkley, T. Budd, and R. Loll, 'Baby universes revisited', *Physics Letters B* 706 (2011) 86–89, arXiv:1110.3998.

[3]   J. Ambjørn, J. Barkley, and T. Budd, 'Roaming moduli space using dynamical triangulations', *Nuclear Physics B* (2011), arXiv:1110.4649.

[4]   J. Ambjørn, L. Chekhov, C. Kristjansen, and Y. Makeenko, 'Matrix model calculations beyond the spherical limit', *Nuclear Physics B* 404 (1993) 127–172, arXiv:hep-th/9302014.

[5]   J. Ambjørn, J. Correia, C. Kristjansen, and R. Loll, 'The relation between Euclidean and Lorentzian 2D quantum gravity', *Physics Letters B* 475 (2000) 24–32, arXiv:hep-th/9912267.

[6]   J. Ambjørn, B. Durhuus, and J. Fröhlich, 'Diseases of triangulated random surface models, and possible cures', *Nuclear Physics B* 257 (1985) 433–449.

[7]   J. Ambjørn, B. Durhuus, and T. Jonsson, 'Three-dimensional simplicial quantum gravity and generalized matrix models', *Modern Physics Letters A* 6 (1991) 1133–1146.

[8]   J. Ambjørn, B. Durhuus, and T. Jonsson, *Quantum geometry : A statistical field theory approach*, Cambridge Monographs on Mathematical Physics, Cambridge University Press, 1997.

[9]   J. Ambjørn, A. Görlich, S. Jordan, J. Jurkiewicz, and R. Loll, 'CDT meets Hořava–Lifshitz gravity', *Physics Letters B* 690 (2010) 413–419, arXiv:1002.3298.

[10] J. Ambjørn, A. Görlich, J. Jurkiewicz, and R. Loll, 'Nonperturbative quantum de Sitter universe', *Physical Review D* 78 (2008) 063544–17, arXiv:0807.4481.

[11] J. Ambjørn, A. Görlich, J. Jurkiewicz, and R. Loll, 'Geometry of the quantum universe', *Physics Letters B* 690 (2010) 420–426, arXiv:`1001.4581`.

[12] J. Ambjørn, J. Jurkiewicz, and R. Loll, 'Dynamically triangulating Lorentzian quantum gravity', *Nuclear Physics B* 610 (2001) 347–382, arXiv:`hep-th/0105267`.

[13] J. Ambjørn, J. Jurkiewicz, and R. Loll, 'Nonperturbative 3D Lorentzian quantum gravity', *Physical Review D* 64 (2001) 044011, arXiv:`hep-th/0011276`.

[14] J. Ambjørn, J. Jurkiewicz, and R. Loll, 'Emergence of a 4D world from causal quantum gravity', *Physical Review Letters* 93 (2004) 131301, arXiv:`hep-th/0404156`.

[15] J. Ambjørn, J. Jurkiewicz, and R. Loll, 'The spectral dimension of the universe is scale dependent', *Physical Review Letters* 95 (2005) 171301, arXiv:`hep-th/0505113`.

[16] J. Ambjørn and R. Loll, 'Non-perturbative Lorentzian quantum gravity, causality and topology change', *Nuclear Physics B* 536 (1998) 407–434, arXiv:`hep-th/9805108`.

[17] J. Ambjørn and Y. Watabiki, 'Scaling in quantum gravity', *Nuclear Physics B* 445 (1995) 129–142, arXiv:`hep-th/9501049`.

[18] J. Ambjørn, S. Jain, and G. Thorleifsson, 'Baby universes in 2d quantum gravity', *Physics Letters B* 307 (1993) 34–39, arXiv:`hep-th/9303149`.

[19] J. Ambjørn and S. Varsted, 'Three-dimensional simplicial quantum gravity', *Nuclear Physics B* 373 (1992) 557–577.

[20] C. Anderson, S. Carlip, J. H. Cooperman, P. Hořava, R. Kommu, and P. R. Zulkowski, 'Quantizing Hořava-Lifshitz gravity via causal dynamical triangulations' (2011), arXiv:`1111.6634`.

[21] E. Anderson, J. Barbour, B. Z. Foster, B. Kelleher, and N. Ó Murchadha, 'The physical gravitational degrees of freedom', *Classical and Quantum Gravity* 22 (2005) 1795–1802, arXiv:`gr-qc/0407104`.

[22] H. Aoki, H. Kawai, J. Nishimura, and A. Tsuchiya, 'Operator product expansion in two-dimensional quantum gravity', *Nuclear Physics B* 474 (1996) 512–528, arXiv:`hep-th/9511117`.

[23] T. Banks, W. Fischler, and L. Susskind, 'Quantum cosmology in 2+1 and 3+1 dimensions', *Nuclear Physics B* 262 (1985) 159–186.

[24] J. Barbour, 'Shape dynamics. An introduction' (2011), arXiv:`1105.0183`.

[25] J. Barbour and N. Ó Murchadha, 'Conformal superspace: the configuration space of general relativity' (2010), arXiv:`1009.3559`.

[26] D. Benedetti and J. Henson, 'Spectral geometry as a probe of quantum spacetime', *Physical Review D* 80 (2009) 124036, arXiv:0911.0401.

[27] M. Bershadsky and I. R. Klebanov, 'Genus-one path integral in two-dimensional quantum gravity', *Physical Review Letters* 65 (1990) 3088–3091.

[28] L. Bombelli, A. Corichi, and O. Winkler, 'Semiclassical quantum gravity: statistics of combinatorial Riemannian geometries', *Annalen der Physik* 14 (2005) 499–519, arXiv:gr-qc/0409006.

[29] D. V. Boulatov, V. A. Kazakov, I. K. Kostov, and A. A. Migdal, 'Analytical and numerical study of a model of dynamically triangulated random surfaces', *Nuclear Physics B* 275 (1986) 641–686.

[30] D. V. Boulatov and A. Krzywicki, 'On the phase diagram of three-dimensional simplicial quantum gravity', *Modern Physics Letters A* 6 (1991) 3005–3014.

[31] L. Brewin, 'The Riemann and extrinsic curvature tensors in the Regge calculus', *Classical and Quantum Gravity* 5 (1988) 1193.

[32] T. Budd, 'The effective kinetic term in CDT' (2011), arXiv:1110.5158.

[33] T. Budd and T. Koslowski, 'Shape dynamics in 2+1 dimensions' (2011), arXiv:1107.1287.

[34] S. Carlip, 'Notes on the (2+1)-dimensional Wheeler–DeWitt equation', *Classical and Quantum Gravity* 11 (1994) 31–39, arXiv:gr-qc/9309002.

[35] S. Carlip, *Quantum gravity in 2+1 dimensions*, Cambridge University Press, 2003.

[36] S. Carlip, 'Quantum gravity in 2+1 dimensions: the case of a closed universe', *Living Reviews in Relativity* 8 (2005), arXiv:gr-qc/0409039.

[37] S. Carlip, 'Spontaneous dimensional reduction in short-distance quantum gravity?', *AIP Conference Proceedings* 1196 (2009) 72–80, arXiv:0909.3329.

[38] G. Chapuy, 'A new combinatorial identity for unicellular maps, via a direct bijective approach', *Advances in Applied Mathematics* 47 (2011) 874–893, arXiv:1006.5053.

[39] A. Dasgupta and R. Loll, 'A proper-time cure for the conformal sickness in quantum gravity', *Nuclear Physics B* 606 (2001) 357–379, arXiv:hep-th/0103186.

[40] F. David, 'Planar diagrams, two-dimensional lattice gravity and surface models', *Nuclear Physics B* 257 (1985) 45–58.

[41] F. David, 'Randomly triangulated surfaces in - 2 dimensions', *Physics Letters B* 159 (1985) 303–306.

[42] M. Desbrun, A. Hirani, and J. Marsden, 'Discrete exterior calculus' (2005), arXiv:`math/0508341`.

[43] M. Desbrun, E. Kanso, and Y. Tong, 'Discrete differential forms for computational modeling', in: *Discrete Differential Geometry*, pp. 287–324, 2008.

[44] P. A. M. Dirac, 'Fixation of coordinates in the Hamiltonian theory of gravitation', *Physical Review* 114 (1959) 924–930.

[45] J. Distler and H. Kawai, 'Conformal field theory and 2D quantum gravity', *Nuclear Physics B* 321 (1989) 509–527.

[46] B. Dittrich, 'Partial and complete observables for canonical general relativity', *Classical and Quantum Gravity* 23 (2006) 6155–6184, arXiv:`gr-qc/0507106`.

[47] B. Dittrich and R. Loll, 'Hexagon model for 3D Lorentzian quantum cosmology', *Physical Review D* 66 (2002) 084016, arXiv:`hep-th/0204210`.

[48] R. Dyer, H. Zhang, and T. Möller, 'A survey of Delaunay structures for surface representation' (2009).

[49] H. M. Farkas and I. Kra, *Riemann surfaces*, Springer, 1992.

[50] Fermi GRB/LAT collaborations, 'A limit on the variation of the speed of light arising from quantum gravity effects', *Nature* 462 (2009) 331–334, arXiv:`0908.1832`.

[51] P. D. Francesco, P. Mathieu, and D. Sénéchal, *Conformal field theory*, Springer, 1997.

[52] L. Freidel and K. Krasnov, 'A new spin foam model for 4D gravity', *Classical and Quantum Gravity* 25 (2008) 125018, arXiv:`0708.1595`.

[53] R. Friedberg and T. Lee, 'Derivation of Regge's action from Einstein's theory of general relativity', *Nuclear Physics B* 242 (1984) 145–166.

[54] G. van der Geer, 'Siegel modular forms' (2006), arXiv:`math/0605346`.

[55] G. W. Gibbons, S. W. Hawking, and M. J. Perry, 'Path integrals and the indefiniteness of the gravitational action', *Nuclear Physics B* 138 (1978) 141–150.

[56] P. Ginsparg and G. Moore, 'Lectures on 2D gravity and 2D string theory (TASI 1992)' (1993), arXiv:`hep-th/9304011`.

[57] H. Gomes, 'The dynamics of shape', PhD thesis, University of Nottingham, 2011, arXiv:`1108.4837`.

[58] H. Gomes, S. Gryb, and T. Koslowski, 'Einstein gravity as a 3D conformally invariant theory', *Classical and Quantum Gravity* 28 (2011) 045005, arXiv:`1010.2481`.

[59] H. Gomes and T. Koslowski, 'The link between general relativity and shape dynamics' (2011), arXiv:`1101.5974`.

[60] S. Gryb, 'Shape dynamics and Mach's principles: Gravity from conformal geometrodynamics', PhD thesis, University of Waterloo, Canada, 2011.

[61] X. Gu and S. Yau, 'Computing conformal structure of surfaces' (2002), arXiv:`cs/0212043`.

[62] S. S. Gubser and I. R. Klebanov, 'Scaling functions for baby universes in two-dimensional quantum gravity', *Nuclear Physics B* 416 (1994) 827–849, arXiv:`hep-th/9310098`.

[63] A. Gupta, S. P. Trivedi, and M. B. Wise, 'Random surfaces in conformal gauge', *Nuclear Physics B* 340 (1990) 475–490.

[64] A. Hatcher, *Algebraic topology*, Cambridge University Press, 2002.

[65] S. W. Hawking, 'The path-integral approach to quantum gravity.', in: *General Relativity: An Einstein Centenary Survey*, pp. 746–789, Cambridge University Press, 1979.

[66] P. Hořava, 'Membranes at quantum criticality', *Journal of High Energy Physics* 2009 (2009) 020–020, arXiv:`0812.4287`.

[67] P. Hořava, 'Quantum gravity at a Lifshitz point', *Physical Review D* 79 (2009) 084008, arXiv:`0901.3775`.

[68] P. Hořava, 'Spectral dimension of the universe in quantum gravity at a Lifshitz point', *Physical Review Letters* 102 (2009) 161301, arXiv:`0902.3657`.

[69] C. Itzykson, J. Drouffe, and P. V, *Statistical field theory: strong coupling, Monte Carlo methods, conformal field theory*, Cambridge UniversityPress, 1991.

[70] S. Jain and S. D. Mathur, 'World-sheet geometry and baby universes in 2D quantum gravity', *Physics Letters B* 286 (1992) 239–246, arXiv:`hep-th/9204017`.

[71] T. Jonsson, 'Width of handles in two-dimensional quantum gravity', *Physics Letters B* 425 (1998) 265–268, arXiv:`hep-th/9801150`.

[72] H. Kawai, N. Kawamoto, T. Mogami, and Y. Watabiki, 'Transfer matrix formalism for two-dimensional quantum gravity and fractal structures of space-time', *Physics Letters B* 306 (1993) 19–26, arXiv:`hep-th/9302133`.

[73] H. Kawai, N. Tsuda, and T. Yukawa, 'Complex structures defined on dynamically triangulated surfaces', *Physics Letters B* 351 (1995) 162–168, arXiv:`hep-th/9503052`.

[74] H. Kawai, N. Tsuda, and T. Yukawa, 'Complex structure of a DT surface with T2 topology', *Nuclear Physics B - Proceedings Supplements* 53 (1997) 777–779, arXiv:`hep-lat/9609002`.

[75] N. Kawamoto, V. A. Kazakov, Y. Saeki, and Y. Watabiki, 'Fractal structure of two-dimensional gravity coupled to c=-2 matter', *Physical Review Letters* 68 (1992) 2113.

[76] V. A Kazakov, 'Ising model on a dynamical planar random lattice: Exact solution', *Physics Letters A* 119 (1986) 140–144.

[77] V. A. Kazakov, I. K. Kostov, and A. A. Migdal, 'Critical properties of randomly triangulated planar random surfaces', *Physics Letters B* 157 (1985) 295–300.

[78] D. Knuth, *The art of computer programming, volume 4A, combinatorial algorithms, part 1*, Addison-Wesley, 2011.

[79] J. Laiho and D. Coumbe, 'Evidence for asymptotic safety from lattice quantum gravity', *Physical Review Letters* 107 (2011) 161301, arXiv:`1104.5505`.

[80] O. Lauscher and M. Reuter, 'Ultraviolet fixed point and generalized flow equation of quantum gravity', *Physical Review D* 65 (2001) 025013, arXiv:`hep-th/0108040`.

[81] G. Leibon and D. Letscher, 'Delaunay triangulations and Voronoi diagrams for Riemannian manifolds', *Proceedings of the sixteenth annual symposium on Computational geometry* (2000) 341–349.

[82] R. Loll, 'Discrete approaches to quantum gravity in four dimensions', *Living Reviews in Relativity* 1 (1998) 13, arXiv:`gr-qc/9805049`.

[83] E. Martinec, 'Soluble systems in quantum gravity', *Physical Review D* 30 (1984) 1198–1204.

[84] P. O. Mazur and E. Mottola, 'The path integral measure, conformal factor problem and stability of the ground state of quantum gravity', *Nuclear Physics B* 341 (1990) 187–212.

[85] V. Moncrief, 'Reduction of the Einstein equations in 2+1 dimensions to a Hamiltonian system over Teichmüller space', *Journal of Mathematical Physics* 30 (1989) 2907–2914.

[86] J. R. Munkres, *Elements of algebraic topology*, Perseus Books, 1984.

[87] S. Muroya, A. Nakamura, C. Nonaka, and T. Takaishi, 'Lattice QCD at finite density', *Progress of Theoretical Physics* 110 (2003) 615–668, arXiv:`hep-lat/0306031`.

[88] R. Nakayama, '2D quantum gravity in the proper-time gauge', *Physics Letters B* 325 (1994) 347–353, arXiv:`hep-th/9312158`.

[89] A. Okabe, B. Boots, and K. Sugihara, *Spatial tessellations: concepts and applications of Voronoi diagrams*, John Wiley and Sons, 2000.

[90] N. Ó Murchadha and J. W. York, 'Existence and uniqueness of solutions of the Hamiltonian constraint of general relativity on compact manifolds', *Journal of Mathematical Physics* 14 (1973) 1551.

[91] D. Oriti, 'The group field theory approach to quantum gravity', in: *Approaches to quantum gravity - toward a new understanding of space, time, and matter*, ed. by D. Oriti, Cambridge University Press, 2009.

[92] A. Perez, 'Spin foam models for quantum gravity', *Classical and Quantum Gravity* 20 (2003) R43–R104, arXiv:`gr-qc/0301113`.

[93] T. Regge, 'General relativity without coordinates', *Il Nuovo Cimento* 19 (1961) 558–571.

[94] R. L. Renken, S. M. Catterall, and J. B. Kogut, 'Phase structure of dynamical triangulation models in three dimensions', *Nuclear Physics B* 523 (1998) 553–568, arXiv:`hep-lat/9712011`.

[95] M. Reuter, 'Nonperturbative evolution equation for quantum gravity', *Physical Review D* 57 (1998) 971–985, arXiv:`hep-th/9605030`.

[96] M. Reuter and F. Saueressig, 'Fractal space-times under the microscope: a renormalization group view on Monte Carlo data', *Journal of High Energy Physics* 12 (2011) 012, arXiv:`1110.5224`.

[97] C. Rovelli, *Quantum gravity*, Cambridge University Press, 2004.

[98] J. Smit, *Introduction to quantum fields on a lattice: "a robust mate"*, Cambridge University Press, 2002.

[99] T. P. Sotiriou, 'Hořava-Lifshitz gravity: a status report', *Journal of Physics: Conference Series* 283 (2011) 012034, arXiv:`1010.3218`.

[100] L. A. Takhtajan and L. Teo, 'Weil-Petersson metric on the universal Teichmüller space I: Curvature properties and Chern forms' (2003), arXiv:`math/0312172`.

[101] T. Thiemann, *Modern canonical quantum general relativity*, Cambridge University Press, 2007.

[102] M. Visser, 'Status of Hořava gravity: a personal perspective', *Journal of Physics: Conference Series* 314 (2011) 012002, arXiv:`1103.5587`.

[103] Y. Watabiki, 'Analytic study of fractal structure of quantized surface in two-dimensional quantum gravity', *Prog. Theor. Phys. Suppl.* 114 (1993) 1–17.

[104] S. Weinberg, 'Ultraviolet divergences in quantum theories of gravitation.', *General relativity: An Einstein centenary survey* (1979) 790–831.

[105] R. M. Williams and P. A. Tuckey, 'Regge calculus: a brief review and bibliography', *Classical and Quantum Gravity* 9 (1992) 1409–1422.

[106] R. M. Williams, 'Quantum Regge calculus', in: *Approaches to quantum gravity - toward a new understanding of space, time, and matter*, ed. by D. Oriti, Cambridge University Press, 2009.

[107] S. A. Wolpert, 'The Weil-Petersson metric geometry', in: *Handbook of Teichmüller geometry*, vol. 2, IRMA Lectures in Mathematics and Theoretical Physics 13, 2007.

[108] S. A. Wolpert, 'Geodesic-length functions and the Weil-Petersson curvature tensor' (2010), arXiv:`1008.2293`.

[109] J. W. York, 'Role of conformal three-geometry in the dynamics of gravitation', *Physical Review Letters* 28 (1972) 1082–1085.

[110] J. W. York, 'Conformally invariant orthogonal decomposition of symmetric tensors on Riemannian manifolds and the initial-value problem of general relativity', *Journal of Mathematical Physics* 14 (1973) 456.

Samenvatting

Bijna honderd jaar geleden introduceerde Einstein de *algemene relativiteitstheorie* van de zwaartekracht. Deze theorie kan gezien worden als vervanging van de gravitatiewet van Newton, die een instantane aantrekkingskracht beschrijft tussen twee puntmassa's. In de algemene relativiteitstheorie is er geen sprake meer van directe interactie tussen massa's op afstand. In plaats daarvan wordt de zwaartekracht beschreven door middel van een interactie met het zwaartekrachtsveld, op soortgelijke wijze als het elektromagnetische veld de aantrekking tussen geladen deeltjes beschrijft. Anders dan het elektromagnetische veld kan het zwaartekrachtsveld opgevat worden als een fundamentele eigenschap van de ruimtetijd; het beschrijft namelijk haar geometrie. Massa veroorzaakt kromming van de ruimtetijd en deze beïnvloedt de banen van deeltjes die zich door de ruimtetijd bewegen.

Om dit te illustreren beschouwen we een versimpeld model van de algemene relativiteitstheorie waarin we de tijd en één van de ruimtelijke dimensies buiten beschouwing laten. In figuur 1a zien we een voorbeeld van een tweedimensionale ruimte met in het midden een gebied met kromming, bijvoorbeeld veroorzaakt door een tweedimensionale massaverdeling. Merk op dat we de derde dimensie hier enkel gebruiken om de kromming te illustreren, maar dat deze verder geen fysische betekenis heeft. De zwarte lijnen tonen mogelijke banen van deeltjes die door de ruimte bewegen. De buitenste banen voeren door nagenoeg vlakke ruimte en beschrijven daarom rechte lijnen, zoals we verwachten van deeltjes waar geen krachten op werken. In gekromde ruimte beweegt een deeltje over een zogenaamde geodeet, de natuurlijke generalisatie van een rechte lijn in een gekromde ruimte. We zien in figuur 1a dat de geodeten door de kromming kunnen worden afgebogen, alsof er een aantrekkingskracht werkt op de deeltjes. Echter, er is geen sprake van een kracht in de gebruikelijke zin. De precieze banen van de deeltjes worden enkel bepaald door de geometrie van de ruimte.

Hoe de ruimtetijd wordt gekromd onder invloed van een massaverdeling wordt beschreven door de Einsteinvergelijkingen. Deze vergelijkingen leggen echter niet de precieze geometrie van de ruimtetijd vast. Net als het elektromagnetische veld interne vrijheidsgraden kent in de vorm van elektromagnetische golven, zo heeft ook het
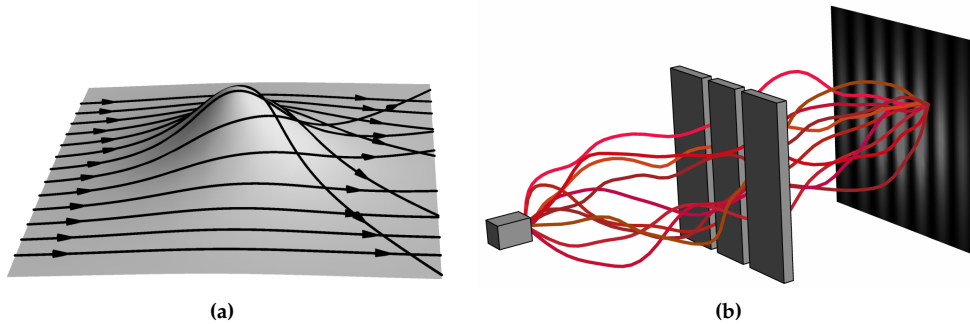
Figuur 1: *(a) De baan van een deeltje wordt beïnvloed door de kromming van de ruimte. (b) Het tweespletenexperiment met een aantal willekeurige banen van de bron naar een punt op het scherm.*

zwaartekrachtsveld interne vrijheidsgraden. Deze vrijheidsgraden zorgen ervoor dat zelfs in het vacuüm, dat wil zeggen in afwezigheid van materie en andere krachten, de zwaartekracht een niet-triviale dynamica kent. De dynamica van de zwaartekracht, oftewel van de geometrie van de ruimtetijd, vormt een belangrijk onderwerp in dit proefschrift. Dit kan zich manifesteren in zogenaamde zwaartekrachtsgolven, maar ook in een tijdsevolutie van globale vorm van de ruimte.

De algemene relativiteitstheorie is een zogenaamde klassieke theorie. Dit wil zeggen dat zij niet geformuleerd is in het raamwerk van de *kwantummechanica*. De ontwikkeling van de kwantummechanica bracht ongeveer honderd jaar geleden, misschien nog wel meer dan de relativiteitstheorie, een revolutie teweeg binnen de theoretische natuurkunde. Men ontdekte dat licht zich in bepaalde situaties beter laat beschrijven in termen van deeltjes, terwijl elektronen en protonen zich kunnen gedragen als golven. Een experiment dat duidelijk het golfkarakter van deeltjes laat zien is het tweespleten-experiment in figuur 1b (we komen straks terug op de getoonde paden). Deeltjes die door een dubbele spleet geschoten worden belanden op het achterliggende scherm met een waarschijnlijkheidsverdeling die een interferentiepatroon vertoont. De kwantummechanica levert een wiskundige beschrijving van deze *golf-deeltje-dualiteit*.

In dit proefschrift maken we gebruik van het *padintegraalformalisme*, een formulering van de kwantummechanica geïntroduceerd door Feynman. In dit formalisme draagt elke mogelijke evolutie van een systeem bij aan de waarschijnlijkheidsverdeling van de uitkomst van een meting. We kunnen dit illustreren aan de hand van het bovengenoemde tweespletenexperiment. Om de kans te bepalen dat een deeltje op een bepaalde plaats op het scherm terecht komt, beschouwen we alle mogelijke paden van de bron

naar dat punt, waarvan we er enkele hebben weergegeven in figuur 1b. Aan elke baan kunnen we een complex getal toekennen in termen van de zogenaamde klassieke actie van het deeltje. De som van al deze getallen zegt iets over de kans dat het deeltje op het betreffende punt terecht komt. Door deze berekening voor verschillende eindpunten te herhalen kan het waargenomen interferentiepatroon verklaard worden.

De kwantummechanica kan niet alleen toegepast worden op individuele deeltjes, maar ook op hele velden zoals het elektromagnetische veld. In het padintegraalformalisme sommeren we niet meer over alle mogelijke paden van een deeltje, maar over alle mogelijke configuraties van een veld in de ruimtetijd. Het resultaat is de *kwantumveldentheorie* die een groot gedeelte van de materie en krachten in ons heelal nauwkeurig beschrijft, zoals samengevat in het *standaard model* van de elementaire deeltjes. Echter, er is één grote afwezige in het standaard model en dat is de zwaartekracht.

Tot op heden is het natuurkundigen nog niet gelukt om een welgedefinieerde kwantumveldentheorie van de zwaartekracht op te stellen. Het ontbreken van een theorie van de *kwantumzwaartekracht* is geen probleem als het gaat om het verklaren van huidige experimenten. Bij experimenten in deeltjesversnellers, zoals de LHC bij CERN, kan de zwaartekracht compleet verwaarloosd worden, omdat de andere fundamentele krachten vele malen sterker zijn. In systemen waar de zwaartekracht wel een belangrijke rol speelt, zoals in het geval van planeetbanen, zijn doorgaans kwantumeffecten verwaarloosbaar en volstaat de (klassieke) algemene relativiteitstheorie. Daarentegen is het niet uitgesloten dat in de toekomst experimenten zullen worden ontwikkeld die vatbaar zijn voor kwantumeffecten van de zwaartekracht. Bovendien hebben we een kwantumtheorie van de zwaartekracht nodig om de natuurkunde in de buurt van singulariteiten in de ruimtetijd beter te begrijpen, zoals in het vroege heelal en in het binnenste van zwarte gaten.

De standaard methode om uitkomsten van observaties te berekenen in de kwantumveldentheorie is door middel van storingsrekening of *perturbatietheorie*. Hierbij worden alleen veldconfiguraties meegenomen in de padintegraal die in een kleine omgeving liggen van een klassieke configuratie (meestal het vacuüm). Ondanks de inperking van het aantal configuraties levert de padintegraal doorgaans oneindigheden op. Dit is gedeeltelijk te wijten aan de *onzekerheidsrelatie* van de kwantummechanica: hoe kleiner de lengteschaal waarop we een configuratie bestuderen, des te wilder worden de waargenomen kwantumfluctuaties. Om de kwantumfluctuaties in te perken, en daarmee tot eindige antwoorden te komen, kunnen we een regularisatie in de vorm van een minimale lengteschaal introduceren in de padintegraal. Vervolgens kan men proberen de regularisatie te verwijderen en de oneindigheden die weer tevoorschijn komen op te vangen door middel van *renormalisatie* van koppelingsconstanten. Dergelijke renormalisatie blijkt mogelijk te zijn voor alle velden in het standaard model, maar niet zonder

meer voor het zwaartekrachtsveld.

In dit proefschrift benaderen we de kwantumzwaartekracht zonder gebruik te maken van de perturbatietheorie, oftewel we bestuderen *niet-perturbatieve* kwantumzwaartekracht. Dit betekent dat we in principe alle configuraties van het zwaartekrachtsveld in de ruimtetijd moeten meenemen in de padintegraal. Aangezien het zwaartekrachtsveld de geometrie beschrijft van de ruimtetijd, komt dit neer op een sommatie over alle mogelijke geometrieën. Net als in de perturbatieve kwantumveldentheorie is een regularisatie noodzakelijk om zinnige antwoorden uit berekeningen te krijgen. Een manier om kwantumfluctuaties in de geometrie op kleine lengteschalen te beperken is door de ruimtetijd op te bouwen uit elementaire bouwstenen. Het model dat we in dit proefschrift beschouwen, genaamd *dynamische triangulatie*, heeft als bouwstenen gelijkzijdige simplices. Dit zijn gelijkzijdige driehoeken, tetraëders of 4-simplices, afhankelijk van het aantal dimensies waarin we werken (zie figuur 1.1 in de introductie). In twee dimensies betekent dit dat we de gladde ruimte, zoals afgebeeld in figuur 1a, vervangen door een triangulatie opgebouwd uit gelijkzijdige driehoeken met een vaste afmeting. Met een vaste hoeveelheid driehoeken kan slechts een eindig aantal geometrieën gebouwd worden en daarmee zijn we in principe verlost van de oneindigheden in de bijbehorende padintegraal. Vervolgens kunnen we onderzoeken wat er gebeurt als we een steeds groter aantal driehoeken nemen met een steeds kleinere afmeting.

In twee dimensies hebben we de beschikking over een aantal analytische methoden om de padintegraal over geometrieën te lijf te gaan. Deze kunnen echter niet in elke situatie toegepast worden en in meer dan twee dimensies zijn er nauwelijks analytische methoden beschikbaar. Gelukkig leent dynamische triangulatie zich bij uitstek voor numerieke simulaties. Na een zogenaamde *Wick-rotatie*, die de tijd transformeert in een extra ruimtelijke dimensie, kunnen we het kwantummechanische systeem opvatten als een thermisch systeem. Dit geeft ons de mogelijkheid om methoden uit de statistische thermodynamica toe te passen op de padintegraal over geometrieën. Met behulp van *Monte-Carlo-simulaties* kunnen we bijvoorbeeld willekeurige triangulaties genereren die representatief zijn voor de complete verzameling van geometrieën in de padintegraal. Door herhaaldelijk een meting van een zekere observabele te verrichten op een willekeurige triangulatie en vervolgens deze metingen te middelen, krijgen we een goede benadering van de exacte waarde zoals gedefinieerd door de padintegraal.

De voornaamste uitdaging bij deze methode is het identificeren van goede *observabelen*. In dit geval komt een observabele overeen met een algoritme dat op consistente wijze aan een triangulatie een waarde toekent. Een eenvoudig voorbeeld van een observabele is het totale volume van de ruimte, dat proportioneel is aan het totaal aantal simplices in de triangulatie. Een belangrijk doel van ons onderzoek was het identificeren van nieuwe observabelen waarmee we de globale dynamica van het model kunnen
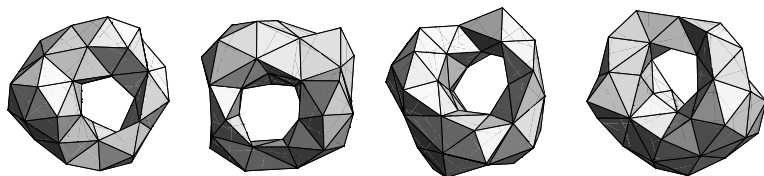
Figuur 2: *Enkele triangulaties die voorkomen in de padintegraal over tweedimensionale geometrieën op de torus.*

onderzoeken. Deze dynamica kunnen we vergelijken met de klassieke algemene relativiteitstheorie om vast te stellen of ons model daadwerkelijk de zwaartekracht beschrijft.

In hoofdstukken 2 en 3 hebben we dynamische triangulaties in twee dimensies bestudeerd. Hierbij hebben we ons beperkt tot triangulaties met de topologie van de torus, oftewel triangulaties zonder rand en precies één gat, zoals in figuur 2. Een interessante observabele voor dergelijke triangulaties wordt gegeven door de lengte van het kortste gesloten pad dat het gat van de torus omcirkelt (zie de rechterzijde van figuur 2.5). In hoofdstuk 2 hebben we met behulp van Monte-Carlo-simulaties de verwachtingswaarde en kansverdeling van deze padlengtes bepaald. Daarmee hebben we een vermoeden getest omtrent de verdeling van *babyuniversa*, oftewel van lokale uitstulpingen in de geometrie.

Een andere observabele, die een belangrijke rol speelt in het gepresenteerde onderzoek, hebben we geleend uit de theorie van Riemann-oppervlakken. Een bijzondere eigenschap van geometrie in twee dimensies is dat zij zich expliciet laat decomponeren in een *hoekgetrouwe* geometrie en een lokale schaalfactor. Een hoekgetrouwe (of conforme) geometrie op een ruimte bevat informatie over de hoeken waarmee lijnstukken elkaar snijden maar niet over de lengtes. De ruimte van geometrieën op de torus is oneindigdimensionaal, terwijl de ruimte van hoekgetrouwe geometrieën slechts tweedimensionaal is en geparametriseerd wordt door een complexe parameter, die de *modulus* wordt genoemd. In hoofdstuk 3 hebben we een algoritme beschreven om een modulus toe te kennen aan een willekeurige triangulatie van de torus. In simulaties hebben wij de kansverdeling van de modulus in de padintegraal bepaald en overeenstemming gevonden met analytische resultaten.

In hoofdstukken 4, 5 en 6 hebben we een model bestudeerd in drie dimensies, waarbij de bouwstenen bestaan uit gelijkzijdige tetraëders. Dit model, genaamd *causale dynamische triangulatie* (CDT), is een aanpassing van de dynamische triangulatie waarbij één van de dimensies aangemerkt is als de tijd. Op deze manier kunnen we de geometrie van de driedimensionale ruimtetijd beschouwen als een tijdsevolutie van een tweedi-

mensionale ruimtelijke geometrie. In hoofdstukken 4 en 5 hebben we met behulp van simulaties de tijdsevolutie van het volume van de ruimte en de hierboven beschreven modulus bestudeerd. Hierbij zijn we tot de conclusie gekomen dat een directe vergelijking met de algemene relativiteitstheorie niet zonder meer mogelijk is. In plaats daarvan hebben we aan de hand van de simulatiedata een effectief model opgesteld. Dit model toont overeenkomsten met een alternatieve beschrijving van de zwaartekracht, genaamd *Hořava–Lifshitzgravitatie*. In hoofdstuk 6 hebben we een zeker aspect van het effectieve model nader onderzocht door middel van metingen van kwantumfluctuaties in de geometrie van de ruimtetijd dichtbij haar rand.

Tenslotte hebben we in hoofdstuk 7 de algemene relativiteitstheorie in drie dimensies aan een nadere inspectie onderworpen. De *canonieke formulering* van de relativiteitstheorie beschrijft de ruimtetijd in termen van een tijdsevolutie van de tweedimensionale geometrie. Het blijkt dat met een zorgvuldig gekozen tijdvariabele deze tijdsevolutie hergeformuleerd kan worden puur in termen van hoekgetrouwe geometrie. Dit heeft als voordeel dat het oneindigdimensionale systeem in drie dimensies gereduceerd wordt tot een eindigdimensionaal systeem. Bovendien lijkt de algemene relativiteitstheorie in deze vorm beter aan te sluiten bij het hierboven beschreven model van causale dynamische triangulatie.

Acknowledgements

First of all I would like to thank my supervisor, Renate Loll, for giving me the opportunity to explore, without restrictions, the interesting world of quantum gravity, for sharing her physical intuition, for having unlimited confidence in my pursuit of crazy ideas, and for giving up sleep altogether in order to have this thesis finished in time.

I would like to express my gratitude to my collaborators for widening my view and bringing excitement to the life of a theoretical physicist. Thanks to Tim Koslowski and Sean Gryb for recognizing an "expert" of $(2+1)$-dimensional gravity in me and for two weeks of lively discussions and frantic scribblings on the blackboard. Thanks to Jan Ambjørn for introducing me to the rich physics of 2d gravity and to Jerome Barkley (whom I have only met through email) for gathering vital simulation data. I have also benefited from numerous discussion with Samo Jordan about various aspects of Monte Carlo simulations. Thanks to the Perimeter Institute for Theoretical Physics for facilitating collaboration on several occasions.

During the last four years the quantum gravity group at the Institute for Theoretical Physics has provided a continuous source of inspiration. Thanks to all postdocs and fellow PhD's and good luck to you all: Andreas, Bianca, Brendan, David, Daniele, Hanno, Igor, Irina, Juliane, Michele, Paul, Pedro, Philipp, Rachel, Samo, Sean, and Tomasz. Special thanks to Philipp for sharing an office with me for four long years, for the crazy adventures in Sicily (together with Gerben), and for the encouragements during my final weeks of struggle.

Thanks to all my colleagues and former colleagues at the Institute for Theoretical Physics for providing a pleasant atmosphere and conversations during the numerous coffee breaks (with or without "koekjes"). Special thanks to my colleague and friend Niels with whom I have shared my physics (and ice skating) "career" since the very first steps nearly ten years ago.

Thanks to all my friends, especially my friends from the QSSP, former house mates and fellow skaters for the great time we have spent together in Utrecht. I thank my parents for encouragements, advice and the occasional poetic touch. Last but not least, thanks to Toke for all her love and support.

Curriculum vitae

The author was born on July 8, 1984 in Watford, United Kingdom. At the age of six he moved to the Netherlands, where during the years 1996 to 2002 he attended the secondary school Christelijk Gymnasium Beyers Naudé in Leeuwarden. He studied physics and mathematics at Utrecht University and obtained bachelor degrees in both programmes in 2005 (with distinction). Subsequently, he followed the master's programme in theoretical physics at the same university. He wrote his graduate thesis under supervision of Renate Loll, and obtained his master's degree in 2007 (with distinction). In 2008 he started his PhD research at the Institute for Theoretical Physics in Utrecht, again under supervision of Renate Loll. The results of this research can be found in this thesis.